

# Control of flexible motion systems using frequency response data

***Citation for published version (APA):***

Hoogendijk, R. (2014). *Control of flexible motion systems using frequency response data*. [Phd Thesis 1 (Research TU/e / Graduation TU/e), Mechanical Engineering]. Technische Universiteit Eindhoven.  
<https://doi.org/10.6100/IR774666>

***DOI:***

[10.6100/IR774666](https://doi.org/10.6100/IR774666)

***Document status and date:***

Published: 01/01/2014

***Document Version:***

Publisher's PDF, also known as Version of Record (includes final page, issue and volume numbers)

***Please check the document version of this publication:***

- A submitted manuscript is the version of the article upon submission and before peer-review. There can be important differences between the submitted version and the official published version of record. People interested in the research are advised to contact the author for the final version of the publication, or visit the DOI to the publisher's website.
- The final author version and the galley proof are versions of the publication after peer review.
- The final published version features the final layout of the paper including the volume, issue and page numbers.

[Link to publication](#)

***General rights***

Copyright and moral rights for the publications made accessible in the public portal are retained by the authors and/or other copyright owners and it is a condition of accessing publications that users recognise and abide by the legal requirements associated with these rights.

- Users may download and print one copy of any publication from the public portal for the purpose of private study or research.
- You may not further distribute the material or use it for any profit-making activity or commercial gain
- You may freely distribute the URL identifying the publication in the public portal.

If the publication is distributed under the terms of Article 25fa of the Dutch Copyright Act, indicated by the "Taverne" license above, please follow below link for the End User Agreement:

[www.tue.nl/taverne](http://www.tue.nl/taverne)

***Take down policy***

If you believe that this document breaches copyright please contact us at:

[openaccess@tue.nl](mailto:openaccess@tue.nl)

providing details and we will investigate your claim.

# Control of flexible motion systems using frequency response data



This research is part of the 'Pieken in de Delta 2007' program funded by SenterNovem, an agency of the Dutch ministry of Economic Affairs.



The research reported in this thesis is part of the research program of the Dutch Institute of Systems and Control (DISC). The author has successfully completed the educational program of the Graduate School DISC.

A catalogue record is available from the Eindhoven University of Technology Library. ISBN: 978-90-386-3648-1

Typeset by the author with the pdfL<sup>A</sup>T<sub>E</sub>X documentation system.

Cover design: Marenne Fotografie, Oss, the Netherlands

Reproduction: Ipskamp Drukkers, Enschede, the Netherlands.

Copyright 2014 by R. Hoogendijk. All rights reserved.

# Control of flexible motion systems using frequency response data

PROEFSCHRIFT

ter verkrijging van de graad van doctor aan de  
Technische Universiteit Eindhoven, op gezag van de  
rector magnificus, prof.dr.ir. C.J. van Duijn, voor een  
commissie aangewezen door het College voor  
Promoties in het openbaar te verdedigen  
op dinsdag 1 juli 2014 om 16.00 uur

door

Rob Hoogendijk

geboren te Hooge en Lage Zwaluwe



Dit proefschrift is goedgekeurd door de promotoren en de samenstelling van de promotiecommissie is als volgt:

voorzitter:	prof.dr. L. P. H. de Goey
promotor:	prof.dr.ir. M. Steinbuch
copromotoren:	dr.ir. M. J. G. van de Molengraft
	dr.ir. M. F. Heertjes
leden:	prof.dr.ir S. Weiland
	prof.dr.ir. H. Butler
	dr.ir. G. Z. Angelis (SKF)
	prof.dr.ir. J. Swevers (Katholieke Universiteit Leuven)

## Societal perspective

This thesis is about *motion systems*; systems that perform controlled movements. For example, a robot arm that assembles a car, or a 3D-printer that prints a part of a machine. It is important that these motion systems are accurate and fast to enable the production of high quality products at a low cost.

The conventional techniques that are used to control these devices assume that the mechanical structure of these machines is rigid. However, for increasing requirements on speed and accuracy this assumption is no longer valid. This thesis provides important contributions to take the *flexibility* of these systems into account in the control design. To avoid the need for a mathematical model of these complex machines, the controllers are designed on the basis of accurate (*frequency response*) measurements.

The research conducted in this thesis contributes to the realization of very precise manufacturing machines that have a large throughput. In the future, this will enable the production of products with incredible functionality, e.g., the smartphones of the future, at a price that everybody can afford.



# Summary

## **Control of flexible motion systems using frequency response data**

The ever increasing technological demands from society call for inexpensive manufacturing of very complex products. This requires the motion systems that are used in the manufacturing processes to be fast and precise. Fast systems will increase the throughput which lowers the cost of the products, while high precision is required to achieve high-quality products. In order to satisfy these requirements, internal deformations of the mechanical structure that occur during the motion tasks should be considered in the control design.

One possible way to do so is to make an accurate parametric model of the system to be controlled. This would enable the use of advanced model-based control techniques. However, high-precision motion systems typically have multiple inputs and outputs and a large number of internal modes. This makes the derivation of an accurate, low-order parametric model for control purposes a complex and time-consuming task.

A different approach is to perform measurements on the system and design a controller using the obtained data. Such a data-based approach is pursued in this thesis, for the following reasons. Firstly, for motion systems, accurate frequency response data can be obtained at low cost, as these systems are typically equipped with high-precision actuators and sensors. The dynamics of these systems are relatively fast, such that the data can be obtained within a limited amount of time, i.e., typically in the order of minutes. Secondly, many of the control designs that are currently used in industry, are based on loop-shaping using frequency response data. This renders a data-based approach a natural extension of the methods that are already used.

This thesis has two main contributions that extend frequency response data-based methods to better cope with the internal dynamics of motion systems. The first contribution is a method to predict closed-loop pole locations for a given controller using only frequency response data of the system to be controlled. Insight in the closed-loop pole locations is important, since the poles of these systems tend to be lightly damped. Without appropriate control, the time-domain response

of the system thus will be oscillatory and potentially performance limiting. The currently used loop-shaping techniques provide only limited insight in the closed-loop pole locations. In this thesis, a method is developed to compute so-called transfer function data from frequency response data using Cauchy integrals. For lightly damped mechanical systems, transfer function data can be used to estimate closed-loop pole locations. Error bounds on the computed pole locations are derived by investigating the numerical aspects of the computation of transfer function data. This technique has been validated successfully by means of experiments on a benchmark single-input single-output system consisting of two masses connected via a flexible shaft. Moreover, experiments on a prototype lightweight wafer stage demonstrate that this approach is also feasible on an industrial setup. For this multi-input multi-output system, it was demonstrated that the damping of the internal dynamics could be predicted accurately by means of the proposed method. This aids the control engineer in the design and tuning of controllers that have satisfactory responses in time-domain.

The second contribution of this thesis is a design method for notch filters for multi-input multi-output systems with internal deformations. Conventional notch filter design is done for each performance degree-of-freedom separately. However, this does not take the directionality of the targeted modes into account. Moreover, multiple notch filters will be necessary to target a single mode. The novel approach in this thesis takes the directionality of the targeted modes into account by using transformation matrices in combination with conventional single-input single-output notch filters. In this way a multi-input multi-output controller is computed which reduces the controller order and facilitates the tuning process. The method was successfully applied to a flexible beam setup. Especially the off-diagonal terms of the closed-loop system show improved performance, since the directions of the modes are taken into account in the design of the notch filters.

# Contents

<b>Societal perspective</b>	<b>iii</b>
<b>Summary</b>	<b>v</b>
<b>Nomenclature</b>	<b>1</b>
<b>1 Introduction</b>	<b>7</b>
1.1 Advances in high-precision motion systems . . . . .	7
1.1.1 Accurate and fast positioning . . . . .	7
1.1.2 Integrated circuits . . . . .	8
1.1.3 Control of high-precision motion systems . . . . .	9
1.1.4 Challenges for high-precision motion systems . . . . .	10
1.2 Research objectives . . . . .	11
1.2.1 The Xtreme Motion project . . . . .	11
1.2.2 Scope and problem formulation . . . . .	12
1.3 Feedback control of flexible motion systems . . . . .	14
1.3.1 Frequency-domain data-based approaches . . . . .	14
1.3.2 Time-domain data-based approaches . . . . .	18
1.4 Research approach and contributions . . . . .	19
1.4.1 Towards data-based analysis and damping of flexible modes . . . . .	19
1.4.2 Towards incorporating directionality in the control design . . . . .	20
1.5 Outline of the thesis . . . . .	21
<b>2 Computation of closed-loop poles for SISO systems</b>	<b>23</b>
2.1 Introduction . . . . .	23
2.2 Computing TFD from FRD . . . . .	26
2.2.1 Definition of TFD . . . . .	26
2.2.2 Use of TFD . . . . .	26
2.2.3 Computation of TFD . . . . .	27
2.3 Accuracy of TFD . . . . .	30
2.3.1 Finite integral . . . . .	31

2.3.2	Integration method and resolution . . . . .	32
2.3.3	Influence of measurement noise . . . . .	35
2.3.4	LHP TFD from RHP TFD . . . . .	37
2.3.5	Error bounds on TFD . . . . .	38
2.4	Computational aspects . . . . .	40
2.4.1	Coping with undamped poles . . . . .	40
2.4.2	Computation time . . . . .	41
2.4.3	Amount of human interaction . . . . .	42
2.5	Use-case: Data-based Root-locus . . . . .	43
2.6	Results on a benchmark motion system . . . . .	44
2.7	Conclusions . . . . .	55
<b>3</b>	<b>Computation of closed-loop poles for MIMO systems</b>	<b>57</b>
3.1	Introduction . . . . .	57
3.2	Computation of TFD . . . . .	61
3.2.1	Definition of TFD . . . . .	61
3.2.2	Computation of TFD in the RHP . . . . .	62
3.2.3	TFD for systems with integrators . . . . .	65
3.2.4	Computation of TFD in the LHP . . . . .	66
3.3	Uncertainty estimation . . . . .	68
3.3.1	Error bounds due to a finite integral . . . . .	69
3.3.2	Error bounds on the integration method . . . . .	69
3.3.3	Error bounds due to noise . . . . .	71
3.3.4	Error bounds in the LHP due to asymmetry . . . . .	72
3.3.5	Total error bound . . . . .	72
3.4	Computation of closed-loop poles using TFD . . . . .	73
3.4.1	Theory . . . . .	73
3.4.2	Computational aspects . . . . .	78
3.4.3	Uncertainty in pole locations . . . . .	80
3.4.4	Grid selection . . . . .	81
3.5	Experiments and design . . . . .	82
3.5.1	The setup: a prototype wafer stage . . . . .	83
3.5.2	Identification . . . . .	84
3.5.3	Control Design . . . . .	84
3.5.4	TFD of the setup . . . . .	86
3.5.5	Example 1: Root-locus torsion mode . . . . .	87
3.5.6	Example 2: Damping 500 Hz modes . . . . .	90
3.6	Conclusions . . . . .	95

---

<b>4</b>	<b>Directionality of flexible modes</b>	<b>97</b>
4.1	Introduction . . . . .	97
4.2	Modal description . . . . .	100
4.3	Conventional notch filters . . . . .	102
4.4	Directional notch filters . . . . .	103
4.4.1	Directional notch filtering concept . . . . .	104
4.4.2	Design of the directional notch filter . . . . .	106
4.4.3	Obtaining the mode shapes . . . . .	107
4.5	Results . . . . .	109
4.5.1	Flexible beam setup . . . . .	109
4.5.2	Decentralized Control . . . . .	110
4.5.3	Directional Notch filtering . . . . .	113
4.5.4	Time-domain results . . . . .	117
4.6	Conclusions . . . . .	117
<b>5</b>	<b>Conclusions and recommendations</b>	<b>119</b>
5.1	Conclusions . . . . .	119
5.1.1	Damping of flexible modes . . . . .	119
5.1.2	Directionality of flexible modes . . . . .	120
5.2	Recommendations . . . . .	121
5.2.1	Damping of flexible modes . . . . .	122
5.2.2	Directionality of flexible modes . . . . .	123
5.2.3	General recommendations . . . . .	123
	<b>References</b>	<b>125</b>
<b>A</b>	<b>Symmetry condition using a LFT</b>	<b>135</b>
	<b>Acknowledgements</b>	<b>139</b>
	<b>Curriculum Vitae</b>	<b>141</b>





# Nomenclature

## Acronyms

DOF	Degree-of-freedom
FRD	Frequency Response Data
LFT	Linear Fractional Transformation
LHP	Left Half-Plane
MIMO	Multi-Input Multi-Output
RGA	Relative Gain Array
RHP	Right Half-Plane
SISO	Single-Input Single-Output
TFD	Transfer Function Data

## Scalar variables and SISO systems

*(Printed in normal font, lower- and uppercase)*

*roman symbols*

$a$	a constant
$A$	actuator
$b$	a constant
$c$	a constant
$C(s)$	controller
$\mathcal{C}$	contour in the s-plane
$\mathcal{C}_{\mathcal{D}}$	Nyquist contour in the s-plane
$d$	distance to the imaginary axis
$\mathcal{D}(s)$	determinant of $(\mathbf{I} + \mathbf{H}\mathbf{C})$
$\mathcal{D}(s_i)$	value of $\mathcal{D}$ at $s_i$
$\hat{\mathcal{D}}(s_i)$	estimated value of $\mathcal{D}(s_i)$

---

$E_f$	error due to finite integral
$E_i$	error due to integration method
$E_n$	error due to noise
$E_s$	error due to asymmetry
$f$	frequency in Hz
$g()$	a (complex) function
$H(j\omega)$	frequency response of the plant
$H(j\omega_k)$	frequency response of the plant at $\omega_k$
$\hat{H}(j\omega_k)$	measured frequency response of the plant at $\omega_k$
$H(s)$	transfer function of the plant
$H(s_i)$	transfer function data at $s_i$
$\hat{H}(s_i)$	estimated transfer function data at $s_i$
$H_{yu}$	$(y, u)$ entry of MIMO system $\mathbf{H}$
$I(\omega)$	integrand of Cauchy integral
$j$	$\sqrt{-1}$
$J$	cost function
$k$	gain
$K$	maximum value of the second derivative of the integrand
$L(s)$	open-loop
$L_\sigma$	line in the s-plane parallel to imaginary axis
$L_\omega$	line in the s-plane parallel to real axis
$M_{yu}$	$(y, u)$ entry of mean value second derivative of the integrand
$m_{kl}$	entries of $\mathbf{M}$
$n$	integer nonnegative number
$N$	integer nonnegative number
$N_i(s)$	notch filter
$p_{cl}$	closed-loop pole
$p_{ol}$	open-pole
$P$	probability
$r$	radius in the s-plane
$R_x$	DOF: rotation about x-axis
$R_y$	DOF: rotation about y-axis
$R_{yu}$	set of radii for entry $(y, u)$
$R_z$	DOF: rotation about z-axis
$s$	complex frequency (Laplace variable)
$s_i$	$i^{th}$ complex frequency point
$s_{\mathcal{C}}$	a point in the s-plane on the contour $\mathcal{C}$
$S(s)$	sensitivity transfer function
$t$	time
$S$	sensor
$T(s)$	closed-loop transfer function
$T$	DOF: torsion mode
$u$	input
$u(s)$	$\text{Re}(\mathcal{D}(s))$
$v(s)$	$\text{Im}(\mathcal{D}(s))$

---

$W(s)$	weighting filter
$W(j\omega)$	frequency response of weighting filter
$x$	DOF: translation along x-axis
$y$	output
$y$	DOF: translation along y-axis
$z$	DOF: translation along z-axis

*greek symbols*

$\alpha$	a point in the s-plane
$\beta$	damping ratio of filters
$\Delta\omega$	frequency resolution of FRD
$\zeta$	damping ratio plant
$\theta$	angle
$\nu(j\omega)$	circular complex noise
$\sigma$	$\text{Re}(s)$ absolute damping
$\sigma_H$	square root of variance of $\hat{H}(s_i)$
$\tau$	time constant
$\Phi_{yu}$	set of angles of entry $(y, u)$
$\phi_{cl}$	closed-loop characteristic polynomial
$\phi_{ol}$	open-loop characteristic polynomial
$\phi$	angle
$\Psi$	modal participation factor
$\omega$	$\text{Im}(s)$ frequency in rad/s
$\omega_k$	$k^{th}$ frequency point
$\omega_{max}$	maximum frequency

## Vectors

*(Printed in bold font, lowercase)*

<b><math>b_{mi}</math></b>	$i^{th}$ input mode shape
<b><math>c_{mi}</math></b>	$i^{th}$ output mode shape
<b><math>k_i</math></b>	$i^{th}$ vector of the kernel
<b><math>q_m</math></b>	modal displacements vector
<b><math>u</math></b>	input vector
<b><math>x</math></b>	state vector
<b><math>y</math></b>	output vector

## Matrices and MIMO systems

*(Printed in bold font, uppercase)*

*roman symbols*

<b>0</b>	zero matrix
<b>A</b>	state-space system matrix
<b>B</b>	state-space input matrix
<b>B<sub>m</sub></b>	modal state-space input matrix
<b>C</b>	state-space output matrix
<b>C<sub>m</sub></b>	modal state-space output matrix
<b>C(s)</b>	MIMO controller
<b>C(s<sub>i</sub>)</b>	value of MIMO controller at $s_i$
<b>D</b>	state-space feedthrough matrix
<b>E</b>	error term of TFD
<b>H<sub>dec</sub>(s)</b>	decoupled plant
<b>H(jω)</b>	frequency response of <b>H(s)</b>
<b>H(jω<sub>k</sub>)</b>	frequency response of <b>H(s)</b> at $j\omega_k$
<b><math>\hat{\mathbf{H}}(j\omega_k)</math></b>	measured frequency response of <b>H(s)</b>
<b>H(s)</b>	MIMO plant
<b>H(s<sub>i</sub>)</b>	value of <b>H(s)</b> at $s_i$
<b><math>\hat{\mathbf{H}}(s_i)</math></b>	estimated value of <b>H(s)</b> at $s_i$
<b>I</b>	identity matrix
<b>L(s)</b>	open-loop matrix ( <b>HC</b> )
<b>M</b>	matrix used to compute mode shapes via optimization
<b>N<sub>i</sub></b>	Matrix containing SISO notch in (1,1) entry for mode $i$
<b>R</b>	matrix containing sets of radii
<b>T<sub>in,i</sub></b>	input transformation matrix for mode $i$
<b>T<sub>out,i</sub></b>	output transformation matrix for mode $i$
<b>T<sub>u</sub></b>	input decoupling matrix
<b>T<sub>y</sub></b>	output decoupling matrix
<b>W</b>	weighting filter matrix

*greek symbols*

<b>Z</b>	matrix of damping values
<b>Φ</b>	matrix containing sets of angles
<b>Ψ</b>	modal participation matrix
<b>Ω</b>	matrix of eigenfrequencies

## Miscellaneous

$\dot{x}$	derivative of $x$ with respect to time
$\text{Im}(c)$	imaginary part of complex variable $c$
$\text{Re}(c)$	real part of complex variable $c$
$\angle(c)$	argument of complex variable $c$
$c^*$	complex conjugate of $c$
$\ker(\mathbf{M})$	kernel (null space) of matrix $\mathbf{M}$
$\mathbb{R}$	set of real-numbers
$\mathbb{C}$	set of complex-numbers
$\text{Var}[x]$	variance of $x$
$\text{Prob}[x]$	probability of $x$
$\text{diag}(d_i, \dots)$	diagonal matrix containing elements $d_i$ on its diagonal
$\odot$	element wise multiplication of matrices
$\oslash$	element wise division of matrices



# Chapter 1

## Introduction

**T**his chapter states the context and goals of the research presented in this thesis. An overview of feedback control of flexible motion systems is given after which the research approach and contributions are presented.

### 1.1 Advances in high-precision motion systems

#### 1.1.1 Accurate and fast positioning

Nowadays, products and production processes often contain positioning devices. For example, automated manufacturing techniques such as milling, turning and 3D-printing contain positioning devices to remove or add material at the right location on a product. Furthermore, they are found in assembly processes ranging from pick-and-place machines for small electronic components to the assembly lines for complete cars. But they are also used in many consumer products such as printers, hard-disk drives or optical drives. The positioning devices need a high accuracy in order to produce high-quality products. At the same time, the speed of these machines should be as high as possible to reduce the production cost. This renders the design of these devices a challenging problem.

Machines in the chip manufacturing industry are a prime example that illustrates the typical challenges of high-precision motion systems. Therefore, this application is chosen as a carrier for the research described in this thesis. The results presented in this thesis, however, are not limited to this specific application.



### 1.1.2 Integrated circuits

Over the past years, the functionality of integrated circuits (IC) has increased tremendously, while their costs have decreased. For example, in 1994 a 4 MB CompactFlash card would cost approximately 200 euro, while nowadays a 50 euro MicroSD card can hold 64 GB of data, see Figure 1.1. Similar trends have been observed for dynamic random access memory (DRAM) chips and central processing units (CPU) (Van den Brink, 2013).



Figure 1.1: 1994 CompactFlash card of 4 MB and a 2014 microSD card of 64 GB.

A large number of transistors per chip is required to increase the functionality of ICs. Miniaturization of the features of the ICs keeps the dimensions and power consumption within acceptable limits and increases the speed of the chip. At the same time, the production speed of these chips needs to be increased to reduce the costs. Hence, a highly accurate and fast production process is required.

ICs are produced on silicon disks, called *wafers*. The production process involves many steps, but the most critical step is lithography (Mack, 2008), see Figure 1.2. In this step, (extreme) ultraviolet light is used to project the chip design from a reticle onto the wafer, which is covered with a light-sensitive layer. Using various chemical processes, the projected image is converted into one layer of the electrical circuit. Typically, 20-30 layers are used to construct the complex structures of an IC.

The image of the chip design is projected in a scanning manner by moving the wafer and reticle with respect to each other. This increases the size of the exposed area and the imaging performance of the lens. The resulting lithography machines are called *wafer scanners*. To achieve the scanning motions very fast and accurate positioning stages are required. Current wafer scanners obtain an accuracy of a few nanometer, move at  $0.6 - 1 \text{ m/s}$  with accelerations up to  $40 \text{ m/s}^2$  and have a settling time of a few milliseconds (Butler, 2011).

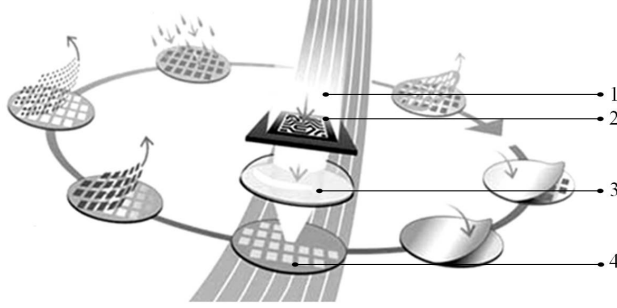


Figure 1.2: Lithography is a crucial step in the production process of integrated circuits. Ultraviolet light (1) is used to project the image of the chip design in the reticle (2) via the lens (3) on the wafer (4) (ASML, 2014).

### 1.1.3 Control of high-precision motion systems

Achieving both high speed and high accuracy poses a challenge to the control systems of the positioning stages, see e.g., (Butler, 2011). A simplified overview of the control schemes used in these machines is shown in Figure 1.3. Typically, magnetically levitated stages are used with the consequence that all 6 rigid-body degrees-of-freedom have to be actively controlled. To enable independent control of each direction of motion the multi-input multi-output (MIMO) system  $\mathbf{H}$  is decoupled using transformation matrices  $\mathbf{T}_u$  and  $\mathbf{T}_y$ . Both feedback  $\mathbf{C}_{fb}$  and feedforward  $\mathbf{C}_{ff}$  controllers are used to achieve fast and accurate positioning. Known disturbances (mainly induced by the reference trajectories  $\mathbf{r}$ ) are used to predict the required input  $\mathbf{u}_{ff}$ . The feedback controller stabilizes the system and counteracts unknown disturbances by computing a correcting input  $\mathbf{u}_{fb}$  based on the error signals  $\mathbf{e}$ .

The feedback controllers for these systems are designed by (manual) loop-shaping using frequency response data. As these systems are designed to exhibit predominantly linear, time-invariant behaviour, they are characterized by their frequency responses very well. Moreover, the frequency responses can be obtained accurately and at low cost, due to the availability of an accurate actuator and sensor system with a high signal-to-noise ratio. Loop-shaping is a method that is relatively straightforward to implement and to use. The dynamics of a magnetically levitated stage are dominated by the mass characteristics of the stage and by a number of high-frequency resonant vibration modes of the stage. This allows for a control design that consists of a limited number of filters, whose functionality

is well understood. Tracking of the reference trajectory is achieved by PID-type controllers in combination with feedforward controllers. Because the system can be decoupled very well, each degree-of-freedom can be tuned individually. The stage is designed such that the resonances, which can potentially endanger the stability, lie well above the target bandwidth. As a result, they can be suppressed by including only a few notch filters in the control loops.

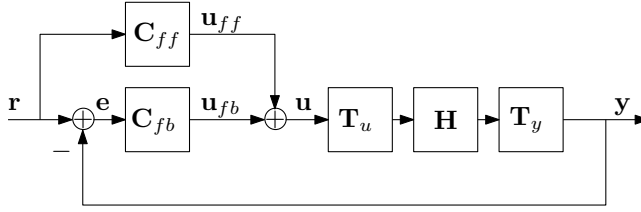


Figure 1.3: Control loop with feedback  $C_{fb}$  and feedforward  $C_{ff}$  controller to control the plant  $H$  which is decoupled using matrices  $T_u$  and  $T_y$ . The signals are: the reference  $r$ , the error  $e$ , the input  $u$  (which is the sum of the input due to feedback  $u_{fb}$  and feedforward  $u_{ff}$ ) and the output  $y$ .

#### 1.1.4 Challenges for high-precision motion systems

The specifications for the next generation of lithography machines will be more demanding in terms of accuracy and throughput. In van den Brink (2013) it is stated that resolutions will go below 10 nm in the near future. At the same time, the throughput must be increased to reduce production costs. This has implications on the required speed and accuracy of the positioning stages of these machines. To increase the accuracy, the bandwidth of the controllers should be increased for better disturbance rejection. At the same time, more aggressive motion profiles will be required to increase the speed, leading to larger disturbance forces, which again requires a higher bandwidth.

Another direction for increased throughput is to increase the size of the wafers from the current 300 mm to 450 mm as to reduce production overhead (Pettinato and Pillai, 2005). Obviously, this also requires larger positioning stages. Upscaling of current designs would lead to heavy stages. That is, if the requirement that the resonance frequencies have to lie well above the target bandwidth is maintained. This would mean that large actuator forces are required which lead to large disturbance forces and thermal issues due to the heat production of the actuators. Therefore, it is often advocated that the next generation positioning

stages will have to be lightweight (Makarovic et al., 2004; Oomen et al., 2014). A lightweight design leads to a decrease in stiffness of these systems, which causes the resonances to shift to lower frequencies. Furthermore, the disturbance rejection properties (obtained by virtue of Newton's second law) of a light stage are less favorable compared to a heavy stage. This poses a challenge for the control system design.

It is clear that the target bandwidths have to increase while the frequencies of the resonant modes might decrease. As a result, the flexible modes of these stages will lie around or even below the target bandwidths. These resonant modes typically have a low damping due to the materials that are used to construct motion stages. This means that a flexible mode that is excited by the control system or by external disturbances will deteriorate the performance of these systems. The currently used control designs use notch filters to cope with the vibration modes of these stages. A notch filter decreases the gain at the resonance frequency to prevent excitation of the flexible mode by the control system. However, this also causes the control system to lose control authority at the frequency of the mode, which is not desirable for frequencies below the bandwidth. It is clear that the current approach does not allow for active control of the flexible modes. Also, the flexible modes will hamper the decoupling of the system. The flexible modes will oscillate in directions that in general do not align with the rigid-body degrees-of-freedom. This introduces coupling between the rigid-body directions of motions at and above the resonance frequency of these flexible modes, which degrades performance.

## 1.2 Research objectives

### 1.2.1 The Xtreme Motion project

The research presented in this thesis is part of the Xtreme Motion project, a project funded by Senter Novem, an agency of the Dutch ministry of economic affairs. The goal of the project is to perform research for the next generation positioning devices that can be applied in the semiconductor industry. The project is conducted in close collaboration with the following industrial and academic partners: ASML, Bosch-Rexroth, Heidenhein, Magnetic Innovations, MI-Partners, Philips Innovation Services, Prodrive, Vision Dynamics Mechaphysics, Delft University of Technology and Eindhoven University of Technology. Five sub-targets have been defined to cover the broad range of research fields that play a role in the development of the next generation positioning devices, including dynamics, control, actuators and thermal effects:

1. dynamic optimization of actuator and sensor locations for over-actuation and over-sensing of non-rigid-body dynamics,  
Durango-Galvan et al. (2012)
2. development of control strategies of dynamic effects in non-rigid-body structures,  
Silvas et al. (2012); Bruijnen and van Dijk (2012)
3. development of an actuator concept with optimal force distribution and linearity,  
Vrijsen et al. (2014, 2013a,b)
4. development of control strategies for electromagnetic effects with spatial distribution in non-rigid-body structures,  
Katalenić (2013)
5. development of transient thermal models for frequency-dependent thermal sensitivity and real-time compensation strategies.  
Hooijkamp et al. (2012c,b,a)

The references included above are a selection of the publicly accessible results that are available at the moment of writing. These references provide a good starting point for further reading on these closely related research topics. The research described in this thesis is part of sub-target 2.

### 1.2.2 Scope and problem formulation

The goal of this research is to enable high-precision motion control for the next generation positioning devices, which exhibit flexible dynamics. The research focusses on the control design rather than the system design. Every system has its limitations, which might be overcome by improving the mechanical structure or by using more or better actuators and sensors. However, before the system design can be optimized, it is necessary to know how such a system can be controlled, given a particular configuration. Therefore, the mechanical structure and the number and locations of the actuators and sensors is assumed to be fixed beforehand. The systems considered in this thesis are thus characterized by

- a mechanical structure exhibiting multiple flexible modes with low damping,
- predominantly linear, time-invariant behaviour,
- multiple force inputs and position outputs at fixed locations,

- a performance location that can be located at any position on the mechanical structure.

The control systems of high-precision motion systems typically consist of a feedback and a feedforward controller, recall Figure 1.3. Although feedforward control is very important for performance, it is not considered in this thesis; the recent thesis by Ronde (2014) is completely devoted to this topic.

Furthermore, a data-based approach will be pursued, rather than a model-based approach. Although a large number of model-based control design techniques are available, obtaining an accurate model is no straightforward task. One approach is to model a flexible structure as a continuum described by partial differential equations, see e.g., Meirovitch (1997). This renders the system a distributed parameter system. Solutions for the partial differential equations are only available for very simple geometries such as beams and plates. To enable the analysis of more complex geometries Finite Element Modelling (FEM) techniques have been developed. However, the accuracy of these models can be limited for complex structures due to inevitable geometric differences between the model and the actual system that is built, due to assumptions on material behaviour and due to numeric approximations in the model. Furthermore, FEM models are typically of high order, which will lead to high-order controllers that cannot be implemented in practice.

Therefore, reduced-order models are often used for control design. These reduced order models can be derived from high-order models using model reduction techniques. Alternatively, low-order models can be obtained from fitting parametric models on measured data, see e.g., Pintelon and Schoukens (2001). In the field of vibration control, these reduced order models are often considered in a modal representation. This makes it possible to synthesize LQR,  $\mathcal{H}_2$ , or  $\mathcal{H}_\infty$  controllers that satisfy control goals specified for each mode, see Gawronski (2004); Preumont (2011). In motion control, model-based control has been considered for systems that exhibit predominantly rigid-body dynamics in Steinbuch and Norg (1998); de Callafon and van den Hof (2001); van de Wal et al. (2002). However, the combination of motion and vibration control is still a topic of ongoing research, see e.g., Oomen et al. (2014). Regardless of the chosen synthesis method a model-based control design is as good as the model that is used. Using a model with a large modelling error can lead to a controller that gives large control errors and can even lead to an unstable closed-loop system. Obtaining an accurate, low-order parametric model of the system to be controlled is not a straightforward task, as these systems have a large number of inputs and outputs as well as a large number of flexible dynamics (Van Herpen, 2014). Therefore an alternative approach is followed in this thesis.

The currently used control design methodology for high-precision motion systems, i.e., loop-shaping using frequency response data, leads to high-performance controllers. It would be desirable to extend this proven method such that it can better deal with the flexible dynamics of next generation motion systems. Two main aspects of flexible motion systems cannot be dealt with using the currently available methods. Firstly, the flexible dynamics will lead to oscillations with very low damping. Classical loop-shaping techniques are not suitable to design controllers to maximize the damping of the flexible modes. Secondly, the flexible dynamics result in a large number of deformation modes, giving the system complex directionality properties. Consequently, besides the six rigid-body directions, many flexible directions will become important in the control design and need to be taken into account. This leads to the problem statement of this thesis:

*Explore and develop frequency response data-based feedback control design methods that can address the flexible dynamics of advanced high-precision motion systems. These methods should be able to*

- *analyse and increase the damping of the flexible modes,*
- *incorporate the complex directionality of the flexible modes in the control design.*

## 1.3 Feedback control of flexible motion systems

This section briefly summarizes data-based feedback control design methods that are considered relevant for the control of flexible motion systems.

### 1.3.1 Frequency-domain data-based approaches

Data-based frequency-domain control design methods are often used to control high-precision motion systems. The main advantage of these methods is that frequency response data (FRD) can often be obtained at high accuracy and at low costs. Furthermore, the frequency-domain is well-suited to visualize the closed-loop sensitivities, the effect of plant uncertainty, disturbances and sensor noise.

## Loop-shaping

The best known FRD-based control design method is probably loop-shaping in the Bode diagram. Through Bode diagrams, the effect of loop-shaping filters on the magnitude and phase of the open-loop FRD is easily visualized as a function of frequency (Bode, 1945; Horowitz, 1963). Closed-loop performance and robustness against variations in the plant can be specified in terms of phase- and amplitude margins and bandwidth.

Alternatively, loop-shaping can be performed using the Nichols chart which plots magnitude against phase instead. The Nichols chart is well-known due to its use in *Quantitative Feedback Theory* (Horowitz, 1993). The advantage of this method is that it can deal with the uncertainties in the FRD in a straightforward way by introducing so-called QFT-bounds. The poles, zeros and gain of the controller are tuned on the basis of these bounds.

Although these loop-shaping techniques are limited to SISO systems, MIMO systems can be handled as well if the system can be decoupled in independent SISO systems. This approach is used in many high-precision motion systems, where the rigid-body degrees-of-freedom are decoupled using information about the geometry of the system. As the internal dynamics of high-precision motion systems are increasingly important for performance the flexible dynamics have to be taken into account.

This problem was also encountered in the '80s in the design of large space structures. Many of the challenges faced in high-precision motion systems are also found in the control of large space structures. Namely, the systems are difficult to model, have a large number of lightly damped resonant modes and very high specifications on positioning accuracy and vibration suppression (Balas, 1982). It was found that space structures could be modelled using a limited set of modes (Hughes, 1987). However, model-based controllers synthesized using a reduced-order modal model were hampered by spill-over effects; unmodelled modes that degrade the performance and could even cause instability.

A model-based approach was pursued in the control of large space structures, while in this thesis a data-based approach is preferred for reasons mentioned earlier. A method that is based on partial modelling of the system is modal decoupling. It only uses the (static) mode shapes and not a dynamical model of the system. Modal decoupling is described by Inman (1984) and applied in the motion control context for example by Makarovic et al. (2004); Schneiders et al. (2004); Friswell (2001); Anthonis and Ramon (2003). In modal decoupling often a number of flexible modes is decoupled in addition to the rigid-body directions of motion. The mode shapes can be identified using modal testing (Ewins, 1986) or from FEM



models. Any errors in the mode shapes will be visible in the interaction terms in the decoupled frequency response of the system. Moreover, the use of static transformation matrices cannot destabilize the system. By using the technique of sequential loop-closing (Hovd and Skogestad, 1994) the stability of the MIMO closed-loop system can be guaranteed. The disadvantage of this approach is that it requires sufficient actuators and sensors to actuate and observe the flexible modes. As more actuators and sensors are required compared to conventional rigid-body decoupling, this technique is sometimes referred to as *over-actuation* and *over-sensing* (Makarovic et al., 2004; Schneiders et al., 2004).

As stated in Skogestad and Postlethwaite (2005) directionality is the main difference between SISO and MIMO systems. It is the complicated directionality of the summation of all modes that makes it difficult to decouple all modes using a limited number of actuators and sensors. Apart from the directionality of the internal dynamics, the directionality of disturbances has to be included in the control design too (Skogestad and Morari, 1987). Boerlage et al. (2010) describe a method to design controllers that counteract disturbances in the appropriate directions. However, this method does not provide a way to cope with the internal directionality caused by the flexible modes.

Stability analysis of MIMO systems is also not straightforward if no parametric model of the system is available. For SISO systems, stability can be assessed by inspection of the Nyquist plot. Generalisations of this technique can be made by using the eigenvalues of the open-loop per frequency, which are called the *characteristic loci* (MacFarlane and Postlethwaite, 1977). Alternatively the Nyquist plot of the determinant of the return difference equation can be used (Brockett and Byrnes, 1981).

## Active vibration control

A number of techniques from the field of active vibration control (Gawronski, 2004; Preumont and Seto, 2008) can be applied without the use of a parametric model. These include positive position feedback (Goh and Caughey, 1985), lead control, direct velocity feedback (Balas, 1979) and integral force feedback (Preumont et al., 1992). For collocated actuator-sensor pairs, a robust method is obtained to add damping to resonant modes. The controllers are designed using classical loop-shaping techniques where the open-loop characteristics in the Bode diagram representation are shaped according to the specified gain and phase margins. However, without a model it is unclear how much damping is added by these controllers. Furthermore, dedicated actuator-sensor pairs for vibration control increase the amount of required actuators and sensors. This will certainly be a consideration for high-precision motion systems that already require the control

of six rigid-body degrees-of-freedom.

A lot of attention in the field of vibration control is given to the development of smart materials and structures. Smart materials are materials where strain can be generated by different mechanisms including temperature, electric- or magnetic fields (Preumont, 2011). These materials are characterized by a high level of integration of the actuators and sensors with the structure, which causes interaction between the actuator/sensor and system dynamics. Piezo actuators and sensors are often used in smart materials, see e.g. Inman (2001). Furthermore, electro-magnetic dampers are proposed in Jung et al. (2012). Again, additional actuators and sensors are required, which is why this approach is not pursued in this thesis. Besides, the addition of extra actuators and sensors may enable improved performance, but still the question remains how to design the controllers.

### Optimization based approaches

A number of frequency-domain methods have been developed that rely on optimization techniques to find a controller that satisfies a certain performance measure. QFT is one technique that lends itself for optimization if the QFT-bounds are parametrized, see e.g., Halikias et al. (2007); Molins and Garcia-Sanz (2009). Many results on the optimization of PID controllers are available. In Grassi et al. (2001), for example, the optimal PID parameters are found by integrating identification and control design by minimizing a weighted difference between the actual and a target loop transfer function. Keel and Bhattacharyya (2008) show the computation of the set of all stabilizing PID controllers that achieve a certain performance, specified by the phase or gain margin or by the  $\mathcal{H}_\infty$  norm. Furthermore genetic algorithms (Mitsukura et al., 1999) and swarm-based optimization (Gaing, 2004) are considered. Karimi et al. (2007); Karimi and Galdos (2010) propose to use linear programming with linear constraints in the Nyquist diagram to design a fixed-order  $\mathcal{H}_\infty$  controller. The advantage is that a convex optimization problem can be formulated, but with the disadvantage that the performance can only be specified as a lower bound on the crossover frequency.

The application of these optimization-based control design methods on high-precision motion systems is not straightforward. This is because it is not clear how to choose the cost function to account for the flexible modes of these systems. For example, the damping of the flexible modes cannot be included in this cost function as generally no accurate model of the flexible modes is available. Furthermore, the directionality of the flexible modes cannot be taken into account.

### 1.3.2 Time-domain data-based approaches

Besides frequency-domain data-based control, a number of time-domain data-based control design methods have been developed. One approach is to compute *Linear Quadratic Gaussian* (LQG) controllers from the Markov parameters of a set of input-output data (Skelton and Shi, 1994). This approach was extended to MIMO systems by Chan (1996). In Aangenent et al. (2005), this approach is implemented for the control of a robot arm. However, the performance was not satisfactory for high-precision motion control. The computational load of the algorithm puts constraints on the control horizon and sample rate, which degrades the performance. In data-based LQG, a closed-form solution of the Riccati equation is used to compute the controller that is optimal for a given cost function. As an alternative, gradient-based optimization of the cost function is considered. The difficulty in this approach lies in the approximation of the gradient of the cost function as no parametric model of the system to be controlled is available. For this purpose Spall and Cristion (1998) propose to use the *simultaneous perturbation stochastic approximation* method to optimize the controller parameters. Alternatively, *Iterative Feedback Tuning* (IFT) (Hjalmarsson and Gevers, 1998), can be used to compute an unbiased estimate of gradients of a given cost function. This method directly uses the data measured on the actual system. Lequin et al. (2003) use this method to optimize the parameters of a PID controller. However, IFT requires many experiments to compute the gradients as the number of inputs  $n_u$  and number of outputs  $n_y$  of the system increases. Namely,  $n_u n_y + 1$  experiments are required to estimate the gradients (Formentin et al., 2012).

A different approach was proposed in Cabral and Safonov (1996), which describe *unfalsified control*. In this approach, controllers are eliminated from a predefined set of feasible controllers if they do not satisfy the performance specifications. However, this technique is computationally demanding as the performance specification is given in terms of a solution to an expanding collection of quadratic inequalities (Cabral and Safonov, 2004). Therefore, in Cabral and Safonov (2004) it is proposed to use the ellipsoid algorithm to produce a sequence of decreasing volume ellipsoids which contains the set of unfalsified candidates. This reduces the computation time such that implementation is possible. In van Helvoort et al. (2008), this technique was successfully applied to an industrial inkjet printer at a sample rate of 1 kHz.

A method that can synthesize a controller from one set of input-output data is *Virtual Reference Feedback Tuning* (VRFT) (Campi et al., 2000). In this approach, the introduction of a virtual reference signal makes it possible to reduce the control design problem to an identification problem (Guardabassi and Savaresi, 2000). In Formentin et al. (2012) VRFT is used for fixed-order control design for MIMO systems. Experiments on a diesel engine show good reference tracking and decoupling

properties.

In Karimi et al. (2003) *correlation-based tuning* is described where the controller parameters are found by solving a correlation equation or minimizing the square of a cross-correlation function. In this way, the output error between the designed and achieved closed-loop system becomes uncorrelated with the reference signal. A major advantage of this method is that it is less sensitive to noise.

All these control design methods specify the performance in the time-domain via a certain cost function. Constraints on the time-domain signals can indirectly impose constraints on the damping of the flexible modes of high-precision motion systems. However, in the time-domain it is not easy to visualize the effect of plant uncertainty, disturbances and sensor noise. This renders the application of these methods for the control of high-precision motion systems often less straightforward.

## 1.4 Research approach and contributions

### 1.4.1 Towards data-based analysis and damping of flexible modes

It is clear that many frequency-domain data-based control design techniques are available. These methods are often used in practice as frequency response data (FRD) can be obtained accurately and at low costs. Performance specifications for these methods are given in the frequency-domain, which is desirable for stability and disturbance rejection properties. However the major disadvantage is that the frequency-domain does not provide direct information on the transient response of the closed-loop system. For high-precision motion systems, this implies that it is not clear how to analyse and increase the damping of the flexible modes of the system to be controlled. The reason for this is that it is not possible to directly compute the closed-loop poles from the FRD. Conventionally, a parametric model of the system is required to compute the closed-loop poles. As it was explained in Section 1.2.2, it is not straightforward to obtain such a model with sufficient accuracy. Therefore, a different approach is pursued in this thesis, which leads to the first contribution of this thesis.

**Contribution I:** *A data-based method to compute closed-loop poles.*

A data-based method is developed to compute the closed-loop poles of a system for a given controller without the need for a parametric model of the system to be controlled. This enables incorporating the closed-loop pole locations into the frequency response data-based control design methods. The first contribution consists of the following parts.

**Contribution I.A:** *A method to compute Transfer Function Data.*

The key concept in the method is the computation of Transfer Function Data (TFD). A computational method is developed to compute TFD from FRD using a Cauchy contour integral. The computational aspects and estimation errors are analysed in detail.

**Contribution I.B:** *Data-based computation of a root-locus.*

It is shown that the availability of TFD enables the computation of closed-loop poles without a parametric model of the system to be controlled. Moreover, for SISO systems a root-locus can be computed from the TFD. The closed-loop pole locations can be visualized as a function of a controller parameter. This allows the selection of the optimal value of this parameter with respect to the closed-loop pole locations, for example to maximize the damping of flexible modes.

**Contribution I.C:** *Data-based computation of closed-loop poles of MIMO systems.*

By extending the computation of TFD to MIMO systems the computation of the closed-loop poles of MIMO systems is enabled. This requires the computation of the determinant of the return difference matrix. TFD allows for data-based computation of this determinant, from which the locations and multiplicities of the closed-loop poles can be computed.

## 1.4.2 Towards incorporating directionality in the control design

It is clear that the first research contribution enables a data-based analysis of closed-loop poles of MIMO systems. In this way, the closed-loop poles of the flexible modes of high-precision motion systems can be analysed. However, this does not yet provide a control design method to control the flexible modes. One of the main challenges in the control of the flexible modes of MIMO systems is the directionality of these modes. Modal decoupling can be used to decouple the flexible modes, but this often requires extra actuator and sensor pairs. As high-precision motion systems typically have a large number of modes it is infeasible to decouple all modes. This gives the second research contribution of this thesis.

**Contribution II:** *Incorporating the directions of flexible modes in the feedback control design.*

It is shown that the directions of the flexible modes can be incorporated in the feedback control design without the use of extra actuators and sensors. The second contribution consists of the following parts.

**Contribution II.A:** *A numerical method to compute the directions of the flexible modes.*

The directions of the flexible modes are determined by their mode shapes. That is, the mode shapes are required in order to use the directionality in the control design. It is shown that the mode shapes can be computed from the frequency response data, without the need for a parametric model of the system.

**Contribution II.B:** *A design method for notch filters that accounts for directionality.*

A design method is developed to design notch filters for flexible modes of MIMO systems. The method takes the directionality of these modes into account by using the mode shapes computed in Contribution II.A. This method leads to a low-order controller that facilitates the tuning process.

## 1.5 Outline of the thesis

This thesis contains three research chapters. Each of the research chapters is based on a journal publication. In this way, each research chapter is self-containing and can be read independently.

### Chapter 2

This chapter addresses Contributions I.A and I.B and is based on the paper

Hoogendijk, R., van de Molengraft, M. J. G., den Hamer, A. J., Angelis, G. Z., Steinbuch, M., Computation of Transfer Function Data from Frequency Response Data with Application to Data-Based Root-Locus. *Under review for journal publication.*

In this chapter, the computation of TFD for SISO systems is described. It is explained that a root-locus can be computed from the TFD for a given controller. The results are validated on a benchmark experimental setup, where the approach is utilized to minimize the settling times encountered.

### Chapter 3

This chapter addresses Contributions I.A and I.C and is based on the paper

Hoogendijk, R., Heertjes, M. F., van de Molengraft, M. J. G., Steinbuch, M., Estimation of Closed-Loop Poles of MIMO Systems using Transfer Function Data. *In preparation for journal publication.*

MIMO TFD enables the computation of the determinant of the return difference in a data-based way. This enables computation of the closed-loop pole locations, including their multiplicity. The results are applied on an industrial prototype wafer stage. Firstly, the computed closed-loop pole locations are validated by making a comparison with time-domain data. Secondly, an example is included that shows how to incorporate the computed closed-loop poles in a control design

for the setup.

#### **Chapter 4**

This chapter addresses Contributions II.A and II.B and is based on the paper

Hoogendijk, R., Heertjes, M.F., van de Molengraft, M. J. G., Steinbuch, M.,  
Directional notch filters for motion control of flexible structures. *Mechatronics*, article in press, <http://dx.doi.org/10.1016/j.mechatronics.2014.01.011>

A new method to design notch filters for MIMO motion control systems with flexible mechanical structures is proposed in this chapter. The so-called directional notch filters take the directions of the targeted flexible modes into account using their mode shapes. The mode shapes are obtained from frequency response data using a new numerical optimization method. Experiments on a flexible beam setup demonstrate the feasibility of the proposed method in practice.

#### **Chapter 5**

In this chapter the conclusions are drawn and recommendations for future research are given.

## Chapter 2

# Data-based computation of closed-loop poles for SISO systems

**T**his chapter describes the computation and use of transfer function data (TFD) computed from frequency response data of a SISO system. TFD can be regarded as a sampled, data-based representation of the transfer function, which can be used to compute closed-loop poles without a parametric model of the system to be controlled. Computational accuracy and complexity are extensively discussed. As a use-case of TFD it is shown that a root-locus can be computed in a data-based way, using only frequency response data of a system. Experiments on a benchmark motion system demonstrate the use of TFD in minimizing settling times.

## 2.1 Introduction

Frequency-domain data-based control design methods have proven to be, and still are very successful in the analysis and design of controllers, especially for motion systems, see, e.g., Steinbuch and Norg (1998), Levine (2011). Accurate and fast tuning of high bandwidth controllers can be achieved using manual loop-shaping on frequency response data (FRD). Even today, many high-end industrial machines, for example wafer scanners, are controlled using PID controllers in combination with notch, low-pass and other filters as described in Butler (2011). In van de Wal



et al. (2001), it is stated that conventional (multiloop SISO) control is preferred because it is well understood, easy to tune, does not require a model, is easy to implement and gives satisfactory performance.

Due to the increasing performance requirements for high-precision motion systems, the internal dynamics are becoming increasingly important for the performance of these systems. The internal dynamics typically exhibit lightly damped resonances, that are conventionally suppressed using notch filters. To achieve a better performance, it is important to actively damp the resonances to improve the settling times. The damping of the resonances is determined by the time-constants of the closed-loop poles. However, currently used data-based control design methods cannot be used to analyse the damping of the closed-loop poles.

Model-based control design methods can be used to compute or even specify closed-loop poles. It is well known that classical techniques such as pole-placement or optimal control can be used for this purpose. In den Hamer et al. (2005), a control design method is presented in which information from a parametric model is used to enhance the loop-shaping process by incorporating information on the closed-loop pole locations. Also, results on robust control with constraints on pole locations have been reported, see for example Anderson and Moore (1969), Haddad and Bernstein (1992). Yet, application of model-based control on high-precision motion systems is not straightforward, because the synthesized controllers can be unstable and are typically of high order, as discussed in van de Wal et al. (2002). Furthermore, deriving an accurate low order parametric model for the control design of high-precision motion systems is not a straightforward task, which is why frequency-domain techniques are largely used in practice (Karimi and Galdos, 2010).

Recent advances in FRD-based control provide improved controller design tools compared to classic loop-shaping. Optimization-based computation of QFT controllers is often reported, see for example recent contributions by Molins and Garcia-Sanz (2009) or Halikias et al. (2007). Furthermore, Keel and Bhattacharyya (2008) show how to compute the set of all stabilizing PID controllers that achieve a certain performance, specified by the phase or gain margin or by the  $\mathcal{H}_\infty$  norm. Also, FRD based fixed-order  $\mathcal{H}_\infty$  control design is described in Karimi et al. (2007); Karimi and Galdos (2010). Performance specifications for these methods are given in the frequency-domain, which is good for stability and disturbance rejection properties. However, it is not clear how to specify damping of the resonant poles.

Time-domain data-based methods, such as data-based LQG (Skelton and Shi, 1994), Virtual Reference Feedback Tuning (Campi et al., 2000; Formentin et al., 2012) or Iterative Feedback Tuning (Hjalmarsson and Gevers, 1998) specify cost functions in the time- domain. Although these methods can be used to specify

the damping of the closed-loop poles in an indirect way, they do not combine well with the well established frequency-domain methods that are currently used for high-precision motion systems.

This chapter describes the computation and application of a data-based equivalent of the transfer function named *transfer function data* (TFD). Using TFD, controller design and analysis techniques that are formulated in terms of the transfer function of a system can be applied in a fully data-based way. TFD gives information on the value of the transfer function at every point in the complex plane. Therefore, it can be used to compute closed-loop pole locations. For SISO systems it is even possible to compute a root-locus completely data-based. In this way, closed-loop pole locations can be visualized in the control design without using a parametric model of the system to be controlled. TFD is computed from FRD, which makes the method a natural extension of manual loop-shaping. Moreover, TFD contains all dynamics of the system that are contained in the FRD, since the information about the system is not reduced to a small number of parameters as it is in the case of parametric modelling.

TFD can be computed from FRD if the system to be controlled is a stable and lightly damped resonant system. The method is well-suited for high-precision motion systems that are lightly damped as a result of the choice of materials that are used such as metals and ceramics, and the design principles applied that focus on lightweight and stiff construction. But also space structures and satellites, which have typical damping ratios in the range of 0.001 – 0.005, satisfy these conditions, see Preumont (2011).

The computation of TFD from FRD uses the Cauchy integral theorem from complex function theory. Rahman (1997) gives a comprehensive overview of this field of research. The Bode sensitivity integral, described in Bode (1945) and the Hilbert transform as used in Tesche (1992) are two examples of the application of Cauchy's theorem in the field of control theory. More recently, in den Hamer et al. (2008); den Hamer (2010) this integral is used to prove stability and causality of a system from its frequency response function. A first exploration of the use of TFD can be found in Hoogendijk et al. (2010), where TFD is used for frequency-domain optimal control.

In this chapter, the method to compute TFD for SISO systems is thoroughly investigated and experiments on a benchmark motion system are included. As a use-case, a root-locus is computed completely data-based using TFD. This allows prediction of the closed-loop pole locations and therewith minimization of the settling time of the system.

Summarizing, the main contributions of this chapter are:

- extensive discussion on the accuracy and computational aspects of transfer function data,
- data-based root-locus as a use-case for TFD,
- evaluation of the method on a benchmark motion system.

First, the computation of TFD will be explained in Section 2.2. Section 2.3 explains how to obtain accurate TFD and elaborates on the aspects in the computation that influence the accuracy of the method. Next, computational aspects are discussed in Section 2.4. Section 2.5 contains the theory on data-based root-locus plots. Finally, the experiments on a benchmark motion system are discussed in Section 2.6.

## 2.2 Computing TFD from FRD

### 2.2.1 Definition of TFD

Frequency response data (FRD) is defined to be a set of samples  $H(j\omega_k)$  of a transfer function  $H(s)$  at the points  $s = j\omega_k$ ,  $\omega \in \mathbb{R}$ . The subscript  $k = 1, 2, \dots, N$  is an index in the set of  $N$  data points, which can be obtained via available frequency response measurement techniques (Pintelon and Schoukens, 2001). FRD gives only partial information about  $H(s)$ , since the transfer function is only evaluated at points  $s = j\omega_k$  that lie on the imaginary axis of the  $s$ -plane. Therefore, the concept *transfer function data* (TFD) is introduced. TFD contains the response  $H(s_i)$  at complex frequencies  $s_i = \sigma_i + j\omega_i$ , where the subscript  $i = 1, 2, \dots, N_{tfd}$  is an index in the set of  $N_{tfd}$  data points. In  $s_i$ ,  $\omega_i \in \mathbb{R}$  is the imaginary part of  $s_i$ , while  $\sigma_i \in \mathbb{R}$  is the real part of  $s_i$ , which is the distance of the point  $s_i$  to the imaginary axis. In this way, TFD provides information about the system for a grid of points  $s_i$  in the complex plane and not only for the imaginary axis. As a result, TFD  $H(s_i)$  can be regarded as the data-based version of the transfer function  $H(s)$  of the system.

### 2.2.2 Use of TFD

TFD enables the use of data-based control design and analysis methods that cannot be applied to FRD directly. A clear example is the data-based computation of the closed-loop pole locations of a single-input-single-output system  $H(s)$  with

controller  $C(s)$ . It is well known that all transfer functions share the same denominator, consider for example the closed-loop transfer function  $T(s)$  and sensitivity  $S(s)$ , given by

$$T(s) = \frac{H(s)C(s)}{1 + H(s)C(s)}, S(s) = \frac{1}{1 + H(s)C(s)}. \quad (2.1)$$

From the denominators of (2.1) it is clear that closed-loop pole locations  $p_{cl}$  can be found by searching for points  $s$  in the complex plane that satisfy (Evans, 1950; Den Hamer et al., 2005)

$$p_{cl} = \{s \in \mathbb{C} \mid H(s)C(s) = -1\}. \quad (2.2)$$

FRD  $H(j\omega_k)$  is not sufficient to compute the closed-loop poles, since it only gives information about the value of  $H(s)$  on the imaginary axis. In general, the closed-loop poles will not lie on the imaginary axis. TFD on the other hand, gives information about  $H(s)$  for the whole complex plane, thereby enabling the data-based evaluation of (2.2).

### 2.2.3 Computation of TFD

The Cauchy integral formula (Rahman, 1997), described in the following theorem, is the basis for the proposed approach to compute the TFD.

**Theorem 2.1** (*Cauchy integral formula*) *Let  $g(s)$  be an analytic function in a region  $G$ ,  $\mathcal{C}$  a simple closed curve in  $G$  in anticlockwise direction and let  $\alpha$  denote a point in  $\mathcal{C}$ . Then*

$$g(\alpha) = \frac{1}{2\pi j} \int_{\mathcal{C}} \frac{g(s)}{s - \alpha} ds. \quad (2.3)$$

*Proof:* For the proof, see Rahman (1997). ■

Theorem 2.1 states that the value of a complex function at an arbitrary point in the complex plane that lies within a closed contour can be computed from the values of the function on the contour, provided that the function is analytic in this region.

Cauchy's theorem can be used to compute TFD from FRD in the right half-plane (RHP) as follows. Let  $H(s)$  be a stable, strictly proper system, such that  $H(s)$  has no poles in the RHP, which makes  $H(s)$  analytic in the RHP. This means that

it is possible to compute the value of the transfer function  $H(s_i)$  at any point  $s_i$  in the RHP by drawing a contour  $\mathcal{C}$  around the point  $s_i$  using

$$H(s_i) = \frac{1}{2\pi j} \int_{\mathcal{C}} \frac{H(s_C)}{(s_C - s_i)} ds_C, \quad s_i \in \mathbb{C}^+, \quad (2.4)$$

where

$$\mathbb{C}^+ = \{s \in \mathbb{C} \mid \text{Re}(s) > 0\}, \quad (2.5)$$

and where  $s_C$  are the points in the complex plane that lie on the contour  $\mathcal{C}$ . However, this requires the value of the transfer function at every point  $s_C$  on the contour to be known. Since a frequency response data-based approach is pursued, it is assumed that the value of the transfer function is only known on the imaginary axis. Therefore, a suitable choice for the contour  $\mathcal{C}$  is the D-contour  $\mathcal{C}_D$  depicted in Figure 2.1, which consists of the imaginary axis and a semicircle at infinity. For a strictly proper system, the response goes to zero when  $|s|$  goes to infinity. Moreover, the integrand of (2.4), has a relative degree of at least 2, such that the semicircle at infinity does not contribute to the integral. This reduces the contour integral to

$$H(s_i) = \frac{1}{2\pi j} \int_{-\infty}^{\infty} \frac{H(j\omega)}{(j\omega - s_i)} dj\omega, \quad s_i \in \mathbb{C}^+, \quad (2.6)$$

which is an integral over the imaginary axis. This can be rewritten as

$$H(s_i) = \frac{1}{2\pi} \int_{-\infty}^{\infty} \frac{H(j\omega)}{(s_i - j\omega)} d\omega, \quad s_i \in \mathbb{C}^+, \quad (2.7)$$

such that a real valued integration variable is obtained. Furthermore, the integration direction is reversed, which is accounted for by adding a minus sign to the denominator of the integrand ( $j\omega$  and  $s_i$  change place).

Equation (2.7) shows how TFD for the RHP can be computed from FRD using a Cauchy integral. This is not possible for the left half-plane (LHP), which is not an analytic region because it contains the poles of the system. However, lightly damped resonant systems, for which this method is developed, have poles and zeros that lie close to the imaginary axis, see Figure 2.1. This gives the TFD a certain symmetry that can be used to compute LHP TFD from RHP TFD. The specific symmetry condition that can be used depends on the system at hand. For systems with force actuators and position sensors, as is usually the case for motion systems, the transfer function can be written as a summation of  $N_m$  modes  $n$  with modal participation factor  $\Psi_n$ , frequency  $\omega_n$  and damping  $\zeta_n$  as in

$$H(s) = \sum_n^{N_m} \frac{\Psi_n}{s^2 + 2\zeta_n\omega_n s + \omega_n^2}. \quad (2.8)$$

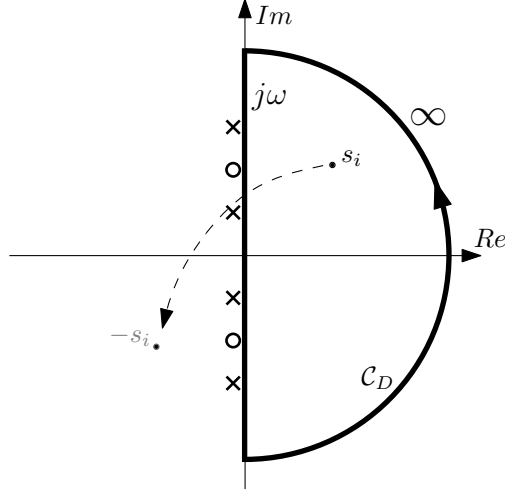


Figure 2.1: Contour in the  $s$ -plane used to compute TFD from FRD. The contour consists of the imaginary axis and a semi-circle at infinity.

When the system is lightly damped,  $\zeta_n \rightarrow 0$  such that

$$H(-s) = H(s), \quad (2.9)$$

since  $(-s)^2 = s^2$ . This makes it possible to approximate LHP TFD from RHP TFD.

Note that similar symmetry conditions could be derived for other classes of systems. For example, if it is known that all poles  $p_n$  lie at the same distance  $d$  from the imaginary axis,  $p_n = (-d + jw_n)$ . Then,

$$H(-s - 2d) = H(s) \quad (2.10)$$

would hold. Another example is a system that has velocity sensors instead of position sensors. In that case the transfer function can be written as

$$H(s) = \sum_n^{N_m} \frac{\Psi_n s}{s^2 + 2\zeta_n \omega_n s + \omega_n^2}, \quad (2.11)$$

such that

$$H(-s) = -H(s), \quad (2.12)$$

could be used.

Since TFD is computed from FRD, it cannot contain *more* information than the original FRD. However, the computation of TFD puts the data in a different format which makes the data *more usable*, as shown in the example of Section 2.2.2.

In this section, it has become clear that the computation of TFD is only possible if the system satisfies a number of constraints. These conditions can be summarized as follows. The system should be

1. stable, such that the contour integral around the RHP does not encircle any poles,
2. strictly proper, such that the response of the semi-circle at infinity does not contribute to the contour integral,
3. lightly damped, such that symmetry can be used to compute LHP TFD from RHP TFD.

## 2.3 Accuracy of TFD

In practice, the FRD of a system to be controlled will be measured at  $N$  frequencies  $\omega_k$ . Since knowledge of  $H(j\omega)$  is restricted to the points  $H(j\omega_k)$ , a numerical approximation of the integral (2.7) is required in the computation of the TFD. Several aspects of this numerical computation give approximation errors. The influence of these sources of inaccuracy will be discussed in the subsequent subsections, to explain how to accurately compute TFD.

Simulations have been performed to illustrate the influence of the various sources of inaccuracy that will be derived in the subsequent subsections. For this purpose, TFD will be computed for a known transfer function of a resonant system

$$H(s) = \frac{\omega_n^2}{s^2 + 2\zeta\omega_n s + \omega_n^2}, \quad (2.13)$$

where  $\omega_n = 10$  rad/s is the natural frequency and  $\zeta = 0.005$  is the damping ratio. FRD  $H(j\omega_k)$  for this model is obtained by evaluating this transfer function at a set of frequencies between 0.1 and 1000 rad/s, with a resolution of 0.1 rad/s. The FRD will be used in the computation of TFD using (2.7). The computed TFD  $H(s_i)$  will be compared to the transfer function  $H(s)$  from (2.13). The 3D-Bode magnitude plot of the transfer function is depicted in Figure 2.2. In a 3D-Bode magnitude plot, the magnitude of the TFD is plotted as a function of both the real and the imaginary part of the complex frequency  $s_i$  (Tsiotras, 2005).

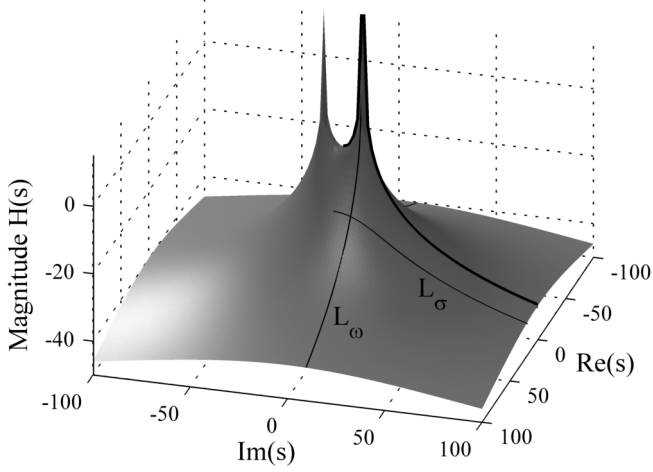


Figure 2.2: 3D-Bode magnitude diagram of the model. The bold solid line represents the FRD, while the lines indicated by  $L_\sigma$  and  $L_\omega$  are lines on which the TFD will be computed to assess the accuracy.

The accuracy of the TFD estimation depends on the point  $s_i$  at which the TFD is computed. Therefore, to assess the quality of the TFD, multiple points  $s_i$  have to be evaluated in the subsequent analysis. To be able to plot the result in a two dimensional graph, TFD is computed on different lines of points in the complex plane, as indicated by the lines  $L_\sigma$  and  $L_\omega$  in Figure 2.2. All points on the line  $L_\sigma$  have the same real part  $\sigma$  while points on the line  $L_\omega$  have the same imaginary part  $\omega$ . In the remainder of this section, the following error causes will be addressed: finite integral (Section 3.1), integration method and resolution (Section 3.2), influence of measurement noise (Section 3.3) and LHP TFD from RHP TFD (Section 3.4).

### 2.3.1 Finite integral

In practice, the infinite integral (2.7) cannot be computed, since the FRD can only be measured up till a certain maximum frequency  $\omega_{max}$ . Therefore (2.7) is rewritten as

$$H(s_i) = \frac{1}{2\pi} \int_{-\omega_{max}}^{\omega_{max}} \frac{H(j\omega)}{(s_i - j\omega)} d\omega + E_f(s_i), \quad s_i \in \mathbb{C}^+, \quad (2.14)$$



where the first term in this expression is the approximation of (2.7) that can be computed from TFD.  $E_f(s_i)$  is the error which is given by

$$E_f(s_i) = \frac{1}{2\pi} \int_{-\infty}^{-\omega_{max}} \frac{H(j\omega)}{(s_i - j\omega)} d\omega + \frac{1}{2\pi} \int_{\omega_{max}}^{\infty} \frac{H(j\omega)}{(s_i - j\omega)} d\omega, \quad s_i \in \mathbb{C}^+. \quad (2.15)$$

Figure 2.3 shows TFD of the example system (2.13) computed for different values of  $\omega_{max}$  to illustrate how the computation of TFD is affected when the FRD would be measured over a limited frequency range. The figure shows TFD computed at the line  $L_\sigma$  with  $\sigma = 10$ . This means that this Bode plot does not show the response of the system on the imaginary axis, but the response at  $s_i = \sigma + j\omega_i$  for a fixed  $\sigma = 10$  as a function of the frequency. From the figure it is clear that a higher value for  $\omega_{max}$  gives more accurate TFD, because a smaller part of the infinite integral is omitted. It can also be observed that the error increases when  $\text{Im}(s_i)$  is close to and above  $\omega_{max}$ . This is caused by the  $s_i - j\omega$  term in the denominator of (2.15) that acts as a weighting for each frequency point; points  $j\omega$  that lie close to the point  $s_i$  at which the TFD is computed, contribute more to the integral. Therefore, the higher the value of  $\text{Im}(s_i)$ , the more important the omitted part of the FRD is for the TFD as  $s_i$  lies closer to  $\omega_{max}$ . This analysis shows that  $\omega_{max}$  should be chosen as high as possible.

### 2.3.2 Integration method and resolution

Limitations in data storage and available measurement time make that the number of data points  $H(j\omega_k)$  to approximate (2.7) are limited. Hence, a numeric integration method has to be applied to compute (2.14). In this research the trapezoidal rule is used to approximate the integral in (2.14). The trapezoidal rule, given by

$$\int_a^b f(x)dx = \sum_{k=1}^{N_k-1} \frac{1}{2} [f(x_k) + f(x_{k+1})] \Delta x + E_i, \quad (2.16)$$

approximates the integral of a function  $f$  on an interval  $(a, b)$  by  $N_k$  trapezoids of width  $\Delta x$ . An upper bound for the integration error  $E_i$  can be obtained from (Adams, 1999)

$$E_i \leq \frac{K(b-a)^3}{12N_k^2}, \quad (2.17)$$

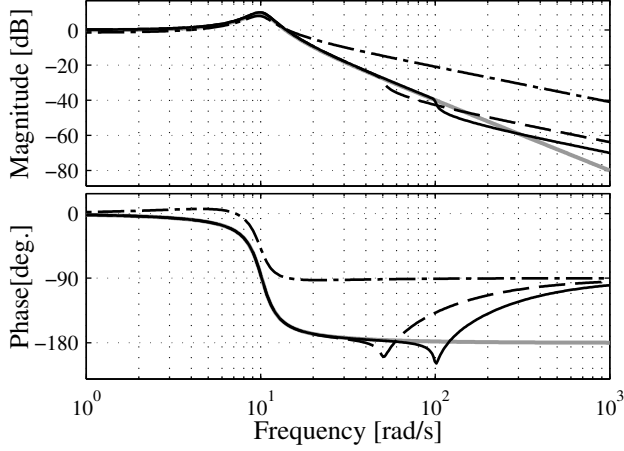


Figure 2.3: TFD from FRD with  $\Delta\omega = 0.1$  rad/s computed for the line  $L_\sigma$  with  $\sigma = 10$  for  $\omega_{max} = 100$  rad/s (solid), 50 rad/s (dash), 10 rad/s (dash-dot) and the model (grey).

where  $K$  is the maximum value of the second-order derivative of  $f$  with respect to  $x$ . As the error decreases with  $\frac{1}{N_k^2}$ , it is beneficial to take as many data points as possible. Applying the trapezoidal rule to the integral expression of (2.14) gives

$$\begin{aligned} H(s_i) &= \frac{1}{2\pi} \int_{-\omega_{max}}^{\omega_{max}} \frac{H(j\omega)}{(s_i - j\omega)} d\omega + E_f(s_i) \\ &= \frac{1}{4\pi} \sum_{k=-N}^{N-1} \left( \frac{H(j\omega_k)}{(s_i - j\omega_k)} + \frac{H(j\omega_{k+1})}{(s_i - j\omega_{k+1})} \right) \Delta\omega + E_i(s_i) + E_f(s_i). \end{aligned} \quad (2.18)$$

In practice, the FRD is measured at a discrete grid of  $N$  positive frequencies  $w_k$ . However, the integral of (2.14) contains both the positive and negative frequency axis. The value of the FRD on the negative frequency axis is easily obtained though, since it holds that

$$H(-jw) = H(jw)^*, \quad (2.19)$$

where  $*$  denotes the complex conjugate. Therefore the index  $k$  in (2.18) runs from  $-N$  until  $N-1$ , where a negative index of  $k$  as in  $\omega_{-k}$  denotes  $-\omega_k$  to incorporate both positive and negative frequencies.

To illustrate the influence of the resolution of the FRD, TFD is computed at line  $L_\sigma$  with  $\sigma = 10$ , for different resolutions of the FRD, see Figure 2.4. It can be seen

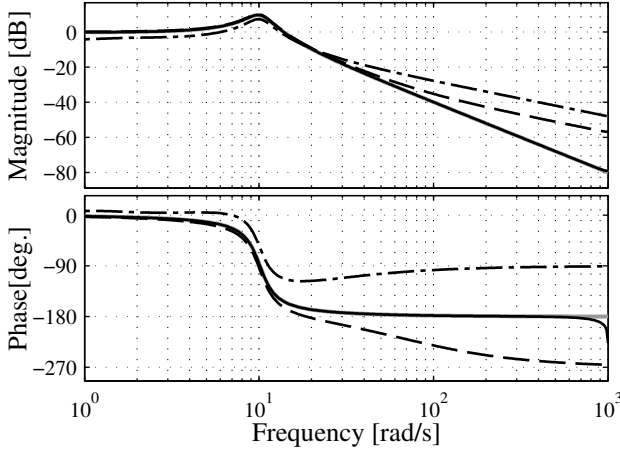


Figure 2.4: TFD computed at line  $L_1$  using FRD with  $\omega_{max} = 1000$  rad/s, for different resolutions;  $\Delta\omega = 0.1$  rad/s (solid),  $\Delta\omega = 1$  rad/s (dash),  $\Delta\omega = 10$  rad/s (dash-dot) and the model (grey, mostly covered by the solid curve).

that in this case, only the FRD points computed with resolution  $\Delta\omega = 0.1$  rad/s lie very close to the true values of the TFD points obtained from the model. The required resolution depends on the damping in the system. The lower the damping is, the sharper the peaks of the FRD of the system will be. Sharp peaks in the FRD result in a high second-order derivative of  $H(j\omega)$ , which will result in a large error according to (2.17). A rule of thumb that was found during simulations, is that  $\Delta\omega$  should satisfy

$$|\Delta\omega| < |\sigma_n|, \quad (2.20)$$

where  $\sigma_n$  is the real part of the pole  $p_n$  of the system that is the closest to the imaginary axis.  $\sigma_n$  can be estimated from the damping ratio  $\zeta$  and the natural frequency of the pole  $\omega_n$  according to (Franklin et al., 2002)

$$|\sigma_n| = |\zeta\omega_n|, \quad (2.21)$$

where the damping ratio will lie between 0.001 – 0.005 (Preumont, 2011) and the frequency of the pole can be estimated from the resonance peaks of the FRD. The frequency of the peak in the FRD is actually the *damped* natural frequency  $\omega_{nd}$  given by

$$\omega_{nd} = \omega_n \sqrt{1 - \zeta^2}. \quad (2.22)$$

However,  $\omega_{nd} \approx \omega_n$ , due to the low damping ratio. With a damping ratio that is in the order of  $10^{-3}$ , the difference between  $\omega_{nd}$  and  $\omega_n$  is in the order of  $10^{-6}$  due to the square in (2.22). Thus, as a rule of thumb

$$|\Delta\omega| < |\zeta\omega_{nd}|, \quad (2.23)$$

can be used in practice. To obtain FRD with sufficient resolution will thus require a two-step procedure. First, an initial measurement has to be conducted to have a rough idea of the value of  $\omega_{nd}$  and  $\zeta$ . Next, the FRD is measured with the appropriate frequency resolution determined using (2.23).

Note that the results of Figure 2.3 were also obtained using the numeric integration method described in this paragraph, with a resolution  $\Delta\omega = 0.1$  rad/s.

### 2.3.3 Influence of measurement noise

The FRD that is measured will contain a certain level of measurement noise, which will influence the computation of TFD. However, a point  $H(s_i)$  of the TFD is computed using a Cauchy integral over all FRD points, which reduces the effect of the noise, especially for points  $s_i$  that lie far from the imaginary axis. This can be seen as follows. Suppose the frequency response measurement  $\hat{H}(j\omega)$  contains zero mean circular complex noise  $\nu(j\omega)$  according to

$$H(j\omega) = \hat{H}(j\omega) + \nu(j\omega), \quad (2.24)$$

where  $H(j\omega)$  is the true frequency response. This means that (2.7) can be rewritten as

$$\begin{aligned} H(s_i) &= \frac{1}{2\pi} \int_{-\infty}^{\infty} \frac{H(j\omega)}{(s_i - j\omega)} d\omega \\ &= \frac{1}{2\pi} \int_{-\infty}^{\infty} \frac{\hat{H}(j\omega)}{(s_i - j\omega)} d\omega + \frac{1}{2\pi} \int_{-\infty}^{\infty} \frac{\nu(j\omega)}{(s_i - j\omega)} d\omega \\ &= \frac{1}{2\pi} \int_{-\infty}^{\infty} \frac{\hat{H}(j\omega)}{(s_i - j\omega)} d\omega + E_n(s_i). \end{aligned} \quad (2.25)$$

It can be observed that the error  $E_n(s_i)$  due to noise is an integral over  $\nu(j\omega)$ , filtered with  $(s_i - j\omega)^{-1}$ . For  $s_i$  values that are close to the imaginary axis, the filter is very sharp. This means that in that case the noise is less filtered, or even amplified. The farther the points  $s_i$  are located from the imaginary axis, the more

the noise is filtered. This implies that (2.18) becomes

$$\begin{aligned} H(s_i) &= \frac{1}{4\pi} \sum_{k=-N}^{N-1} \left( \frac{\hat{H}(j\omega_k)}{(s_i - j\omega_k)} + \frac{\hat{H}(j\omega_{k+1})}{(s_i - j\omega_{k+1})} \right) \Delta\omega + E_f(s_i) + E_i(s_i) + E_n(s_i) \\ &= \hat{H}(s_i) + E_f(s_i) + E_i(s_i) + E_n(s_i), \end{aligned} \quad (2.26)$$

where  $\hat{H}(s_i)$  denotes estimate of the TFD that can be computed numerically, i.e.,

$$\hat{H}(s_i) = \frac{1}{4\pi} \sum_{k=-N}^{N-1} \left( \frac{\hat{H}(j\omega_k)}{(s_i - j\omega_k)} + \frac{\hat{H}(j\omega_{k+1})}{(s_i - j\omega_{k+1})} \right) \Delta\omega. \quad (2.27)$$

From the variance of the FRD  $\text{Var}[\hat{H}(j\omega_k)]$  it is possible to compute the variance  $\text{Var}[\hat{H}(s_i)]$  of the estimated TFD  $\hat{H}(s_i)$ . From the standard properties of variance (Taboga, 2013), it is derived that

$$\text{Var}[\hat{H}(s_i)] = \frac{2}{16\pi^2} \sum_{k=-N}^{N-1} \left( \frac{\text{Var}[\hat{H}(j\omega_k)]}{|s_i - j\omega_k|^2} + \frac{\text{Var}[\hat{H}(j\omega_{k+1})]}{|s_i - j\omega_{k+1}|^2} \right) \Delta\omega^2. \quad (2.28)$$

Since the FRD on the negative frequency axis is computed from (2.19),  $\hat{H}(-j\omega_k)$  and  $\hat{H}(j\omega_k)$  are correlated, which explains the factor 2 in (2.28). Assuming that  $\hat{H}(s_i)$  has a circular complex normal distribution, a confidence circle for  $E_n(s_i)$  can be given. The probability  $P$  that the magnitude of  $E_n(s_i)$  is smaller than the radius of this circle is given by

$$P = \text{Prob}[|E_n(s_i)| < r_P \sigma_H(s_i)], \quad (2.29)$$

where

$$\sigma_H^2(s_i) = \text{Var}[\hat{H}(s_i)]. \quad (2.30)$$

$r_P$  can be computed for a given  $P$  according to

$$r_P = \sqrt{-\ln(1 - P)}. \quad (2.31)$$

For example, to ensure that the probability that the error lies within this bound is 99%,  $r_P = 2.15$  is chosen.

To illustrate this effect, TFD has been computed from a noisy FRD on two  $L_\sigma$  lines, one with  $\sigma = 0.1$  and one with  $\sigma = 10$ , see Figure 2.5. Circular complex noise from a normal distribution with zero mean and a standard deviation of 0.1 was used. The noisy FRD and computed TFD are plotted in grey. The FRD without noise and the value of  $H(s)$  at  $\sigma = 0.1$  and  $\sigma = 10$  obtained from the model are plotted in black. It can be observed that for  $\sigma = 0.1$  the noise is amplified, because the TFD is computed close to the imaginary axis. For  $\sigma = 10$ , however, the noise is filtered significantly.

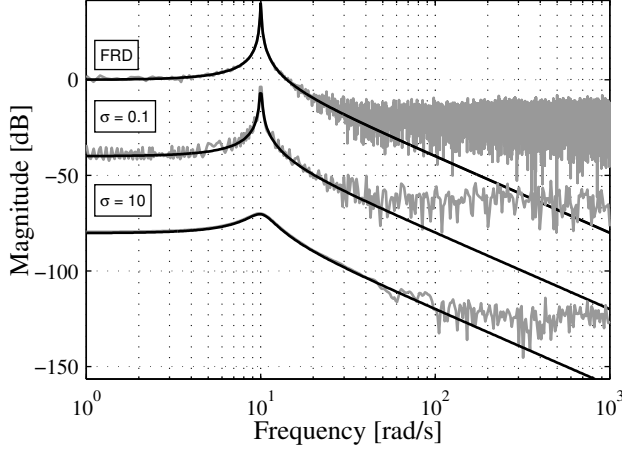


Figure 2.5: TFD computed from noisy FRD (top) at lines  $s_i = 0.1 + j\omega$  (middle) and  $s_i = 10 + j\omega$  (bottom) are shown in grey. Model-based results in black. Magnitudes for  $\sigma = 0.1$  and  $\sigma = 10$  are scaled with a factor  $1E-2$  and  $1E-4$  respectively to distinguish lines.

### 2.3.4 LHP TFD from RHP TFD

As mentioned previously, TFD in the LHP has to be obtained from RHP TFD using the symmetry condition (2.9). Since the poles of a real system will always have a certain amount of damping, an error will be made due to this approximation. The error  $E_s$  that is made in this approximation is equal to

$$E_s(s_i) = H(s_i) - H(-s_i). \quad (2.32)$$

Fortunately, the systems for which this method is developed, are very lightly damped ( $\zeta = 0.001 - 0.005$ ). To demonstrate that this is sufficiently small and to show what goes wrong for larger damping values, simulations have been performed. Figure 2.6 shows TFD on the line  $L_\omega$ , which is the line  $s = \sigma + 9.5j$ , for two models described by (2.13); one has damping ratio  $\zeta = 0.005$  (black) and the other  $\zeta = 0.5$  (grey). The line  $L_\omega$  of Figure 2.2 is now evaluated. Because it runs through both the LHP and the RHP, it shows the difference between RHP and LHP TFD. The true value of  $H(s_i)$  is plotted in dashed lines. It can be observed that the low-damped model is almost symmetric with respect to the imaginary axis, while the more damped model is not. The solid lines show the TFD that will be computed for the two models, which is the RHP TFD mirrored to the LHP according to (2.9). While for the lightly damped model the TFD lies close to  $H(s)$

obtained from the model, this is clearly not the case for the damped model. This illustrates that computing LHP TFD from RHP TFD is only possible for lightly damped systems.

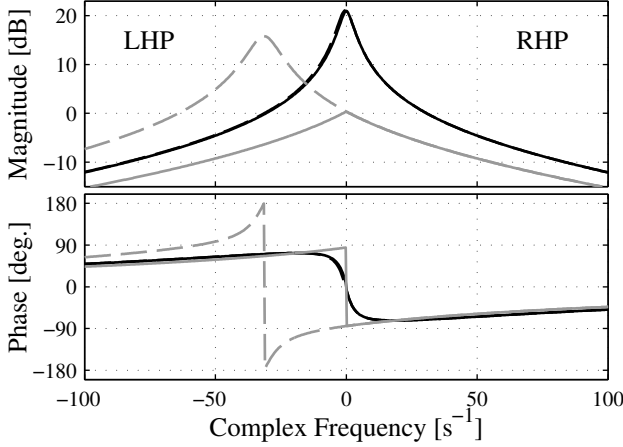


Figure 2.6: TFD computed at the line  $L_\omega$  for  $\omega = 9.5$  rad/s for  $\zeta = 0.005$  (black) and  $\zeta = 0.5$  (grey). Model-based results are indicated with a dashed line, while the computed TFD is plotted with a solid line.

### 2.3.5 Error bounds on TFD

The analysis presented in Section 2.3.1-Section 2.3.4 can be combined to compute the total error bound  $\Delta\hat{H}(s_i)$  on the computed TFD  $\hat{H}(s_i)$ . This error is defined to be

$$\Delta\hat{H}(s_i) = H(s_i) - \hat{H}(s_i). \quad (2.33)$$

where  $H(s_i)$  is the unknown, true value of the transfer function at  $s_i$ . An upper bound for  $\Delta\hat{H}(s_i)$  can be obtained by summation of the magnitude of the error terms discussed in the previous sections yielding

$$\Delta\hat{H}(s_i) \leq |E_n(s_i)| + |E_f(s_i)| + |E_i(s_i)| + |E_s(s_i)|. \quad (2.34)$$

Note that  $E_s(s_i)$  is zero in the RHP, since the symmetry condition is only used to compute TFD for the LHP. The computation of this error bound can be done in practice, but this requires the following approximations:

- An estimation of  $E_n(s_i)$  requires an estimation of the noise on the FRD, which can be done using standard frequency-domain identification techniques, see for example, Pintelon and Schoukens (2001).
- To estimate the error  $E_f(s_i)$  of the finite integration interval from (2.15) requires an estimation of the behaviour of the system for frequencies beyond  $\omega_{max}$ . As it is required that the system is strictly proper, the FRD has at least a minus-one slope at high frequencies. Assuming that all resonances lie below  $\omega_{max}$ , the FRD can be approximated by

$$H(j\omega) = \frac{c}{(j\omega)^n} \quad \text{for } \omega < -\omega_{max} \text{ and } \omega > \omega_{max}, \quad (2.35)$$

where  $c$  is a constant that can be computed from the FRD and  $n < -1$  is an approximation of the slope of the FRD at high frequencies. With this assumption, (2.15) can be computed analytically.

- The error due to the integration method  $E_i(s_i)$  can be obtained by estimation of the second-order derivative of the FRD with respect to  $\omega$ , such that (2.17) can be computed. This derivative could be obtained by locally fitting a smooth function on the FRD and computing the derivative thereof (Heath, 2005).
- Finally, in the LHP an estimate of the error due to the symmetry condition  $E_s(s_i)$  is required. This could be achieved by computing TFD  $H(s_i)$  in the LHP using the alternative symmetry condition (2.10), that assumes symmetry in the line  $\text{Re}(s_i) = -d$ . In this way, the TFD is computed as if all poles would lie at a distance  $d$  from the imaginary axis. This gives

$$|E_s(s_i)| = |\hat{H}(s_i) - \hat{H}(s_i - 2d)| \quad (2.36)$$

where  $d$  should be an estimate for the distance of the pole that has the largest distance to the imaginary axis. This is a valid approximation as taking the symmetry with respect to the imaginary axis underestimates the damping, while the alternative symmetry condition overestimates the damping. In reality, the damping will lie somewhere in between. Hence, taking the difference between these two extreme cases yields a good approximation of the error.



## 2.4 Computational aspects

### 2.4.1 Coping with undamped poles

Many systems contain undamped poles, i.e., poles that lie on the imaginary axis. For example, a motion system with rigid-body modes will have a transfer function that contains a double integrator. For systems with undamped poles, (2.7) cannot be used directly to compute  $H(s_i)$  from  $H(j\omega_k)$  because the contour does not lie in an analytic region due to the poles on the imaginary axis. Numerically, the computation goes wrong because the FRD will have a very high second-order derivative at the pole location which gives large errors in the computation according to (2.17).

A straightforward way to deal with this problem is to add a known weighting filter  $W(s)$  to the FRD in the computation step that cancels these undamped poles. After computing the TFD of the filtered FRD, the inverse filter can be applied to obtain TFD of the original system. The procedure is as follows. The FRD  $H(j\omega_k)$  is multiplied with the FRD of the filter  $W(j\omega_k)$  thereby cancelling the undamped poles, giving the filtered FRD

$$H_f(j\omega_k) = H(j\omega_k)W(j\omega_k). \quad (2.37)$$

Next, TFD  $H_f(s_i)$  is computed from the filtered FRD  $H_f(j\omega_k)$  using (2.7). Since the filter  $W(s_i)$  is known for all points  $s_i$ , it can be removed from  $H_f(s_i)$  according to

$$H(s_i) = \frac{H_f(s_i)}{W(s_i)}, \quad (2.38)$$

to obtain TFD  $H(s_i)$  of the original system. The filter  $W(s)$  consists of notch filters that are placed at the (estimated) frequencies of the undamped poles. The notches cancel the sharp peaks in the FRD thereby reducing the second-order derivative. The exact frequency at which the notches are placed is not important, since the effect of these filters is cancelled by (2.38). Figure 2.7 shows an example of this idea for the transfer function  $H(s) = 1000/s^2$ . A Bode plot with a linear frequency scale is used to show the infinite slope of the FRD at zero frequency (grey). A filter  $W(s) = s^2/(s - 20\pi)^2$  (grey dash) is used to cancel the undamped poles at  $s = 0$ , resulting in the filtered FRD (black). This filtered FRD can be used in (2.7), while the original FRD could not.

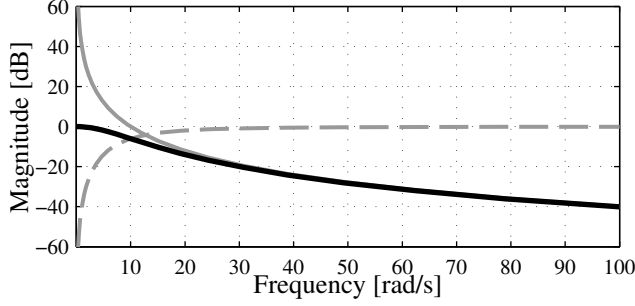


Figure 2.7: FRD of a system containing undamped poles at  $s = 0$  (grey), weighting filter (grey,dashed), weighted FRD (black).

### 2.4.2 Computation time

For each TFD point  $\hat{H}(s_i)$  that is computed, a summation over all FRD points is performed. As mentioned before, it is beneficial to take as many points as possible. This gives rise to the question whether the computations can be performed in a reasonable amount of time with sufficient accuracy. To assess this, the value of the transfer function data of the resonant system (2.13) is computed at an arbitrarily chosen point  $s_i = 8 + 16j\pi$  using a varying number of FRD points  $N$ . Figure 2.8 shows a graph of computation time in seconds and relative error  $E_r$  defined by

$$E_r(s_i) = \frac{|H(s_i) - \hat{H}(s_i)|}{|H(s_i)|}, \quad (2.39)$$

where  $H(s_i)$  is the TFD and  $H(s)$  is the value of the transfer function obtained from the model. Simulations were performed on a standard pc with a 2.5 GHz dual-core processor and 4GB of RAM memory. For  $N < 10^4$  both the computation time and accuracy do not show a clear trend. For such a small number of points, the accuracy depends on how well the data is represented by the chosen frequency grid. For example, by the choice of the grid, the resonance peak of (2.13) could lie exactly between two data points resulting in low accuracy. The short computation times will be influenced largely by the overhead of the computer and not the actual computation time of the algorithm. For  $N > 10^4$ , however, the trend is clearly visible. It can be observed that the computation time  $t_{comp}$  is proportional to the number of data points, thus

$$t_{comp} \propto N_k. \quad (2.40)$$

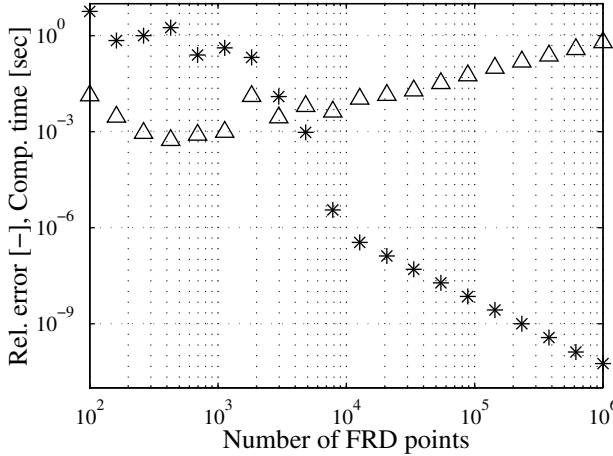


Figure 2.8: Computation time ( $\Delta$ ) and relative error ( $*$ ) to compute one TFD point at  $s_i = 8 + 16j\pi$ .

The relative error on the other hand shows that

$$E_r \propto N_k^{-2}, \quad (2.41)$$

which agrees with (2.17). It can be observed that an accuracy of  $10^{-6}$  can be obtained with  $\sim 10^4$  points. In that case, the computation of one TFD point only takes approximately 9 milliseconds. One TFD point, however, is not very useful, normally a grid of points is required to analyse a system in the s-plane. The short computation times show that it is feasible to compute TFD for a whole grid of points in a few seconds with reasonable accuracy.

### 2.4.3 Amount of human interaction

A data-based method is only attractive if it is more accurate or easier to apply than model-based methods. In this case, the simplicity of the method is one of the major advantages. The required amount of human interaction for this method is limited. Provided that the system satisfies the requirements; lightly damped and zero response at infinite frequency, and that sufficiently accurate FRD is available, the only freedom is the selection of the points  $s_i$  at which the TFD is computed. As the goal of TFD is to compute closed-loop pole locations in a data-based way, the range for the points  $s_i$  is chosen properly if all closed-loop poles that are relevant for the control design lie within the range. For the imaginary part of  $s_i$ ,

corresponding to the frequency axis, the interesting values of the s-plane can be observed from the FRD. Since the closed-loop poles travel from their open-loop pole locations to the zeros of the system, the frequencies at which the open-loop poles and zeros of the system are located indicate the interesting range for  $s_i$ . The range for the real part of  $s_i$  has to be determined experimentally, as it is unknown how far the poles will travel into the LHP. However, since the method is fast, iterating over possible interesting ranges is not very time-consuming.

As the TFD is computed on a discrete grid of points  $s_i$ , the accuracy of the computed closed-loop pole location is, in theory, limited by the grid density. However, the grid density itself can be taken arbitrarily high, provided that sufficient computation time and memory is available. Moreover, in practice it was found that the inaccuracy of the computation of TFD at each point  $s_i$ , as discussed in Section 2.3 is of more influence on the final result than the discretization of the s-plane.

Note that systems with undamped poles also require the selection of an appropriate filter  $W(s)$  as discussed in Section 2.4.1.

Summarizing, the following aspects require some human interaction in the method:

1. estimation of the damping of the poles, see (2.23), to determine the correct resolution for the FRD,
2. determination of the relevant range of the s-plane,
3. design of a weighting filter  $W(s)$  in case undamped poles are present.

## 2.5 Use-case: Data-based Root-locus

As mentioned in Section 2.2.2, TFD can be used to compute the closed-loop poles of a system under feedback control. In this section it will be shown that it is not only possible to compute the closed-loop poles for a given controller, but that it is also possible to draw the root-locus for this controller in a fully data-based way, using TFD. In this section, the parameter in the root-locus is chosen to be the gain  $k$  of the controller  $C(s)$  from (2.2). By taking  $k$  out of the controller according to

$$C(s) = k\overline{C}(s), \quad (2.42)$$

where  $k \in \mathbb{R}$ , (2.2) becomes

$$\begin{aligned} p_{cl}(k) &= \{s \in \mathbb{C} \mid kH(s)\overline{C}(s) = -1\} \\ &= \{s \in \mathbb{C} \mid H(s)\overline{C}(s) = -\frac{1}{k}\}, \end{aligned} \quad (2.43)$$

where the closed-loop poles  $p_{cl}(k)$  now depend on the gain of the controller  $k$ . From (2.43) it is clear that points in  $H(s)\overline{C}(s)$  that have *zero imaginary part* and a *negative real part* belong to the root-locus. However, a discrete grid of points  $s_i$  is used, which means that (2.43) is only evaluated at  $s = s_i$ . In general,  $\text{Im}(\hat{H}(s_i)\overline{C}(s_i))$  will not exactly be equal to zero for any point  $s_i$ .  $\text{Im}(\hat{H}(s)\overline{C}(s))$  will be zero somewhere between the data points  $s_i$ . Figure 2.9 illustrates this. In the figure, the point  $s_i$  has two neighbouring points where  $\text{Im}(\hat{H}(s_i)\overline{C}(s_i))$  changes sign (for the algorithm only the four closest neighbours are considered). Since the underlying transfer function is analytic on the whole s-plane (except for a few isolated points; the poles of  $H(s)\overline{C}(s)$ ),  $\text{Im}(\hat{H}(s_i)\overline{C}(s_i))$  must be equal to zero somewhere between these points. An estimation of this point is made using linear interpolation. Considering point  $s_i$  and its neighbour  $s_j$  as indicated in the figure, the zero crossing  $\hat{p}_{cl}$ , which is an estimate of the closed-loop pole location, is given by

$$\hat{p}_{cl} = s_i + \alpha(s_j - s_i), \quad (2.44)$$

where

$$\alpha = \frac{\text{Im}(\hat{H}(s_i)\overline{C}(s_i))}{\text{Im}(\hat{H}(s_j)\overline{C}(s_j)) - \text{Im}(\hat{H}(s_i)\overline{C}(s_i))}. \quad (2.45)$$

However, according to (2.43), the corresponding gain is not only real, but also negative, therefore it is checked whether

$$H(\hat{p}_{cl})\overline{C}(\hat{p}_{cl}) < 0, \quad (2.46)$$

where linear interpolation is used again to compute

$$H(\hat{p}_{cl})\overline{C}(\hat{p}_{cl}) = \hat{H}(s_i)\overline{C}(s_i) + \alpha(\hat{H}(s_j)\overline{C}(s_j) - \hat{H}(s_i)\overline{C}(s_i)). \quad (2.47)$$

The complete root-locus is constructed by performing a search over all data points  $s_i$ . For the root-locus points that are found, the corresponding gain  $k$  can be computed from

$$k = \frac{-1}{H(\hat{p}_{cl})\overline{C}(\hat{p}_{cl})}. \quad (2.48)$$

In this way it is possible to use the data-based root-locus to compute the gain that is required to obtain the desired closed-loop pole locations.

## 2.6 Results on a benchmark motion system

The proposed method is applied to a benchmark motion setup, see Figure 2.10. The system consists of two inertias connected via a rotational spring. A schematic

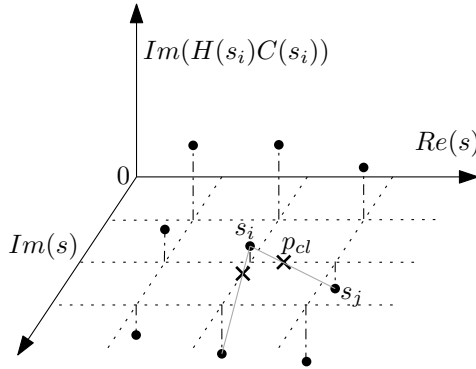


Figure 2.9: The root-locus points ( $\times$ ) are found from linear interpolation between the data-points  $Im(\hat{H}(s_i)C(s_i))$  ( $\bullet$ ) to compute where the data crosses the zero plane.

drawing of the setup is shown in Figure 2.11. The input  $u$  to the system is supplied by a DC motor and the output  $y$  of the system is the position of the inertia on the motor side measured by the motor encoder.

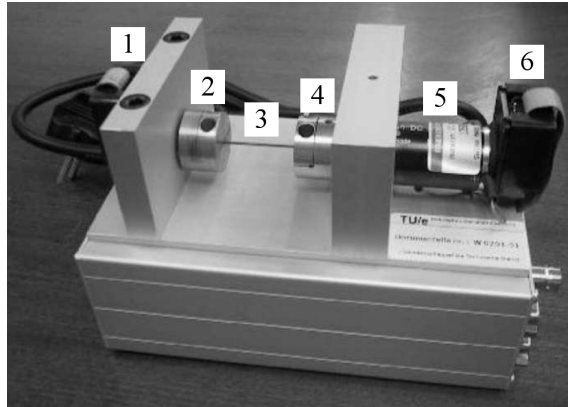


Figure 2.10: Experiment setup: 1: load encoder, 2: inertia at load side, 3: rotational spring, 4: inertia at motor side, 5: motor, 6: motor encoder.

The control objective is to perform a point-to-point motion. A third-order set-point is designed for this purpose and mass feedforward is added. Because the system is lightly damped, oscillations will occur during the motion that have to

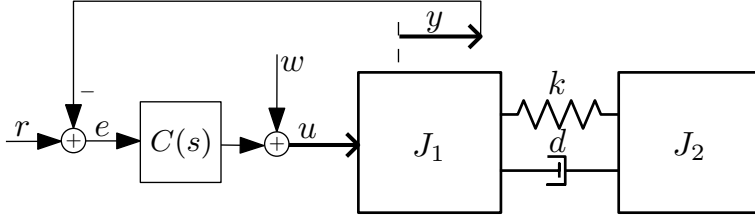


Figure 2.11: Schematic representation of the experimental setup with collocated controller.

be damped by the feedback controller  $C(s)$ . This controller is designed using loopshaping techniques and consists of a gain, lead filter and low-pass filter. The goal of the controller is to damp the oscillations that will occur, but tuning of the controller for this purpose is not straightforward. The time-constant of the oscillations is determined by the real part of the closed-loop poles. The amplitude of the oscillation due to a closed-loop pole with real part  $\sigma_p$  will be governed by  $e^{\sigma_p t}$ , ( $\sigma_p < 0$ ). However, the closed-loop pole locations cannot be determined directly from the commonly used control design plots such as open-loop/sensitivity Bode diagrams or Nyquist plots. In these experiments it will be shown that TFD can give a quick and easy-to-compute estimation of the closed-loop pole locations, without computation of a parametric model of the system. A root-locus will be computed in a fully data-based way, which will be used to tune the gain of the controller such that the closed-loop poles lie as far as possible in the LHP, thereby giving the fastest decay rate of the oscillations. The method is validated in two ways. Firstly, the TFD is compared to a parametric model that is computed for the system. Secondly, the response in the time-domain is measured to validate the predicted closed-loop poles from the data-based root-locus. Summarizing, the following steps will be performed:

1. obtaining FRD of the system,
2. computation of TFD  $\hat{H}(s_i)$  from FRD using (2.27),
3. computation of the data-based root-locus using (2.44),
4. time-domain evaluation of the performance of the controller.

### Step 1: Obtaining FRD of the system

The FRD of the system is obtained from a closed-loop identification experiment. A multisine excitation signal of  $N_p = 60$  periods with Schroeder phase was supplied to the system according to the theory described in (Pintelon and Schoukens, 2001). A three-point measurement method is used where the sensitivity and complementary sensitivity are estimated by exciting at  $w$  and measuring  $e$  and  $u$ , as indicated in Figure 2.11. The FRD is measured at frequencies between 0.63 and 6283 rad/s with a resolution of 0.63 rad/s, see Figure 2.12. The total variance of the FRD, plotted in grey in the figure, is computed from

$$\text{Var}[\hat{H}(j\omega)] = \frac{1}{N_p(N_p - 1)} \sum_{k=1}^{N_p} |\hat{H}(j\omega) - \hat{H}_k(j\omega)|^2, \quad (2.49)$$

where  $\hat{H}_k(j\omega)$  is the FRD computed per period and  $\hat{H}(j\omega)$  is the sample mean over all periods. Note that due to the choice for a Schroeder phase, it is not possible to distinguish between noise variance and total (noise plus nonlinear distortions) variance. In the application at hand, only the total variance is of interest as the non-linearity of the system is outside the scope of our work. For other applications, however, a random multisine approach could be pursued to discriminate between noise variance and total variance, see Pintelon and Schoukens (2001). To compensate for the delay in the measurement system, a delay compensation  $e^{j\omega\tau}$  with  $\tau = 5.5 \cdot 10^{-4}$  seconds is added to the FRD. If this delay is not be compensated for, the damping of the closed-poles is generally be estimated too low as the delay increases the phase lag.

To verify that the FRD is measured with sufficient resolution, (2.23) can be used, if an estimate of the damping ratio  $\zeta$  is available. For this setup it is estimated that  $\zeta \approx 0.002$  (the value found for the parametric model described in the last part of this section). The poles appear in the FRD at a frequency of 368 rad/s. Thus  $\zeta\omega_d = 0.002 \cdot 364 = 0.73$ , which shows that (2.23) is satisfied.

For verification purposes, a parametric model  $H_{mod}(s)$  is fitted on the FRD manually. From the FRD it is observed that the main dynamics are caused by a double integrator, a complex pair of zeros and a complex pair of poles. This gives the following model structure

$$H_{mod}(s) = c \frac{s^2 + 2\zeta_m\omega_{zm}s + \omega_{zm}^2}{s^2(s^2 + 2\zeta_m\omega_{pm}s + \omega_{pm}^2)}. \quad (2.50)$$

The value for the frequency of the zero  $\omega_{zm} = 275$  rad/s and the pole  $\omega_{pm} = 368$  rad/s were obtained by reading these values from the measured FRD. Next, the gain  $c = 6.7 \cdot 10^3$  was tuned manually such that the gain of the model matches the



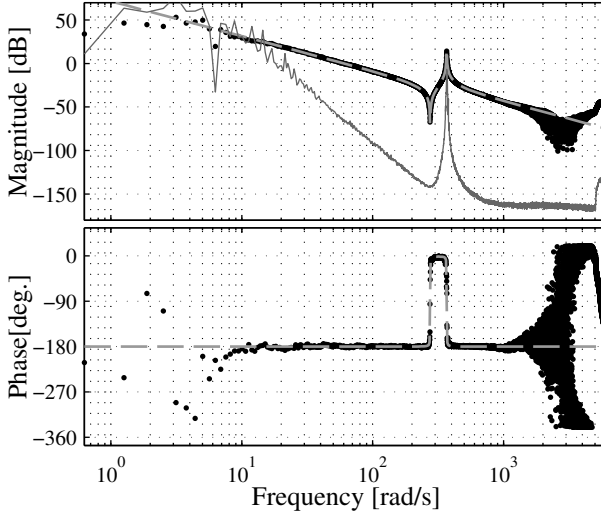


Figure 2.12: Measured FRD of the experimental setup (black), variance of FRD (grey) and parametric model (grey dashed).

gain of the FRD at frequencies between 20 – 100 rad/s. Finally, the damping ratio  $\zeta_m = 0.002$  was adjusted such that the peak value of the resonance of the model is equal to the peak value of the resonance of the FRD. This model, plotted with a grey dashed line in Figure 2.12, will be used to verify the data-based root-locus that will be computed in the third step. It must be emphasized that this model is used only for validation of the method, it is not used in any of the steps in the computation of TFD. For this benchmark system, fitting a parametric model is an easy task. Creating an accurate low-order parametric model for a more complex system will be much more cumbersome. The TFD-based approach on the other hand can be applied to complex systems with the same effort as for this benchmark system.

## Step 2: Computing TFD from FRD

The next step is to compute TFD from the measured FRD. Since the system has pure integrators, the approach of Section 2.4.1 is used to compute TFD for the

RHP. The weighting filter  $W(s)$  that was used is

$$W(s) = \frac{s^2}{s^2 + 2\beta_W\omega_W s + \omega_W^2}, \quad (2.51)$$

where  $\beta_W = 0.6$  and  $\omega_W = 60 \text{ rad/s}$ . The  $s^2$  term in (2.51) cancels the pure integrator of the plant exactly, while the denominator ensures that the influence of the filter is limited to the low frequency range to prevent amplification of noise at high frequencies. Systems that have undamped poles that are not exactly known can potentially pose a problem. When the undamped poles are not cancelled exactly, large 2nd derivatives may still exist, which lead to large errors according to (2.17). However, in the mechanical motion systems that we have encountered so far only the pure integrators have to be cancelled with this method. As the specific values of  $\beta_W$  and  $\omega_W$  do not influence the removal of the pure integrators, this freedom is utilized to reduce the amplitude of the filtered FRD at low frequencies, where the accuracy of the FRD is less due to the limited measurement time.

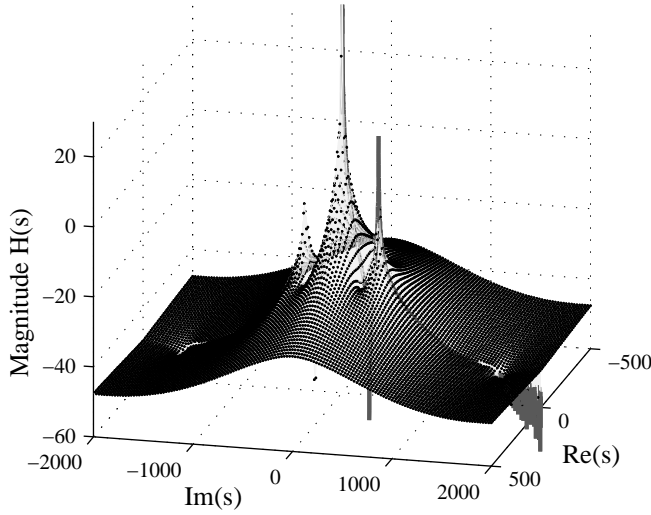


Figure 2.13: 3D-Bode magnitude diagram of the TFD of the experiment setup. The grey line represents the measured FRD.

TFD for the LHP is obtained from the RHP TFD by applying (2.9). Figure 2.13 shows the 3D-Bode diagram of the computed TFD. The conventional Bode magnitude plot is the part of the response on the positive imaginary axis ( $s_i = j\omega$ ), indicated by a grey line on the positive imaginary axis in the figure. The range of values of  $s_i$  for which the TFD is computed is  $-500 < \text{Re}(s_i) < 500$ ,  $-2000 <$

$\text{Im}(s_i) < 2000$ . This range is selected since it is expected that the closed-loop poles lie in this area. For increasing controller gains, the closed-loop poles will travel from the open-loop pole locations to the zeros of the plant, or to infinity. Therefore, the imaginary part of  $s_i$  is chosen such that the frequencies of the open-loop poles lie within this range. Selection of the range for the real part  $s_i$  is done in an iterative way. The range was adjusted such that the root-locus, computed in Step 3, shows the asymptotic behaviour of both the poles at  $s = 0$  and the poles of the resonance of the system. The adjustment of the range is done as follows. If no root-locus points are visible, the range is decreased as the zero crossings probably lie in between grid points. If on the other hand some root-locus points are visible, but the asymptotic behaviour cannot be observed, the range is increased.

The error bounds on the TFD  $\Delta\hat{H}(s_i)$  are computed using the methods described in Section 2.3. The details of the computation of the four contributions to this error as given in (2.34) are as follows:

- The variance on the TFD  $\text{Var}[\hat{H}(s_i)]$  is computed from the variance of the FRD as computed using (2.49). To estimate the error bounds,  $r_P = 2.14$  is used in equation (2.29), corresponding to a 99% confidence that the error lies within these bounds.
- The error  $E_f(s_i)$  due to the finite integral (2.14) that is used instead of the infinite integral (2.7) is computed using (2.35), taking  $n = 2$ ,  $\omega_{max} = 6283$  rad/s.
- The error due to numeric integration  $E_i(s_i)$  is computed from (2.17), where  $a = -\omega_{max}$ ,  $b = \omega_{max}$ ,  $N_k = 10^4$  and  $K$  is computed using straightforward numeric differentiation. Denoting the integrand of (2.18) by

$$I(\omega_k) = \frac{H(j\omega_k)}{s_i - j\omega_k}, \quad (2.52)$$

the second-order derivative is computed using

$$\frac{d^2 I(\omega_k)}{d\omega_k^2} = \frac{I(\omega_{k-1}) - 2I(\omega_k) + I(\omega_{k+1}))}{(\Delta\omega)^2}. \quad (2.53)$$

- The extra error contribution  $E_m(s_i)$  in the LHP is estimated using (2.36) where  $d = \zeta_{max}\omega_{nd} = 0.01 \cdot 364 = 3.64$  is used to estimate the worst case damping of the resonant pole.

### Step 3: Computation of the data-based root-locus

For the system under consideration it is known that high damping of the resonance is obtained when the open-loop transfer function crosses the 0 dB line somewhere between the zero and the pole. To achieve this, phase lead is required in a broad frequency range because the open-loop will cross the 0 dB line three times. Furthermore, a low-pass filter is added to suppress high frequency disturbances and sensor noise. The controller that is used is given by

$$C(s) = k \frac{\frac{s}{\omega_1} + 1}{\frac{s}{\omega_2} + 1} \frac{1}{\frac{s^2}{\omega_{lp}^2} + \frac{2\beta_{lp}s}{\omega_{lp}} + 1}, \quad (2.54)$$

with  $\omega_1 = 125$  rad/s,  $\omega_2 = 2500$  rad/s,  $\omega_{lp} = 4400$  rad/s and  $\beta_{lp} = 0.3$ . The gain  $k$  is initially set to 1 to compute the root-locus, but this initial value is arbitrary. The root-locus will be used to compute the optimal gain for this controller.

TFD  $C(s_i)$  is generated for the controller by evaluating (2.54) at the TFD points  $s_i$ . Next, the approach of Section 2.5 is used to search for points that belong to the root-locus. Recall that these are the points at which  $\hat{H}(s_i)C(s_i)$  is negative and real. These points are plotted in Figure 2.14 (black), along with the root-locus obtained from the parametric model (2.13) (grey). The grey ‘ $\times$ ’ and ‘ $\circ$ ’ markers indicate the open-loop poles and zeros of  $H(s)C(s)$  obtained from the system model and controller.

Each point on the root-locus is a possible closed-loop pole location that is achieved when the gain  $k$  of the controller is set to the corresponding value. Stated the other way around, when the gain of the controller is increased from zero to infinity, the poles will travel from the open-loop pole locations along the plotted lines. It can be observed that the two system poles in the origin go to the zeros of the system for increasing gains. The two poles at 380 rad/s travel to the real axis where one goes towards infinity, while the other goes to the zero of the lead filter at  $-125$ .

The root-locus will be investigated in more detail for three choices of  $k$ . For  $k = 4.29$ , the closed-loop poles lie at the points marked with ‘a’, for  $k = 8.58$  they are at ‘b’ and for  $k = 17.16$  the closed-loop poles lie at locations marked with a ‘c’. The closed-loop poles from the model are marked with a grey ‘+’. The closed-loop poles computed using the TFD-based approach are plotted with a black ‘+’, where the size of the marker indicates the uncertainty of the pole location. The uncertainty on the pole location is computed from the uncertainty of  $\hat{H}(s_i)$  by computing the pole location for 100 random realizations  $\hat{H}_r(s_i)$  that lie within the error bound  $E(s_i)$ . Thus

$$\hat{H}_r(s_i) = \hat{H}(s_i) + re^{i\phi}|\Delta\hat{H}(s_i)|, \quad (2.55)$$

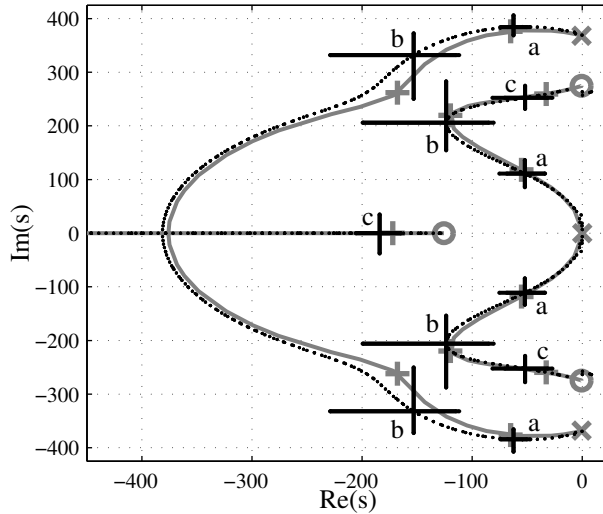


Figure 2.14: Data-based root-locus computed from TFD (black). Model-based root-locus (grey). Corresponding poles indicated with '+' at root-locus gains are a:  $k=4.29$ , b:  $k=8.58$  and c:  $k=17.16$ . The size of the black '+' indicates the uncertainty of the TFD poles.

where  $0 < r < 1$  and  $0 \leq \phi < 2\pi$ . It can be observed that the closed-loop poles obtained from the model lie within the uncertainty bounds of the poles computed from TFD.

It can be observed that the poles that start at the origin lie the farthest in the LHP at 'b'. At 'b', where the controller gain  $k = 8.58$ , the real part of these poles is equal to  $-124$ . For  $k = 8.58$ , the closed-loop poles that start the root-locus at  $380$  rad/s, are shifted even farther into the LHP. This means that 'b' is an optimal choice for the controller gain in terms of decay rate of the oscillations. Choosing the controller gain half as high results in closed-loop poles that lie at 'a', which are closer to the imaginary axis and which will therefore have a larger time-constant. Similarly, doubling the controller gain results in closed-loop poles that lie at 'c' which also have a larger time-constant. The open-loop bode diagram is plotted for these three choices for the gain, see Figure 2.15. In the figure it can be observed that the lead filter increases the phase in the cross-over regions of the three controllers. This shows that all three systems are stable. In manual loop-shaping, the open-loop plot is conventionally used to tune the controller. It can be observed that the cross-over frequency increases as the gain increases. However, no conclusions can be drawn from this plot about how this affects the damping

of the system. It will become clear that the data-based root-locus computed with TFD does provide this information.

The predicted closed-loop poles from the model and from TFD are given in Table 2.1 for the three choices of the gain. Since the TFD is only computed in the range of interest, which lies around the resonant poles of the system, not all closed-loop poles are obtained from the data-based root-locus. There are poles in the controller that give closed-loop poles at high frequencies or at locations far in the left half-plane, which are not obtained from the TFD. However, for the analysis of the time-constant of the system poles, these poles are irrelevant. The model, of course, gives all the closed-loop poles, which explains why Table 2.1 contains more poles in the column of the model-based approach. The uncertainty of the TFD poles, as indicated by the size of the black '+' markers in Figure 2.14, is also given in the table. The closed-loop poles computed from the model lie within the uncertainty of the closed-loop poles computed from TFD.

Point	Gain	Closed-loop poles (model)	Closed-loop poles (TFD)
a	4.29	-2266	
		$-55 \pm 119j$	$-52^{+18}_{-23} \pm 111^{+25}_{-26}j$
		$-65 \pm 377j$	$-62^{+15}_{-12} \pm 384^{+23}_{-19}j$
		$-1324 \pm 4122j$	
b	8.58	-1920	
		$-120 \pm 220j$	$-124^{+43}_{-76} \pm 206^{+82}_{-52}j$
		$-168 \pm 264j$	$-153^{+42}_{-76} \pm 332^{+40}_{-82}j$
		$-1329 \pm 4046j$	
c	17.16	-172	$-184^{+20}_{-22} \pm 0^{+35}_{-38}j$
		$-33 \pm 258j$	$-52^{+25}_{-30} \pm 252^{+25}_{-24}j$
		$-1113 \pm 949j$	
		$-1345 \pm 3864j$	

Table 2.1: Predicted closed-loop pole locations from TFD and from the model for three choices of the controller gain.

## Step 4: Time-domain performance

Since both TFD and the model can only give an *estimation* of the actual closed-loop pole locations, time-domain measurements have been conducted for the three choices of the gain of the controller. A third order trajectory is designed to drive

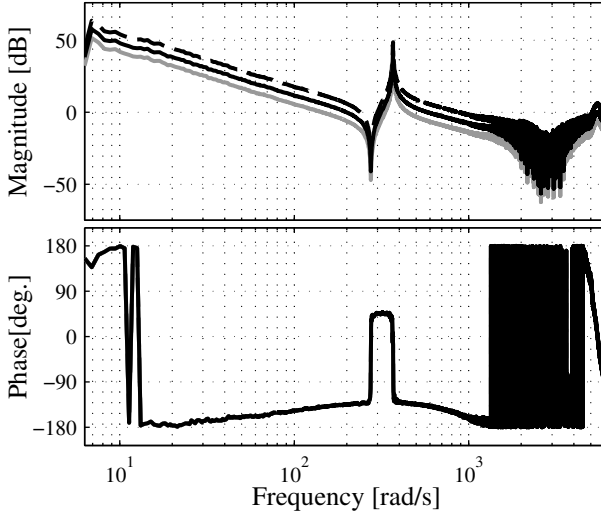


Figure 2.15: Open-loop Bode diagram for three values for the controller gain;  $k=4.29$  (grey),  $k=8.58$  (black) and  $k=17.16$  (dashed).

the system to one full revolution in 0.06 seconds. The responses for the three chosen gains are shown in Figure 2.16. As predicted with the root-locus, the black line, corresponding to  $k = 8.58$  associates with the fastest settling time.

Figure 2.17 shows the power spectral density function of the response for  $t > 0.06$ . The spectrum for the first 0.06 seconds is omitted because it is dominated by the frequency contents of the reference. From 0.06 seconds, the reference is constant, such that the response shows the settling dynamics of the closed-loop. It can be observed that the response for the low-gain case (in grey) has peaks at 119 and 386 rad/s. From Table 2.1 it can be observed that these values are close to the frequencies that were predicted by the root-locus (119 and 383 rad/s). The peak is the highest at 119 rad/s, since that pole is the least damped one of the two. For the ideal gain (black), the dominant frequency is 201 rad/s, where the root-locus predicted 195 rad/s. The root-locus also predicted a pole at 295 rad/s, but that pole is much more damped, such that it is not visible in the spectrum of the response. For the high-gain case (dashed), the dominant frequency is 254 rad/s, which also corresponds to the root-locus (251 rad/s). The closed-loop poles predicted at the real axis are also too damped and cannot be observed in the figure.

While the *frequency* of the closed-loop poles is easily obtained from the power spectrum, the *damping value* of the closed-loop poles cannot be easily obtained

from the time-domain response. In some cases, the damping of a closed-loop pole can be estimated by fitting an exponential function on the peaks of a response. This method works well for closed-loop responses that are not very damped, since in that case many oscillations of the response can be used in the fit. In the case at hand, this method would be inaccurate since all three responses are fast, which makes the fit very inaccurate. Nevertheless, from the figure it is clear that the black line is associated with the fastest settling time, which indicates that the closed-loop poles lie the farthest in the LHP.

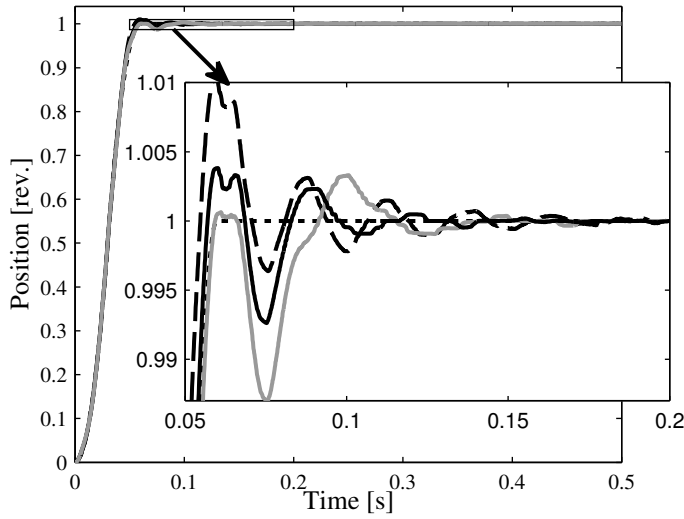


Figure 2.16: Measured response on reference trajectory (dotted) for  $k=4.29$  (grey),  $k=8.58$  (black) and  $k=17.16$  (dashed).

## 2.7 Conclusions

Transfer function data (TFD) can be interpreted as a data-based version of the transfer function of a system. It bridges the gap between model-based and data-based approaches by enabling the application of model-based controller synthesis and analysis tools in a data-based way.

TFD can be computed for lightly damped, stable, strictly proper systems by computing a Cauchy integral over its frequency response data (FRD). TFD gives the



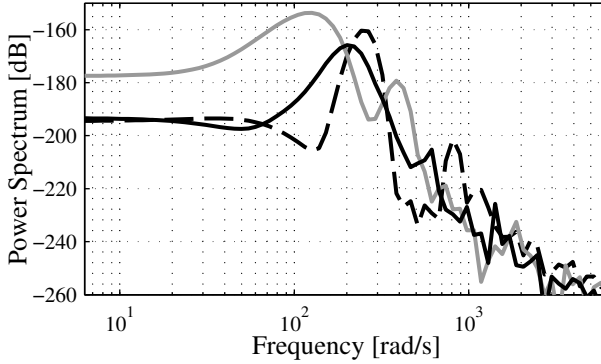


Figure 2.17: Power spectrum of the measured response for  $t > 0.06$  of  $k=4.29$  (grey),  $k=8.58$  (black) and  $k=17.16$  (dashed).

value of the transfer function for a grid of points in the complex plane. For an accurate computation the FRD that is used to compute the TFD must be measured with high resolution. Furthermore the highest frequency of the FRD must be well above the highest frequency at which the TFD is computed. Since the Cauchy integral can only be used to compute RHP TFD, the damping of the system under consideration must be low enough such that the TFD is approximately symmetric in the imaginary axis. This enables the computation of TFD for the whole complex plane by mirroring the RHP TFD to the LHP. The method attenuates measurement noise that is present in the FRD, especially for TFD computed at points in the complex plane that lie far from the imaginary axis. This is caused by the noise filtering properties of the Cauchy integral. The computation time of TFD at one point in the complex plane is in the order of milliseconds, such that it is feasible to compute a grid of points in the complex plane in a few seconds on a normal pc.

As a use-case a data-based root-locus is computed for a bench-mark motion system using TFD. It was found that the controller gain and corresponding closed-loop pole frequencies can be computed accurately. It is shown that it is possible to optimize the gain such that the time-constant of the closed-loop poles is minimal. This was achieved by selecting the controller gain for which the closed-loop pole locations lie the farthest in the LHP.

In the next chapter, the method will be extended to multi-input multi-output systems. For multi-input multi-output systems the approach is even more fruitful, since the modelling of these systems is more difficult such that this approach can be an attractive alternative to parametric modelling of the system.

## Chapter 3

# Data-based computation of closed-loop poles for MIMO systems

**T**his chapter describes the use of TFD in the computation of closed-loop poles of lightly damped MIMO systems. MIMO TFD enables data-based evaluation of the determinant of the return difference matrix. It is explained that this enables the computation of closed-loop poles from TFD including their multiplicity. Experiments on a proto-type wafer stage are presented to demonstrate the practical applicability of the proposed approach. Moreover, a loop-shaping design example is included where the damping of a number of flexible modes is improved by incorporating the obtained closed-loop poles in the control design.

### 3.1 Introduction

The trend that the number of transistors on a chip increases while the cost of a chip decreases leads to increasing performance requirements for wafer scanners in the chip manufacturing industry. To satisfy the specifications on throughput and resolution, increased speed and accuracy of the motion systems in these machines is required. Next generation positioning systems are often designed to be lightweight to enable high accelerations at limited actuator forces, which improves throughput. At the same time lightweight systems are typically less stiff causing flexible

dynamics to shift to lower frequencies, which can lead to a decrease in machine performance. Typical performance measures for these machines are overlay and imaging performance (Wagner et al., 2011). It is expected that the semiconductor industry will switch from the current 300 mm to 450 mm substrates as to increase throughput (Pettinato and Pillai, 2005). For larger substrates, flexible dynamics of the motion stages will become even more pronounced.

Conventionally, high-precision motion systems are designed to exhibit rigid-body dynamics for frequencies below the desired bandwidths of the system. The systems are equipped with multiple actuators and sensors, making them multi-input-multi-output (MIMO) systems. Geometric decoupling is used to decouple these inputs and outputs such that all six rigid-body degrees-of-freedom can be controlled independently (Butler, 2011). Manual loop-shaping based on measured frequency response data is used in industry to tune the controllers. The flexible dynamics of these systems tend to have low damping due to the undamped materials used to construct these systems, such as ceramics and metals. As a result, the systems will exhibit lightly damped resonances beyond the target bandwidths due to the flexible modes of the system. In case these flexibilities limit the performance or endanger closed-loop stability, these resonances need to be suppressed in the control design, which is generally done by using notch filters.

By increasing bandwidth specifications or due to the decrease in stiffness of the mechanical structure of these systems, the resonance frequencies will shift towards (or even drop below) the target bandwidths. Conventional notch filters only prevent excitation of the flexible dynamics by the control system. This is done by decreasing the loop-gain at the resonance frequencies. However, this also prevents the control system to control the flexible modes in case they are excited by external disturbances. Due to the low damping of these flexible modes, this often induces too long settling times, which limits performance. This illustrates that active control of the flexible modes is key to high-precision motion control.

One solution is to use more actuators and sensors to increase control authority over the flexible modes. This is sometimes referred to as *over-sensing* and *over-actuation* (Schneiders et al., 2004). Using more actuators and sensors than needed for rigid-body control enables modal decoupling (Inman, 1984) where besides the rigid-body modes a number of flexible modes can be decoupled. In this way, each decoupled mode can be addressed by the control system in a separate control loop. However, as high-precision motion systems typically have a large number of relevant modes, it is infeasible to decouple all these flexible modes as this would require a large number of actuators and sensors.

It is evident that the control system should add damping to the flexible modes to improve performance. However, classical loop-shaping design using measured

FRD cannot incorporate damping of closed-loop poles as one of the design criteria. The reason for this is that the closed-loop poles cannot be computed from the data directly. To do so, a parametric model of the system to be controlled is required. Unfortunately, deriving an accurate low-order parametric model for control design is no easy task for the considered class of systems. Compared to first principles modelling techniques or finite element modelling, the non-parametric FRD can be measured at low cost with high accuracy. Therefore, the a more feasible approach is to fit a parametric transfer function on the measured FRD. This, however is hampered by the choice of the model-order for such a fit. In van de Wal et al. (2002) it is described how a MIMO model can be obtained from FRD by combining single-input single-output (SISO) fits for each of the input-output combinations. It is shown that redundant state variables may remain in the MIMO model despite the use of model reduction techniques. The controllers synthesised with these models can be unstable and are typically of too high order, which still is considered an open problem (Oomen and Bosgra, 2012).

An alternative approach would be to pursue a data-based control design. Active vibration control methods using FRD are proposed in Preumont and Seto (2008). However, the analysis tools for such methods are very limited if no model of the system is available. For example, there is no way to precisely determine how much damping will be added by feedback control. The same limitation is encountered in other recent advances in FRD-based control. For example, optimization-based computation of QFT controllers is described in Molins and Garcia-Sanz (2009) and Halikias et al. (2007). Another recent contribution by Keel and Bhattacharyya (2008) shows the computation of the set of all stabilizing PID controllers that satisfies a certain performance criterion, specified by the phase or gain margin or by the  $\mathcal{H}_\infty$  norm. FRD based fixed-order  $\mathcal{H}_\infty$  control design is described in Karimi et al. (2007); Karimi and Galdos (2010). Performance specifications for these methods are given in the frequency-domain, which is well-suited to guarantee stability and disturbance rejection properties. However, it is not clear at all how to specify damping of the resonant poles.

Besides these frequency-domain methods, time-domain data-based methods, such as data-based LQG (Skelton and Shi, 1994), Virtual Reference Feedback Tuning (Campi et al., 2000), (Formentin et al., 2012) or Iterative Feedback Tuning (Hjalmarsson and Gevers, 1998) have been developed. Although these methods can be used to specify the damping of the closed-loop poles indirectly by posing constraints on the time-domain response, they do not easily combine with the well established frequency-domain design methods that are currently used for high-precision motion systems. A different approach is therefore required.

The approach pursued in this chapter is to compute the closed-loop poles of a MIMO system from *transfer function data* (TFD). TFD can be regarded as a

data-based or sampled version of the transfer function. Where FRD only gives information on the response of the system on the imaginary axis, TFD gives information on the response of the system in the complex plane. TFD can be computed from FRD, which is shown in the previous work (Hoogendijk et al., 2010) and in the previous chapter. Key in the computation is the usage of a Cauchy contour integral. The Cauchy contour integral is a concept from complex function theory (see, e.g., (Rahman, 1997)) that is often used in control theory. The well-known Bode sensitivity integral (Bode, 1945) and Hilbert transform (Teschke, 1992) are two examples of its application. More recently, it was shown that stability and causality of systems can be proven using Cauchy integrals (Den Hamer et al., 2008).

Different from Hoogendijk et al. (2010) and the previous chapter, this chapter considers the computation of TFD and its uncertainty bounds for MIMO systems. For a given controller, the closed-loop poles of the MIMO system can be computed in a completely data-based way, without the need for a parametric model of the system to be controlled. The computation of the closed-loop poles is done via data-based computation of the determinant of the return difference matrix. In the 80's, this determinant attracted a lot of attention in attempts to generalize classical SISO control theory to MIMO systems. For example, see the MIMO variants of the Nyquist criterion, root-locus and pole-placement given in Brockett and Byrnes (1981); Mayne (1973); Postlethwaite and MacFarlane (1979); Owens (1978), which are all based on parametric models. With the shift towards  $\mathcal{H}_\infty$  control design (Maciejowski, 1989), most of the earlier techniques lost attention.

MIMO TFD allows for evaluation of the determinant of the return difference matrix in the complex plane without the need for a parametric model. Thus, the (complex) value of the determinant can be computed for all points in the complex plane. To analyse the TFD, techniques are used that are closely related to the classical SISO root-locus techniques (Evans, 1950). In Ash and Ash (1968) it is described that the imaginary part of the open-loop is zero along the root-locus. Comparable properties are derived in this chapter for the determinant of the return difference matrix. So-called  $u$ - and  $v$ -contours will be computed; contours where either the real part or the imaginary part of the determinant equals zero. Intersections of these contours not only reveal the closed-loop pole locations, but also the open-loop pole locations. Moreover, the multiplicity of the poles can be derived from these contours. It must be emphasized that these contours are computed directly from the TFD, thus no parametric model is needed.

The main contributions of this chapter can be summarized as follows:

- a method to compute TFD and its uncertainty bounds for MIMO systems,
- numerically reliable computation of the closed-loop poles of MIMO systems

from TFD,

- validation of the closed-loop poles by experiments on a prototype wafer stage,
- controller design example for a prototype wafer stage.

The chapter is organized as follows. First, the computation of TFD from FRD is described in Section 3.2. The section explains the underlying assumptions and approximations of the computation. Next, the estimation errors of the computation are treated in Section 3.3. Section 3.4 explains how the computed TFD can be used to compute the closed-loop poles for a given controller. The proposed methods are validated on a prototype wafer stage that exhibits dominant flexible dynamics, which is the topic of Section 3.5. The computed closed-loop poles are validated by making a comparison with time-domain responses of the closed-loop system. Furthermore, a design example is included where a controller is tuned using TFD. Experimental validation shows improved damping characteristics for the targeted flexible modes.

## 3.2 Computation of TFD

This section describes the computation of transfer function data (TFD) for MIMO systems and can be seen as an extension of the computation of TFD for SISO systems as described in the previous chapter.

### 3.2.1 Definition of TFD

Let a MIMO system  $\mathbf{H}(s)$  consist of the entries  $H_{yu}(s)$ , where  $y = 1, 2, \dots, n_y$  are the  $n_y$  outputs and  $u = 1, 2, \dots, n_u$  are the  $n_u$  inputs, or

$$\mathbf{H}(s) = \begin{bmatrix} H_{11}(s) & H_{12}(s) & \dots & H_{1n_u}(s) \\ H_{21}(s) & H_{22}(s) & \dots & H_{2n_u}(s) \\ \vdots & \vdots & \ddots & \vdots \\ H_{n_y1}(s) & H_{n_y2}(s) & \dots & H_{n_y n_u}(s) \end{bmatrix}. \quad (3.1)$$

An accurate, low-order parametric model of  $\mathbf{H}(s)$  is generally not available for high-precision motion systems. Therefore, controllers for this class of systems are typically designed using loop-shaping based on frequency response data (FRD). FRD is defined to be a set of samples  $\mathbf{H}(j\omega_k)$  of a transfer function  $\mathbf{H}(s)$  at the

points  $s = j\omega_k$ ,  $\omega \in \mathbb{R}$ , or

$$\mathbf{H}(j\omega_k) = \begin{bmatrix} H_{11}(j\omega_k) & H_{12}(j\omega_k) & \dots & H_{1n_u}(j\omega_k) \\ H_{21}(j\omega_k) & H_{22}(j\omega_k) & \dots & H_{2n_u}(j\omega_k) \\ \vdots & \vdots & \ddots & \vdots \\ H_{n_y1}(j\omega_k) & H_{n_y2}(j\omega_k) & \dots & H_{n_y n_u}(j\omega_k) \end{bmatrix}. \quad (3.2)$$

The subscript  $k = 1, 2, \dots, N$  is an index in the set of  $N$  data points, which can be obtained via available frequency response identification techniques (Pintelon and Schoukens, 2001). FRD gives only partial information about  $\mathbf{H}(s)$ , since the transfer function is only evaluated at points  $s = j\omega_k$  that lie on the imaginary axis of the  $s$ -plane. Therefore, the concept *transfer function data* (TFD) is introduced. TFD contains the response  $\mathbf{H}(s_i)$  at complex frequencies  $s_i = \sigma_i + j\omega_i$ , where the subscript  $i = 1, 2, \dots, N_{tfd}$  is an index in the set of  $N_{tfd}$  data points, or

$$\mathbf{H}(s_i) = \begin{bmatrix} H_{11}(s_i) & H_{12}(s_i) & \dots & H_{1n_u}(s_i) \\ H_{21}(s_i) & H_{22}(s_i) & \dots & H_{2n_u}(s_i) \\ \vdots & \vdots & \ddots & \vdots \\ H_{n_y1}(s_i) & H_{n_y2}(s_i) & \dots & H_{n_y n_u}(s_i) \end{bmatrix}. \quad (3.3)$$

In  $s_i$ ,  $\sigma_i \in \mathbb{R}$  represents the real part of  $s_i$  whereas  $\omega_i \in \mathbb{R}$  represents the imaginary part or frequency of  $s_i$ . The former can be regarded as the absolute damping or time constant. In this way, TFD provides information about the system for a grid of points  $s_i$  in the complex plane and not only for the imaginary axis. As a result, TFD  $\mathbf{H}(s_i)$  can be regarded as the data-based representation of the transfer function  $\mathbf{H}(s)$  of the system.

### 3.2.2 Computation of TFD in the RHP

The concept of TFD is straightforward. It is a sampled version of the transfer function. However the concept will only be useful if TFD can be obtained from measured FRD, without the use of a parametric model. In this section, it will be explained that in the right half-plane (RHP) TFD can be computed from FRD using a Cauchy integral. The Cauchy integral formula (Rahman, 1997) states the following.

**Theorem 3.1** (*Cauchy integral formula*) *Let  $g(s)$  be an analytic function in a region  $G$ ,  $\mathcal{C}$  a simple closed curve in  $G$  in anticlockwise direction and let  $s_i$  denote a point in  $\mathcal{C}$ . Then*

$$g(s_i) = \frac{1}{2\pi j} \int_{\mathcal{C}} \frac{g(s)}{s - s_i} ds. \quad (3.4)$$

*Proof:* For the proof, see Rahman (1997). ■

Transfer functions are complex functions that are analytic, except at the pole locations. Therefore, Theorem 3.1 implies that the value  $\mathbf{H}(s_i)$  of a transfer function at the point  $s_i$  can be computed if the transfer function is analytic in the contour surrounding  $s_i$  and if the value of the transfer function is known on this contour. For stable systems, the RHP is an analytic region. Because the value of the transfer function on the imaginary axis, i.e., the FRD, can be obtained by frequency domain identification techniques, a good choice for the contour is a D-contour  $\mathcal{C}_D$  as shown in Figure 3.1.  $\mathcal{C}_D$  consists of the imaginary axis plus a semicircle at infinity to close the contour.

Since each entry  $H_{yu}(s)$  of the MIMO transfer function  $\mathbf{H}(s)$  in (3.1) is a complex function itself, the computation of MIMO TFD can be performed for each SISO TFD entry of the transfer function matrix separately. The TFD in a particular entry can be computed from the FRD of the corresponding entry. That is, the results from the previous chapter can be used to compute TFD for each entry  $H_{yu}(s)$  of the MIMO system. Applying (3.4) to this contour gives

$$H_{yu}(s_i) = \frac{1}{2\pi j} \int_{\mathcal{C}_D} \frac{H_{yu}(s_{\mathcal{C}_D})}{(s_{\mathcal{C}_D} - s_i)} ds_{\mathcal{C}_D}, \quad s_i \in \mathbb{C}^+, \quad (3.5)$$

where  $s_{\mathcal{C}_D}$  denotes the points that lie on  $\mathcal{C}_D$ . The element-wise integration of all elements is denoted by

$$\mathbf{H}(s_i) = \frac{1}{2\pi j} \int_{\mathcal{C}_D} \frac{\mathbf{H}(s_{\mathcal{C}_D})}{(s_{\mathcal{C}_D} - s_i)} ds_{\mathcal{C}_D}, \quad s_i \in \mathbb{C}^+. \quad (3.6)$$

Furthermore, for strictly proper systems like the electromechanical motion systems considered in this work it holds that

$$\lim_{s \rightarrow \infty} \mathbf{H}(s) = \mathbf{0}, \quad (3.7)$$

which means that the value of the transfer function on the semicircle at infinity is zero. This reduces (3.6) to

$$\mathbf{H}(s_i) = \frac{1}{2\pi} \int_{-\infty}^{\infty} \frac{\mathbf{H}(j\omega)}{(s_i - j\omega)} d\omega, \quad s_i \in \mathbb{C}^+. \quad (3.8)$$

Note that the integration bounds are interchanged. This gives a minus sign that is accounted for in the denominator of the integrand. Furthermore, a factor  $j$  is taken outside of the integral to make the integration variable real-valued.

In practice, the integral (3.8) cannot be computed, since the frequency response can only be measured up till a certain maximum frequency  $\omega_{max}$ , i.e.,

$$\mathbf{H}(s_i) = \frac{1}{2\pi} \int_{-\omega_{max}}^{\omega_{max}} \frac{\mathbf{H}(j\omega)}{(s_i - j\omega)} d\omega + \mathbf{E}_f(s_i), \quad s_i \in \mathbb{C}^+, \quad (3.9)$$



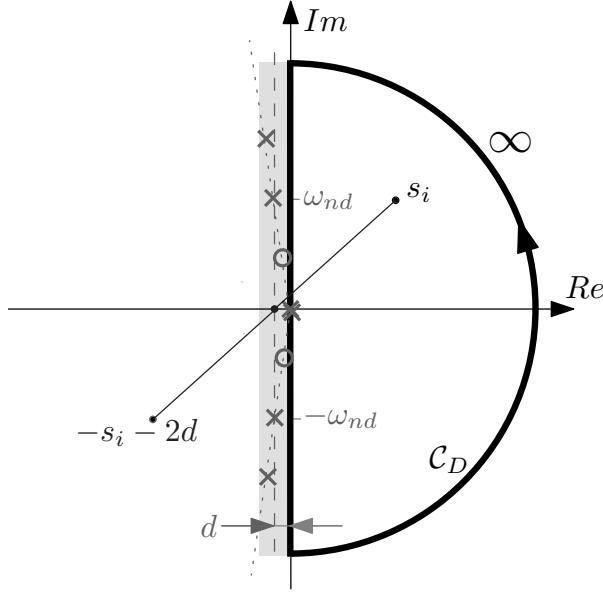


Figure 3.1: Contour  $C_D$  in the  $s$ -plane used to compute TFD at the point  $s_i$ . Symmetry of the poles  $\times$  and zeros  $\circ$  is used to estimate the TFD at the point  $-s_i - 2d$ .

where  $\mathbf{E}_f(s_i)$  is the error that is made due to computing a definite integral. Further analysis and estimation of the error terms of the TFD will be considered in Section 3.3.

As the measured FRD, denoted by  $\hat{\mathbf{H}}(j\omega_k)$ , is only available at discrete points  $\omega_k$ , it is necessary to approximate (3.9) numerically. By using for example the trapezium method, an estimate  $\hat{\mathbf{H}}(s_i)$  is obtained that yields

$$\hat{\mathbf{H}}(s_i) = \frac{1}{4\pi} \sum_{k=-N}^{N-1} \left( \frac{\hat{\mathbf{H}}(j\omega_k)}{(s_i - j\omega_k)} + \frac{\hat{\mathbf{H}}(j\omega_{k+1})}{(s_i - j\omega_{k+1})} \right) \Delta\omega, \quad (3.10)$$

where  $\Delta\omega = \omega_{k+1} - \omega_k$ . The index  $k$  runs from  $-N$  to incorporate negative FRD, which is required as the integral runs over the negative frequencies as well. The response at negative frequencies is easily obtained as it holds that

$$\mathbf{H}(-jw) = \mathbf{H}^*(jw), \quad (3.11)$$

where  $*$  denotes the complex conjugate. The estimation  $\hat{\mathbf{H}}(s_i)$  can be related to the actual value  $\mathbf{H}(s_i)$  by

$$\mathbf{H}(s_i) = \hat{\mathbf{H}}(s_i) + \mathbf{E}_n(s_i) + \mathbf{E}_i(s_i) + \mathbf{E}_f(s_i). \quad (3.12)$$

Here the already mentioned error  $\mathbf{E}_f(s_i)$  due to the definite integral appears, as well as two additional error terms. The FRD itself will contain noise, which leads to the error  $\mathbf{E}_n(s_i)$ . Furthermore, the integration method gives an error  $\mathbf{E}_i(s_i)$ . For example, the trapezium method used in (3.10) is only exact if the second-order derivative of the FRD with respect to the frequency is zero.

Note that it is sufficient to compute TFD for the upper quadrant of the RHP as for the lower quadrant of the RHP it holds true that

$$\mathbf{H}(s^*) = \mathbf{H}^*(s), \quad (3.13)$$

i.e., TFD for the lower quadrant of the RHP is obtained by taking the complex conjugate.

### 3.2.3 TFD for systems with integrators

Many mechanical systems contain double integrators, i.e., a set of poles that lies in the origin of the  $s$ -plane. For systems with undamped poles, (3.10) cannot be used directly to compute  $\hat{\mathbf{H}}(s_i)$  from  $\hat{\mathbf{H}}(j\omega_k)$  because the contour does not lie in an analytic region due to the poles on the imaginary axis. Numerically, the computation is hampered by the fact that the FRD will have a very high second-order derivative at the pole location, which induces large errors by numerical integration.

As explained in Chapter 2 for SISO systems a straightforward way to deal with this problem is to add a known weighting filter  $\mathbf{W}(s)$  to the FRD in the computation step. This method can be generalized for MIMO systems as follows. Let  $\mathbf{W}(s)$  be a high-pass filter of which the entries  $W_{yu}(s)$  are given by

$$W_{yu}(s) = \frac{s^2}{s^2 + 2\beta_W 2\pi f_W s + \omega_W^2}. \quad (3.14)$$

This filter exactly cancels the integrators of the plant by the  $s^2$  term in the numerator. The denominator ensures that the influence of the filter is limited to the low-frequency range to prevent amplification of noise at high frequencies, and to ensure that the filtered system is strictly proper. As the specific values of the damping  $\beta_W$  and corner frequency  $f_W$  of  $\mathbf{W}(s)$  do not influence the removal of

the pure integrators, this freedom is utilized to reduce the amplitude of the filtered FRD at low frequencies, where the FRD is often less accurate due to the limited measurement time used to obtain the data. However,  $f_W$  should be chosen smaller than the lowest resonance of the system as to minimize the influence of this method on the computed result of the TFD in the relevant frequency range.

The FRD  $\hat{\mathbf{H}}(j\omega_k)$  is multiplied with the FRD of the filter  $\mathbf{W}(j\omega_k)$  thereby cancelling the undamped poles giving the filtered FRD  $\hat{\mathbf{H}}_f(j\omega_k)$ , or

$$\hat{\mathbf{H}}_f(j\omega_k) = \hat{\mathbf{H}}(j\omega_k) \odot \mathbf{W}(j\omega_k), \quad (3.15)$$

where  $\odot$  denotes element-wise multiplication. Using (3.10), TFD  $\hat{\mathbf{H}}_f(s_i)$  is computed from the filtered FRD  $\hat{\mathbf{H}}_f(j\omega_k)$ . Since the filter  $\mathbf{W}(s_i)$  is known for all points  $s_i$ , it can be removed from  $\hat{\mathbf{H}}_f(s_i)$  giving

$$\hat{\mathbf{H}}(s_i) = \hat{\mathbf{H}}_f(s_i) \oslash \mathbf{W}(s_i), \quad (3.16)$$

where  $\oslash$  denotes element-wise division. It is required that  $\mathbf{W}(s_i)$  does not have any right half-plane zeros in its entries, as this would make the division in (3.16) indeterminate at the zero locations.

### 3.2.4 Computation of TFD in the LHP

So far, computation of TFD in the RHP using a Cauchy integral method has been discussed. However, the Cauchy integral method cannot be used to compute TFD in the left half-plane (LHP). The LHP contains the poles of the system, which renders it a non-analytic region of the transfer function. However, lightly damped resonant systems, for which this method is primarily developed, have poles and zeros that lie close to the imaginary axis, see Figure 3.1. This gives the TFD a certain symmetry that can be exploited in computing TFD in the LHP.

The specific symmetry condition that can be used depends on the system at hand. For systems with force actuators and position sensors, as is usually the case for motion systems, the transfer function can be written as a summation of  $N_m$  modes  $n$  with modal participation matrix  $\Psi_n$ , frequency  $\omega_n$  and damping  $\zeta_n$  as in

$$\mathbf{H}(s) = \sum_{n=1}^{N_m} \frac{\Psi_n}{s^2 + 2\zeta_n\omega_n s + \omega_n^2}. \quad (3.17)$$

For undamped systems, i.e.,  $\zeta_n = 0$ , it can be concluded from (3.17) that

$$\mathbf{H}(-s_i) = \mathbf{H}(s_i). \quad (3.18)$$

Thus the TFD of undamped systems is symmetric with respect to the origin of the complex plane. However, this may give a too rough approximation for real systems where the poles and zeros of the modal system do have a certain amount of damping  $\zeta_n > 0$ .

It is therefore desirable to have a more accurate symmetry condition than (3.18), which is the MIMO equivalent to the symmetry condition in 2.9. As the goal of the method is to analyse closed-loop pole locations, it makes sense to focus on specific modes in the analysis. Around the resonance frequency  $\omega_n$  of mode  $n$  the transfer function is dominated by the complex pole pair of this mode, i.e., around  $\omega_n$  it holds that

$$\begin{aligned} \mathbf{H}(s) &\approx \frac{\Psi_n}{s^2 + 2\zeta_n\omega_n s + \omega_n^2} \\ &\approx \frac{\Psi_n}{(s - j\omega_{nd} + \sigma_n)(s + j\omega_{nd} + \sigma_n)}, \end{aligned} \quad (3.19)$$

where  $\omega_{nd} = \omega_n \sqrt{1 - \zeta_n^2}$  denotes the imaginary part of the pole pair, which is the damped eigenfrequency of mode  $n$ .  $\sigma_n = -\zeta_n|\omega_n|$  denotes the real part of the pole pair. From (3.19) it is derived that

$$\begin{aligned} \mathbf{H}(-s_i - 2\sigma_n) &\approx \frac{\Psi_n}{(-s_i - 2\sigma_n - j\omega_{nd} + \sigma_n)(-s_i - 2d + j\omega_{nd} + \sigma_n)} \\ &\approx \frac{\Psi_n}{(-s_i - j\omega_{nd} - \sigma_n)(-s_i + j\omega_{nd} - \sigma_n)} \\ &\approx \frac{\Psi_n}{(s_i + j\omega_{nd} + \sigma_n)(s_i - j\omega_{nd} + \sigma_n)} \\ &\approx \mathbf{H}(s_i). \end{aligned} \quad (3.20)$$

Thus, around the pole of interest the TFD is approximately symmetric in the point  $s = -\sigma_n$ . Denoting the distance of this point to the imaginary axis by  $d := |\sigma_n|$ , this results in the symmetry condition

$$\mathbf{H}(-s_i - 2d) = \mathbf{H}(s_i) + \mathbf{E}_m(s_i), \quad (3.21)$$

where  $\mathbf{E}_m(s_i)$  is the error term of the TFD in the LHP introduced by the symmetry approximation. This adds an additional error term to (3.12). The symmetry condition is depicted in Figure 3.1, where the poles at  $\pm\omega_{nd}$  are the poles of interest. As the RHP TFD is mirrored in the point  $s = -d$ , there will be a region where no TFD is computed. This region

$$-2d \leq \text{Re}(s) \leq 0, \quad (3.22)$$

is indicated in the figure as the grey zone left to the imaginary axis. This zone is typically small for lightly damped systems.

Using the symmetry condition in (3.21) gives more accurate LHP TFD around the mode of interest, as the TFD is also dominated by the contribution of this pole. This can be observed from the denominator  $(s_i - j\omega)$  of the integrand in (3.9). This denominator weights the contribution of the FRD  $H_{yu}(j\omega)$  with the inverse of the distance of  $s_i$  to  $j\omega$ . As the FRD around the pole of interest is dominated by the pole of mode  $n$ , and the FRD of the other modes is weighted less due to the weighting with the inverse of  $(s_i - j\omega)$ , the TFD around the pole of mode  $n$  is dominated by this pole.

Estimating the absolute damping  $\sigma_n$  of the pole of mode  $n$  to determine  $d$  is a straightforward operation that does not require a parametric model of the system. An estimate of the damped eigenfrequency  $\hat{\omega}_{nd}$  can easily be obtained by taking the frequency of the resonance peak in the FRD. For lightly damped mechanical systems it is fairly common to use a damping ratio between  $\zeta \approx 0.001 - 0.005$  (Preumont, 2011). Using an estimate  $\hat{\zeta}$  from this range, it follows that

$$\sigma_n \approx \hat{\zeta} \hat{\omega}_{nd}. \quad (3.23)$$

Summarizing, TFD can be computed in the entire complex plane as follows. Compute TFD in the upper quadrant of the RHP using (3.10). Then, the lower quadrant of the RHP is obtained using (3.13), where the LHP TFD is obtained using the symmetry condition in (3.21).

### 3.3 Uncertainty estimation

In the computation of TFD, four error terms have been identified, see (3.12) and (3.21). In practice, the value of these error terms cannot be computed, as the true  $\mathbf{H}(s)$  is unknown. However, in order to compute error bounds on the closed-loop poles that will be computed using TFD, it is useful to estimate error bounds on the TFD. Therefore, error bounds on these terms will be given. In Sections 3.3.1 to 3.3.4 error bounds for the individual error terms are presented. The total error bound is discussed in Section 3.3.5.

### 3.3.1 Error bounds due to a finite integral

The error term  $\mathbf{E}_f(s_i)$  in (3.9) is equal to

$$\begin{aligned} \mathbf{E}_f(s_i) = & \frac{1}{2\pi} \int_{-\infty}^{-\omega_{max}} \frac{\mathbf{H}(j\omega)}{(s_i - j\omega)} d\omega + \\ & \frac{1}{2\pi} \int_{\omega_{max}}^{\infty} \frac{\mathbf{H}(j\omega)}{(s_i - j\omega)} d\omega, \end{aligned} \quad (3.24)$$

which follows from comparison with (3.8). Since  $\mathbf{H}(j\omega)$  is assumed to be strictly proper, the magnitude of  $\mathbf{H}(j\omega)$  has a minus-one slope or steeper at high frequencies. Therefore, the magnitudes of the entries  $H_{yu}(j\omega)$  are bounded by

$$|H_{yu}(j\omega)| \leq \frac{c_{yu}}{|\omega|^n} \quad \text{for } |\omega| > \omega_{max}, \quad n \geq 1, \quad (3.25)$$

assuming that all flexible modes lie below  $\omega_{max}$ . For each entry, a reasonable estimation of the constant  $c_{yu}$  is to take the value of the FRD at  $\omega_{max}$ . Thus, substituting  $\omega_{max}$  in (3.25) gives

$$c_{yu} \geq |H_{yu}(j\omega_{max})| |\omega_{max}^n|. \quad (3.26)$$

This leads to the following error expression

$$\begin{aligned} |E_{f,yu}(s_i)| \leq & \frac{c_{yu}}{2\pi} \left| \int_{-\infty}^{-\omega_{max}} \frac{1}{\omega^n (s_i - j\omega)} d\omega \right| + \\ & \frac{c_{yu}}{2\pi} \left| \int_{\omega_{max}}^{\infty} \frac{1}{\omega^n (s_i - j\omega)} d\omega \right|. \end{aligned} \quad (3.27)$$

$\omega_{max}$  is typically chosen 20-50 times the desired bandwidth and the system will have a minus-one slope or steeper at high frequencies. Consequently,  $H_{yu}(j\omega_{max})$  will typically be small compared to the value of  $H_{yu}(j\omega)$  around the bandwidth of the system. Furthermore, the  $(s_i - j\omega)$  term in the denominator of (3.27) decreases the error even further as typically  $|s_i - j\omega| \gg 1$  for  $\omega > \omega_{max}$ .

### 3.3.2 Error bounds on the integration method

Approximation of the integral (3.9) by the summation (3.10) also gives an error contribution. It is well known that the trapezium method gives an error when it is used to compute the integral of a function that has a non-zero second-order (and possibly higher) derivative. An upper bound of the error can be computed for

each component from the second-order derivative of the integrand (Adams, 1999), giving

$$|\hat{E}_{i,yu}(s_i)| \leq K_{yu}(s_i) \frac{2\omega_{max} \Delta\omega^3}{12}, \quad (3.28)$$

where

$$K_{yu}(s_i) = \max_{\omega} \left| \frac{d^2}{d\omega^2} \frac{H_{yu}(j\omega)}{(s_i - j\omega)} \right|. \quad (3.29)$$

This bound is likely to be very conservative. First, the FRD of lightly damped motion systems will exhibit sharp peaks at the resonances of the system, which causes high second-order derivatives at these frequencies. Fortunately, these peaks only occur at a discrete number of locations in the FRD. Second, at some frequencies the second-order derivative is positive while it is negative at other frequencies. As (3.28) does not take the sign of the second-order derivative into account, it is likely to be a rather conservative error estimation. A more practical approach is to use the average value of the second-order derivative of the integrand, i.e.,

$$M_{yu}(s_i) = \text{mean}_{\omega} \frac{d^2}{d\omega^2} \frac{H_{yu}}{(s_i - j\omega)}, \quad (3.30)$$

to compute the error bound

$$|\hat{E}_{i,yu}(s_i)| \approx |M_{yu}| \frac{2\omega_{max} \Delta\omega^3}{12}. \quad (3.31)$$

Taking the average value causes the positive and negative error contributions to cancel out, which is a more natural approach towards estimating the error bound. However, the disadvantage of this approach is that no guarantee on the size of the error can be given.

Besides, estimating the second-order derivative of  $\mathbf{H}(j\omega)$  itself is not a straightforward task due to the sharp peaks in the FRD, in combination with the noise on the FRD. To cope with the noise, it would be desirable to estimate the second-order derivative using local smooth fits through the given FRD points. However, this causes the resonance peaks to be smoothed as well, thereby underestimating the second-order derivative around the pole locations. A solution that was found to give reasonable estimations of the error in practice is to simply take the numeric second-order derivative of the integrand and using (3.31).

The nature of the data, containing sharp peaks in combination with noise, is also the reason why higher-order numeric integration methods generally become less accurate. As the order of the integration method increases, so do the coefficients that are multiplied with the data points, rendering these methods overly sensitive to noise.

### 3.3.3 Error bounds due to noise

The measured FRD will contain noise contributions, which can be quantified by the variance on the FRD. This variance is given by

$$\text{Var}[\hat{\mathbf{H}}(j\omega)] = \frac{1}{N_p(N_p - 1)} \sum_{k=1}^{N_p} |\hat{\mathbf{H}}(j\omega) - \hat{\mathbf{H}}_k(j\omega)|^2, \quad (3.32)$$

where  $\hat{\mathbf{H}}_k(j\omega)$  is the FRD computed per experiment and  $\hat{\mathbf{H}}(j\omega)$  is the sample mean over  $N_p$  experiments. From (3.32) it is possible to compute the variance of the computed TFD. Using the properties of variance it can be derived from (3.10) that

$$\text{Var}[\hat{\mathbf{H}}(s_i)] = \frac{2}{16\pi^2} \sum_{k=-N}^{N-1} \left( \frac{\text{Var}[\hat{\mathbf{H}}(j\omega_k)]}{|s_i - j\omega_k|^2} + \frac{\text{Var}[\hat{\mathbf{H}}(j\omega_{k+1})]}{|s_i - j\omega_{k+1}|^2} \right) \Delta\omega^2. \quad (3.33)$$

Since the FRD on the negative frequency axis is computed from (3.11),  $\hat{\mathbf{H}}(-j\omega_k)$  and  $\hat{\mathbf{H}}(j\omega_k)$  are correlated, which explains the factor 2 in (3.33).

As it is desired to give error bounds on the computed pole locations, error bounds on the TFD are required. The variance (3.33) is a measure on the extent to which the TFD are distributed. Assuming that  $\hat{\mathbf{H}}(s_i)$  has a circular complex normal distribution, a confidence circle for each element  $E_{n,yu}(s_i)$  can be given. The probability  $P$  that the magnitude of  $E_{n,yu}(s_i)$  is smaller than the radius of this circle is then given by

$$P = \text{Prob}[|E_{n,yu}(s_i)| < r_P \sigma_{H,yu}(s_i)], \quad (3.34)$$

where

$$\sigma_{H,yu}^2(s_i) = \text{Var}[\hat{H}_{yu}(s_i)]. \quad (3.35)$$

$r_P$  can be computed for a given  $P$  according to

$$r_P = \sqrt{-\ln(1 - P)}. \quad (3.36)$$

For example, to ensure the probability that the error lies within this bound is 99%,  $r_P = 2.15$  is chosen. High-precision motion systems are designed to exhibit predominantly linear behaviour and are usually equipped with sensors that have a high signal-to-noise ratio. Furthermore, (3.33) shows that the variance of the FRD is weighted with  $|s_i - j\omega_k|^{-2}$  terms. Hence, the variance on the TFD decreases quadratically as  $s_i$  lies farther from the imaginary axis. On the other hand, the variance is amplified for points  $s_i$  that lie close to the imaginary axis, i.e.,  $|s_i - j\omega_k| < 1$ . Therefore, the variance of the TFD due to the variance of the FRD in general leads to a small error contribution, especially at points that do not lie close to the imaginary axis.



### 3.3.4 Error bounds in the LHP due to asymmetry

There are two main reasons why the symmetry method underlying (3.21) gives rise to errors in the LHP TFD. First, the symmetry point  $-d$  is computed from the estimated  $\hat{\sigma}_n$  in (3.23) as it is assumed that no parametric model of the system is available. Second, the remaining poles of the system are likely to have a real part that is not equal to  $-d$ . Recall from Figure 3.1 that it is clear that not all poles lie on the dashed line  $\text{Re}(s) = -d$ .

Error bounds due to the symmetry assumption underlying (3.21) are obtained from computing the LHP TFD for extreme values of  $d$ . As the system is stable, a reasonable estimate for  $d_{min}$ , the minimum value of  $d$ , is obtained with  $d_{min} = 0$ . An estimate of  $d_{max}$ , the maximum value of  $d$ , is obtained from the pole in the FRD that associates with the highest resonance frequency, i.e.,  $\hat{\omega}_{nd,max}$ . Assuming that this pole has a damping ratio  $\hat{\zeta}$ , (3.23) gives  $d_{max} = \hat{\zeta}\hat{\omega}_{nd,max}$ . In this way, two limits can be defined:

$$\hat{\mathbf{H}}_{min}(-s_i) = \hat{\mathbf{H}}(s_i - 2d_{min}), \quad (3.37)$$

$$\hat{\mathbf{H}}_{max}(-s_i) = \hat{\mathbf{H}}(s_i - 2d_{max}). \quad (3.38)$$

An error estimate now follows from the difference between the LHP TFD computed with (3.21) and these limits. So for each entry of the MIMO system it holds that

$$|\hat{E}_{m,yu}(-s_i)| \leq \max(|\hat{H}_{min,yu}(-s_i) - \hat{H}_{yu}(-s_i)|, |\hat{H}_{max,yu}(-s_i) - \hat{H}_{yu}(-s_i)|). \quad (3.39)$$

### 3.3.5 Total error bound

Using the error bounds derived in the preceding sections, the total error bound can be given as follows. A worst case approximation of the bound on the error  $\hat{\mathbf{E}}_{tot}(s_i)$  of the computed TFD in the right half-plane is to assume that none of the error terms cancel with each other, or

$$|\Delta\hat{\mathbf{H}}(s_i)| \leq |\hat{\mathbf{E}}_n(s_i)| + |\hat{\mathbf{E}}_i(s_i)| + |\hat{\mathbf{E}}_f(s_i)|, \quad \text{Re}(s_i) > 0. \quad (3.40)$$

In the LHP the extra error caused by the symmetry condition causes the error bound to be estimated by

$$|\Delta\hat{\mathbf{H}}(s_i)| \leq |\hat{\mathbf{E}}_n(s_i)| + |\hat{\mathbf{E}}_i(s_i)| + |\hat{\mathbf{E}}_f(s_i)| + |\hat{\mathbf{E}}_m(s_i)|, \quad \text{Re}(s_i) < 0. \quad (3.41)$$

The true value of the TFD point  $\mathbf{H}(s_i)$  lies within a circle with a radius  $|\Delta\hat{\mathbf{H}}(s_i)|$  about the estimated TFD  $\hat{\mathbf{H}}(s_i)$ . That is,  $\mathbf{H}(s_i)$  satisfies

$$\mathbf{H}(s_i) \in \hat{\mathbf{H}}(s_i) + \mathbf{R} \odot |\Delta\hat{\mathbf{H}}(s_i)| \odot e^{i\Phi}. \quad (3.42)$$

Here,  $\mathbf{R}$  and  $\Phi$  are matrices with the same size as  $\hat{\mathbf{H}}(s_i)$ , whose entries satisfy

$$0 \leq R_{yu} \leq 1, \quad (3.43)$$

$$0 \leq \Phi_{yu} \leq 2\pi. \quad (3.44)$$

In this way, a set of points is computed that encapsulates the true value  $\mathbf{H}(s_i)$  at  $s_i$ .  $R_{yu}$  and  $\Phi_{yu}$  will be considered to be independent for each entry in the computation of this set of points. This obviously gives a conservative uncertainty bound as not all parameters are independent. For example, the error in the estimation of the symmetry point  $d$  in (3.39) will be the same for each entry of the MIMO system. However, this assumption facilitates the uncertainty computation and ensures that (3.42) will hold. This uncertainty description of the MIMO TFD will be used in the subsequent sections to estimate error bounds on the computed closed-loop poles.

## 3.4 Computation of closed-loop poles using TFD

The MIMO TFD enables the estimation of the closed-loop poles of the system to be controlled with a given controller  $\mathbf{C}(s)$ . The closed-loop pole locations provide important information on the damping and frequency contents of the closed-loop response of the system that can aid the control design engineer in his tuning tasks.

### 3.4.1 Theory

Key in the computation of the closed-loop poles  $p_{cl}$  is the determinant of the return difference  $\mathbf{I} + \mathbf{H}(s)\mathbf{C}(s)$ , which is given by

$$\mathcal{D}(s) := \det(\mathbf{I} + \mathbf{H}(s)\mathbf{C}(s)). \quad (3.45)$$

$\mathcal{D}(s)$  can be related to the open-loop  $\phi_{ol}(s)$  and closed-loop characteristic polynomial  $\phi_{cl}(s)$  of the system, which are defined by

$$\phi_{ol} = \prod_{k=1}^{N_{ol}} (s - p_{ol,k})^{n_{ol,k}}, \quad (3.46)$$

$$\phi_{cl} = \prod_{l=1}^{N_{cl}} (s - p_{cl,l})^{n_{cl,l}}, \quad (3.47)$$

where  $p_{ol}$  are the open-loop poles of the system.  $N_{ol}$  and  $N_{cl}$  denote the number of open- and closed-loop poles respectively, while  $n_{ol,k}$  and  $n_{cl,l}$  denote the multiplicity of each pole. For  $\mathcal{D}(s)$  in (3.45) it holds that

$$\mathcal{D}(s) = c \frac{\phi_{cl}(s)}{\phi_{ol}(s)}, \quad (3.48)$$

where  $c$  is a constant (Skogestad and Postlethwaite, 2005). Therefore, the closed-loop poles  $p_{cl}$  satisfy

$$p_{cl} = \{s \in \mathbb{C} \mid \mathcal{D}(s) = 0\}. \quad (3.49)$$

Consider the estimate of  $\mathcal{D}$ , given by

$$\hat{\mathcal{D}}(s_i) = \det(\mathbf{I} + \hat{\mathbf{H}}(s_i)\mathbf{C}(s_i)), \quad (3.50)$$

which is obtained from the TFD estimate  $\hat{\mathbf{H}}(s_i)$  and substitution of  $s_i$  in the controller  $\mathbf{C}(s)$ . TFD is computed for a grid of points  $s_i$ , but  $p_{cl}$  will in general lie somewhere in between the grid points  $s_i$ . A solution to this problem could be to search for points  $s_i$  where the magnitude  $|\hat{\mathcal{D}}(s_i)|$  has a (local) minimum. But, there is no guarantee that this local minimum will actually be a pole location. Furthermore, this approach would be sensitive to noise as the detection of the pole would be based on a single data point. Therefore, a more robust solution is proposed. First, splitting the determinant in a real part  $u(s)$  and an imaginary part  $v(s)$  gives

$$\mathcal{D}(s) = u(s) + jv(s). \quad (3.51)$$

It is obvious that (3.49) can be split up too, giving

$$p_{cl} = \{s \in \mathbb{C} \mid u(s) = 0 \wedge v(s) = 0\}. \quad (3.52)$$

The determinant is a complex function that is analytic on its entire domain except for a discrete number of points. These points correspond to the pole locations of the function, which are the open-loop poles according to (3.48). This means that  $\mathcal{D}(s)$  is continuously differentiable, and consequently,  $u(s)$  and  $v(s)$  are continuously

differentiable, except at the open-loop pole locations. As a result  $u(s) = 0$  and  $v(s) = 0$  form continuous contours in the  $s$ -plane. According to (3.52) the closed-loop poles will lie at the intersection points of these contours. Finding the contours is a robust procedure since generally a set of points is used to determine these contours. For convenience of notation, the  $u(s) = 0$  contours will be referred to as  $u$ -contours, and the  $v(s) = 0$  contours as  $v$ -contours. Figure 3.2 shows an illustration of a  $u$ -contour and a  $v$ -contour. It can be seen that the contours intersect at the closed-loop (and open-loop) pole location.

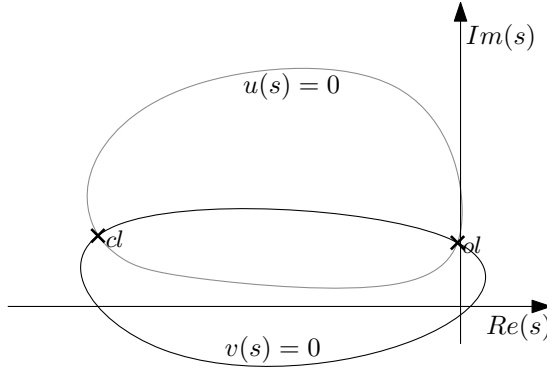


Figure 3.2: The  $u$ -contour and  $v$ -contour in the  $s$ -plane intersect at the closed-loop and open-loop pole locations.

The  $u$ - and  $v$ -contours have several interesting properties. For example, it will be shown that these contours intersect each other at predefined angles. Furthermore, it will become clear that besides the closed-loop poles, also the open-loop poles lie on intersections of the  $u$ - and  $v$ -contours. An analysis of the phase of  $\mathcal{D}(s)$  is required to derive these properties.

The phase of  $\mathcal{D}(s)$  at  $s$  is determined by summation of all the angles of the open- and closed-loop poles with respect to the point  $s$  (Franklin et al., 2002; Ash and Ash, 1968). This follows from

$$\angle \mathcal{D}(s) = \sum_k^{N_{ol}} n_{ol,k} \angle(s - p_{ol,k}) - \sum_l^{N_{cl}} n_{cl,l} \angle(s - p_{cl,l}). \quad (3.53)$$

In the vicinity of one of the poles, e.g.,  $p_{cl,l}$ , the phase is completely determined by the location of  $s$  with respect to this pole. This can be seen from Figure 3.3. Taking

$$s_c(\phi) = p_{cl,l} + re^{i\phi}, \quad (3.54)$$

i.e., a small circle with radius  $r$  and  $\phi \in [0, 2\pi]$  around  $p_{cl,l}$ , it is clear that for  $r \rightarrow 0$  the angles of all other poles  $\phi_1$ ,  $\phi_2$  and  $\phi_3$  with respect to  $s_c$  are constant on this circle. Therefore it holds that for  $r \rightarrow 0$ ,

$$\begin{aligned}
 \angle \mathcal{D}(s_c(\phi)) &= -n_{cl,l} \angle(s_c - p_{cl,l}) + c \\
 &= -n_{cl,l} \angle(p_{cl,l} + re^{i\phi} - p_{cl,l}) + c \\
 &= -n_{cl,l} \angle(re^{i\phi}) + c \\
 &= -n_{cl,l} \phi + c,
 \end{aligned} \tag{3.55}$$

where  $c$  is the total contribution of all other poles. Thus, the phase of  $\mathcal{D}(s)$  around the pole changes with  $-n_{cl,l}\phi$  while encircling the pole, where  $n_{cl,l}$  is the multiplicity of the closed-loop pole. The derivation is completely analogous for an open-loop pole, apart from the change of sign of the phase according to (3.53).

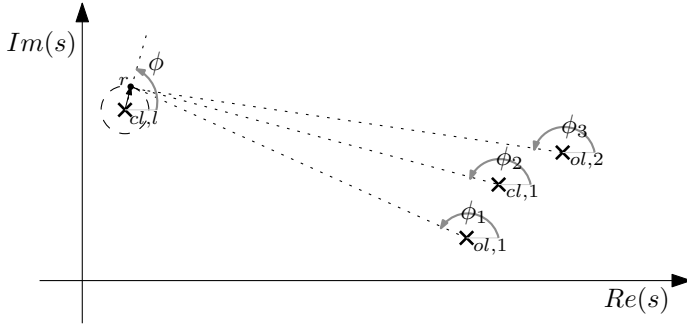


Figure 3.3: In the vicinity of pole  $p_{cl,l}$ , the change in phase of  $\mathcal{D}(s_i)$  is completely determined by this pole.

The phase of  $\mathcal{D}(s_i)$  can be related to the  $u$ - and  $v$ -contours as follows. At  $u$ -contours,  $\mathcal{D}(s)$  is purely imaginary giving

$$\angle \mathcal{D}(s) = \frac{\pi}{2} + n\pi, \tag{3.56}$$

where  $n \in \mathbb{N}$ , while for  $v$ -contours

$$\angle \mathcal{D}(s) = 0 + n\pi. \tag{3.57}$$

For a pole with multiplicity equal to one, the phase of  $\mathcal{D}(s)$  around the pole changes  $2\pi$  according to (3.55), which means that there will be one  $u$ - and one  $v$ -contour intersecting at this point having a  $90^\circ$  angle at the intersection point, see Figure 3.4. In general, the angles between the  $u$ - and  $v$ -contours at a closed-loop pole

with multiplicity  $n_{cl,l}$  will be equal to

$$\angle(u, v) = \frac{90^\circ}{n_{cl,l}}. \quad (3.58)$$

Of course, the same relation holds in case of an open-loop pole (replacing  $n_{cl,k}$  with  $n_{ol,l}$  in (3.58)). The pattern for a pole with multiplicity equal to three is shown in Figure 3.4 as well. These properties of the  $u$ - and  $v$ -contours are of course closely related to the well known root-locus sketching rules (Franklin et al., 2002).

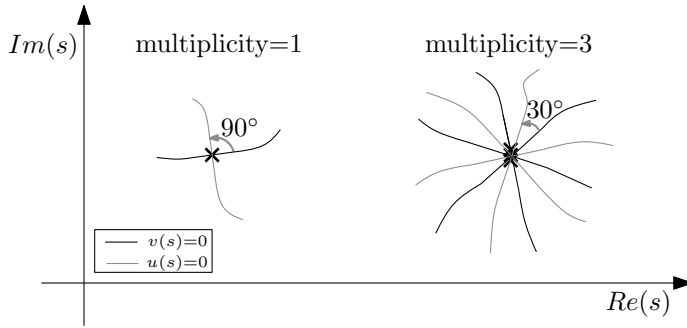


Figure 3.4: Patterns of the  $u$ - and  $v$ -contours depending on the multiplicity of the poles.

It might seem strange at first that also the open-loop poles  $p_{ol}$  lie at intersections of the  $u$ - and  $v$ -contours, as  $|\mathcal{D}(s)| = \infty$  at these locations. The explanation lies in the fact that  $p_{ol}$  are singular points of the complex function  $\mathcal{D}(s)$ . At  $p_{ol}$  the value is indeed indefinite, see Figure 3.5 for an example of the behaviour around  $p_{ol}$ . In the figure,  $u(s)$  and  $v(s)$  are plotted along the  $u$ -contour that goes through an open-loop pole  $p_{ol}$ . It can be observed that  $u(s) = 0$  except for the singular point, while  $v(s)$  shows asymptotic behaviour. The plot along the  $v$ -contour would look exactly opposite;  $v(s) = 0$  except for the singular point, while  $u(s)$  shows asymptotic behaviour. This explains how the magnitude  $|\mathcal{D}(s)|$  can go to infinity while at the same point the  $u$ - and  $v$ -contours intersect. This also indicates the possibility to distinguish between open-loop and closed-loop poles, namely, by inspecting  $|\mathcal{D}(s)|$  near the pole location. Low amplitudes near an intersection point are an indication for a closed-loop pole, while high amplitudes indicate the presence of an open-loop pole.

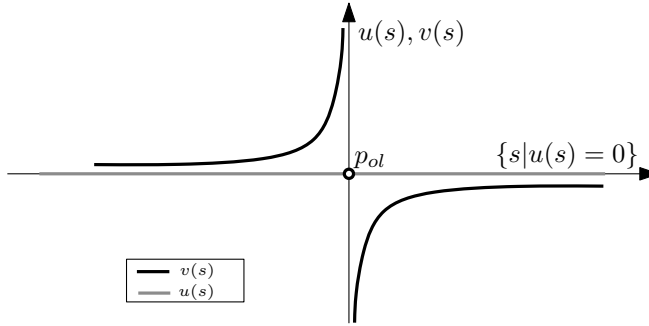


Figure 3.5: Value of  $u(s)$  and  $v(s)$  along a  $u$ -contour that passes through an open-loop pole  $p_{ol}$ .

### 3.4.2 Computational aspects

Using the TFD estimates of  $u(s)$  and  $v(s)$ , which are denoted by  $\hat{u}(s_i)$  and  $\hat{v}(s_i)$ ,  $\hat{\mathcal{D}}(s_i)$  is defined by

$$\hat{\mathcal{D}}(s_i) = \det(I + \hat{\mathbf{H}}(s_i)\mathbf{C}(s_i)) \quad (3.59)$$

$$= \hat{u}(s_i) + j\hat{v}(s_i). \quad (3.60)$$

A computationally cheap and reliable method to estimate the points where  $u(s)$  and  $v(s)$  are zero is to search for zero crossings in  $\hat{u}(s_i)$  and  $\hat{v}(s_i)$ . The idea is illustrated in Figure 3.6, where the value of  $\hat{u}(s_i)$  is plotted in the  $s$ -plane. For each point  $s_i$  it is checked whether

$$\text{sign}[\hat{u}(s_i)] \neq \text{sign}[\hat{u}(s_j)], \quad (3.61)$$

where  $s_j$  is a neighboring point of  $s_i$ . As  $u(s)$  is a continuously differentiable function, it must have a zero crossing somewhere between  $s_i$  and  $s_j$ . Linear interpolation is used to estimate this zero crossing

$$\hat{s}_{cross,u} = \frac{|\hat{u}(s_i)|s_j + |\hat{u}(s_j)|s_i}{|\hat{u}(s_i)| + |\hat{u}(s_j)|}. \quad (3.62)$$

In Figure 3.6, the points  $\hat{s}_{cross,u}$  are indicated by the grey  $\circ$  markers. These points can be connected to each other to form the estimated  $\hat{u}$ -contour, which is a continuous contour in the  $s$ -plane. The derivation for the estimated  $\hat{v}$ -contours is completely analogous. Figure 3.7 gives an illustration of estimated  $\hat{u}$ - and  $\hat{v}$ -contours and the resulting pole locations at the intersection points.

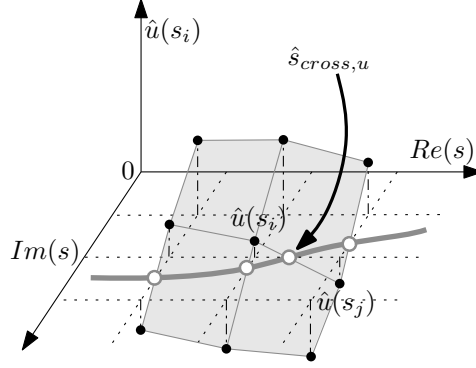


Figure 3.6: The zero crossings (grey  $\circ$ ) in  $\hat{u}(s_i)$  provide an estimate of the  $u$ -contours (grey line).

To estimate the pole locations, it is detected whether the estimated  $\hat{u}$ - and  $\hat{v}$ -contours intersect within a square formed by four grid points. This is illustrated in Figure 3.8, which shows a detailed inset of the area around the closed-loop pole of Figure 3.7. An approximation of the pole location is made by connecting the points  $\hat{s}_{cross,u}$  and  $\hat{s}_{cross,v}$  by the straight lines

$$\omega = a_u \sigma + b_u \quad (3.63)$$

$$\omega = a_v \sigma + b_v, \quad (3.64)$$

where  $\sigma = \text{Re}(s)$  and  $\omega = \text{Im}(s)$ . Here,  $a_u$  and  $a_v$  are the slopes of the lines and  $b_u$  and  $b_v$  the intersection points of the lines with the imaginary axis. These coefficients are computed from  $\hat{s}_{cross,u}$  and  $\hat{s}_{cross,v}$ . The intersection point of these lines is given by

$$\sigma_p = \frac{b_u - b_v}{a_v - a_u} \quad (3.65)$$

$$\omega_p = a_u \sigma_p + b_u. \quad (3.66)$$

If the intersection point exists (i.e.,  $a_v \neq a_u$ ) and if the point lies within the four grid points, the estimated pole location is considered valid. The estimated pole is then equal to

$$\hat{p}_{cl} = \sigma_p + j\omega_p. \quad (3.67)$$

To distinguish an open-loop pole from a closed-loop pole, the magnitude  $|\hat{\mathcal{D}}(s_i)|$  is evaluated at one of the four points  $s_i$  that surround the estimated pole location.



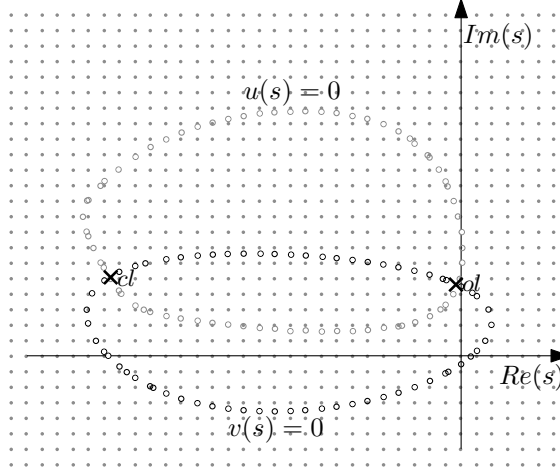


Figure 3.7: The  $\hat{u}$ -contour (grey  $\circ$ ) and  $\hat{v}$ -contour ( $\circ$ ) in the  $s$ -plane intersect at the closed-loop and open-loop pole locations ( $\times$ ). The grey dots indicate the grid points at which the TFD is computed.

One might even think to use the computation of the open-loop pole locations to construct a parametric model of the system to be controlled. However, accurate estimation of the open-loop pole locations is hampered by two issues. Firstly, close to the imaginary axis, the TFD strongly depends on the chosen symmetry point  $\sigma_n$ . Secondly, the variance on the TFD near the imaginary axis is usually larger, recall Section 3.3.3. Moreover, the pole locations alone do not provide sufficient information to construct a parametric model. This would also require the residue matrices of the poles.

### 3.4.3 Uncertainty in pole locations

Using the uncertainty estimation  $|\Delta \hat{\mathbf{H}}(s_i)|$  of the TFD, given in (3.42), enables the computation of an estimate of the uncertainty  $\Delta \hat{p}_{cl}$  of the estimated pole location  $\hat{p}_{cl}$ . Due to the determinant in (3.59), computing  $\Delta \hat{p}_{cl}$  from  $|\Delta \hat{\mathbf{H}}(s_i)|$  cannot be done analytically. Therefore, a numerical solution is used to estimate  $\Delta \hat{p}_{cl}$ . The idea is to generate  $N_r$  realizations  $\hat{\mathbf{H}}_r(s_i)$  of uncertain TFD, or

$$\hat{\mathbf{H}}_r(s_i) = \hat{\mathbf{H}}(s_i) + \mathbf{R}_r \odot |\Delta \hat{\mathbf{H}}(s_i)| \odot e^{i\Phi_r}, \quad (3.68)$$

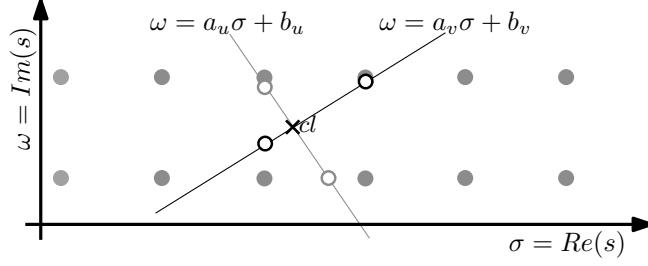


Figure 3.8: The estimated pole location lies at the estimated intersection point of the  $\hat{u}$ - and  $\hat{v}$ -contour.

where  $r = 1..N_r$ , and in which  $\mathbf{R}_r$  and  $\Phi_r$  are matrices with the same size as  $\Delta \hat{\mathbf{H}}(s_i)$ . Their entries

$$R_{r_{out,in}} \in [0, 1], \quad (3.69)$$

$$\Phi_{r_{out,in}} \in [0, 2\pi], \quad (3.70)$$

are chosen from a uniform random distribution. For each input-output entry,  $R_{out,in}$  and  $\Phi_{out,in}$  are chosen independent of the other entries. Each realization, gives a realization of the determinant according to

$$\hat{\mathcal{D}}_r(s_i) = \det(I + \hat{\mathbf{H}}_r(s_i)\mathbf{C}(s_i)), \quad (3.71)$$

which is used to compute the perturbed closed-loop pole locations from (3.67). This approach will give a set of poles  $\hat{p}_{cl,r}$  that lie around the estimated pole location  $\hat{p}_{cl}$ . Subsequently, the uncertainty bounds  $\Delta \hat{p}_{cl}$  are chosen such that every  $\hat{p}_{cl,r}$  lies within these bounds.

### 3.4.4 Grid selection

The selection of the number and location of the grid points  $s_i$  at which the TFD is computed largely influences the successful application of the proposed method. As  $s_i = \sigma_i + j\omega_i$  is complex, the ranges of both the real part  $\sigma_i$  and the imaginary part  $\omega_i$  have to be selected. Selection of the range for  $\omega_i$  is straightforward. The relevant frequency range can be obtained from the FRD since the lightly damped resonances will be clearly visible. The analysis often focusses on a specific mode, which makes it convenient to choose a frequency range around this mode. The range of  $\sigma_i$  has to be determined in an iterative way, as initially the closed-loop

pole locations are unknown. In general, a reasonable initial guess is to take a range that contains all open-loop poles of the plant and controller.

The resolution of the points in both the real and imaginary range have to be determined in an iterative way as well. It is not necessary to use the same frequency points  $\omega_k$  as in the measured FRD, the resolution can be higher or lower depending on the required accuracy and the constraints on computation time. The  $\hat{u}$ - and  $\hat{v}$ -contours can be inspected to see whether the ranges and resolutions are properly chosen. A properly chosen range and resolution gives continuous contours that run from one pole location to another. The controller poles are known and the open-loop poles of the plant can be estimated from the FRD by inspection of the peaks in the Bode magnitude plot. As the number of closed-loop poles equals the number of open-loop poles, the range and resolution can be adjusted until all closed-loop poles become visible.

The resolution also influences the discrimination between an open-loop and a closed-loop pole. The magnitude of  $\hat{\mathcal{D}}(s_i)$  is only a good indicator if the (checked) point  $s_i$  lies close to the actual pole location. Another issue that can occur is that a closed-loop pole location coincides with an open-loop pole location. In that case it is clear from (3.48) that the open-loop pole cancels the closed-loop pole in  $\mathcal{D}(s)$ . This occurs, for example, when the controller gain is low. However, as the open-loop poles of the plant can be observed in the FRD this is not a problem in practice.

Iterating over different grids is not very time-consuming, even though both the TFD, the  $\hat{u}$ - and  $\hat{v}$ -contours, and the pole locations have to be recomputed. For example to recompute a grid of  $50 \times 50$   $s_i$  points for a  $4 \times 4$  MIMO system using FRD with 5000 frequency points takes less than 45 seconds. In Chapter 2 it was derived that the computation of the TFD at one point  $s_i$  from 5000 FRD points takes approximately 1 millisecond using a standard pc (2.4GHz dual-core, 4GB RAM). Thus for the MIMO system  $50 \times 50 \times 4 \times 4 = 40000$  TFD points  $\hat{\mathbf{H}}(s_i)$  are computed, which takes approximately 40 seconds. From  $\hat{\mathbf{H}}(s_i)$  and the controller TFD  $\mathbf{C}(s_i)$  the 2500 points of the determinant  $\hat{\mathcal{D}}(s_i)$  are computed. Subsequently, the zero crossings of  $\hat{\mathcal{D}}(s_i)$  are computed to estimate the  $\hat{u}$ - and  $\hat{v}$ -contours and the pole locations, which takes less than 5 seconds.

## 3.5 Experiments and design

So far it has been discussed how to compute TFD from FRD and how to compute closed-loop poles using TFD without having a parametric model of the system to be controlled. This section presents experiments that validate the computed closed-

loop pole locations. Furthermore a design example is included that demonstrates the use of TFD in a control design to increase the damping of a number of resonant modes.

### 3.5.1 The setup: a prototype wafer stage

The experiments presented in this section have been conducted on an industrial prototype wafer stage, see Figure 3.9. To enable large accelerations, the chuck is designed to have a low mass, its weight is only 13.5 kg. The large size of the chuck,  $600 \times 600$  mm, in combination with the low weight, causes structural deformations to become important within the control design.



Figure 3.9: Industrial prototype wafer stage. The wafer stage (left) has been removed from the metrology frame (right) to disclose its rectangular wafer chuck.

As the wafer stage is magnetically levitated, all six rigid-body degrees-of-freedom ( $x, y, R_z, z, R_x, R_y$ ) have to be controlled. The stage is relatively stiff in the in-plane directions  $x, y$  and  $R_z$ . The out-of-plane directions  $z, R_x$  and  $R_y$  on the other hand, associate with relatively low stiffness, hence the flexible modes manifest themselves predominantly in the out-of-plane dynamics of the wafer stage. The flexible mode associated with the lowest resonance frequency is a torsion mode at 142 Hz. The stage has eight actuators (4 in-plane, 4-out-of-plane) and seven sensors (3 in-plane, 4-out-of-plane). This makes it possible to decouple the system  $\mathbf{H}(s)$  in its six rigid-body degrees-of-freedom plus in an extra direction, for example

direction given by the torsion mode  $T$ , according to

$$\mathbf{H}_{dec}(s) = \mathbf{T}_y \mathbf{H}(s) \mathbf{T}_u, \quad (3.72)$$

where  $\mathbf{T}_y$  is the  $7 \times 7$  sensor transformation matrix and  $\mathbf{T}_u$  is the  $7 \times 8$  actuator transformation matrix. To keep the analysis transparent only the out-of-plane directions of  $\mathbf{H}_{dec}(s)$  are considered, which are  $z$ ,  $R_x$ ,  $R_y$  and  $T$ .

Two examples of the application of TFD will be presented in this chapter. The first example shows the computation of a root-locus for the torsion mode of the setup. This example deals with the validation of the closed-loop poles by comparing them to time domain data. The second example presents a loop-shaping control design that incorporates TFD in the design to increase the damping of the modes around 500 Hz. But prior to these examples, the identification, control design and computation of TFD is discussed.

### 3.5.2 Identification

A non-parametric identification experiment has been conducted using a closed-loop multisine approach (Pintelon and Schoukens, 2001). Controllers with a 50 Hz bandwidth were used during identification. The four decoupled out-of-plane inputs were excited by multisine excitation signals (50 periods, 4 realizations). The plant outputs and controller outputs were measured at a sampling rate of 10 kHz, from which FRD at  $w_k = [1, 2, \dots, 4999]$  Hz was computed, see Figure 3.10. In this figure, rigid-body dynamics can be observed in  $z$ ,  $R_x$  and  $R_y$  directions, characterized by  $-2$ -slopes at low frequencies. Furthermore, flexible modes around 500 and 700 Hz can be observed in these entries. The torsion direction shows a typical flexible mode transfer function; a stiffness line at low frequencies followed by a resonance and a minus-two slope. The modes at 500 and 700 Hz are not visible in this transfer function due to the decoupling.

### 3.5.3 Control Design

Loop-shaping is used to design controllers for the out-of-plane directions of the wafer stage. For robustness, the decentralized controllers are designed with a sensitivity  $|S| < 6$  dB. The achieved bandwidths (cross-over frequencies) for  $z$ ,  $R_x$  and  $R_y$  are 75 Hz. For the  $z$ -direction the controller contains an integrator, a lead filter, two notch filters and a second-order low-pass filter giving,

$$C_z(s) = k_z C_i(s) C_l(s) C_{n1}(s) C_{n2}(s) C_{lp2}(s), \quad (3.73)$$

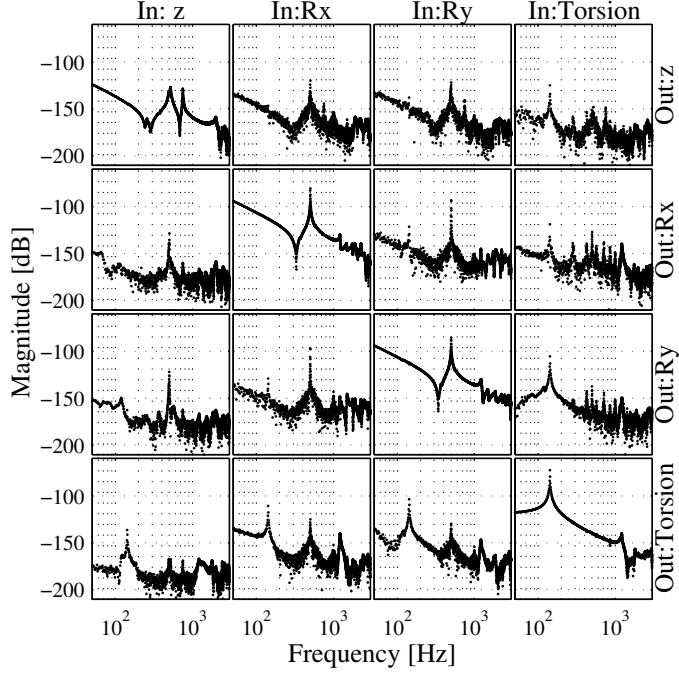


Figure 3.10: Measured FRD of the out-of-plane directions of the wafer stage.

where

$$C_i(s) = \frac{s + 2\pi f_i}{s}, \quad (3.74)$$

$$C_l(s) = \frac{\frac{s}{2\pi f_{l,z}} + 1}{\frac{s}{2\pi f_{l,p}} + 1}, \quad (3.75)$$

$$C_{lp2}(s) = \frac{1}{\left(\frac{s}{2\pi f_{lp2}}\right)^2 + \frac{2\beta_{lp2}s}{2\pi f_{lp2}} + 1}. \quad (3.76)$$

$$C_{ni}(s) = \frac{\left(\frac{s}{2\pi f_{ni,z}}\right)^2 + \frac{2\beta_{ni,z}s}{2\pi f_{ni,z}} + 1}{\left(\frac{s}{2\pi f_{ni,p}}\right)^2 + \frac{2\beta_{ni,p}s}{2\pi f_{ni,p}} + 1}. \quad (3.77)$$

The parameters are  $k_z = 1.18 \cdot 10^6$  N/m,  $f_i = 10$  Hz,  $f_{l,z} = 25$ ,  $f_{l,p} = 252$  Hz,  $f_{n1,z} = f_{n1,p} = 507$  Hz,  $\beta_{n1,z} = 0.01$ ,  $\beta_{n1,p} = 0.4$ ,  $f_{n2,z} = f_{n2,p} = 748$  Hz,  $\beta_{n1,z} = 0.005$ ,  $\beta_{n1,p} = 0.5$ ,  $f_{lp2} = 1000$  Hz and  $\beta_{lp2} = 0.5$ . The controllers for the  $R_x$  and  $R_y$  direction are given by

$$C_{R_x}(s) = C_{R_y}(s) = k_R C_i(s) C_l(s) C_n(s) C_{lp2}(s), \quad (3.78)$$

where  $k_R = 3.7 \cdot 10^4$  N/rad,  $f_i = 10$  Hz,  $f_{l,z} = 25$ ,  $f_{l,p} = 375$  Hz,  $f_{n,z} = f_{n,p} = 502$  Hz,  $\beta_{n,z} = 0.01$ ,  $\beta_{n,p} = 0.6$ ,  $f_{lp2} = 1000$  Hz and  $\beta_{lp2} = 0.5$ . The controller for the torsion direction  $T$  is given by

$$C_T(s) = k_T C_i(s) C_l(s) C_{lp1}(s), \quad (3.79)$$

where a first-order low-pass filter

$$C_{lp1}(s) = \frac{1}{\frac{s}{2\pi f_{lp1}} + 1}, \quad (3.80)$$

was used. The parameters are  $k_T = 1216$  N/m,  $f_{lp1} = f_i = 1$  Hz,  $f_{l,z} = 49$ ,  $f_{l,p} = 444$  Hz.

### 3.5.4 TFD of the setup

From the measured FRD  $\hat{\mathbf{H}}(j\omega_k)$ , TFD  $\hat{\mathbf{H}}(s_i)$  is computed using (3.10). As explained, the computation of TFD is performed separately for each entry in the MIMO system. A 3D-Bode diagram of the (1,1) entry of the TFD is shown in Figure 3.11 as an example. Note that for  $Re(s) = 0$ , the TFD is equal to the FRD obtained from measurement. This can be observed by comparing the (1,1) entry of the FRD in Figure 3.10 with Figure 3.11.

From Section 3.2 it is clear that in the computation of TFD, the choice of parameters plays a crucial role. Firstly, the choices made during the identification of the FRD determine that  $\omega_{max} = 4999$  Hz and  $\Delta\omega = 1$  Hz. Secondly, the  $z$ ,  $R_x$  and  $R_y$  directions contain pure integrators, such that (3.16) has to be used in order to compute the TFD for these entries. The parameters of the  $W$  filter are chosen to be  $f_W = 100$  Hz and  $\beta_W = 0.8$ . Thirdly, the computation of LHP TFD is done using the symmetry condition in (3.21) with the aid of (3.23) to compute the symmetry point  $d$ ;  $\hat{\zeta} = 0.003$  is used as being the mean value of the range  $\zeta \approx 0.001 - 0.005$  that is proposed in Preumont (2011). For the frequency  $\omega_{nd}$ , two values are used in the subsequent sections. In Section 3.5.5  $w_{nd} = 142$  Hz because it corresponds to the torsion mode that will be analysed. In Section 3.5.6  $w_{nd} = 517$  Hz, i.e., the mean value of the resonance frequencies of the modes around 500 Hz. This results in  $d = 2.7$  and  $d = 9.7$ , respectively.

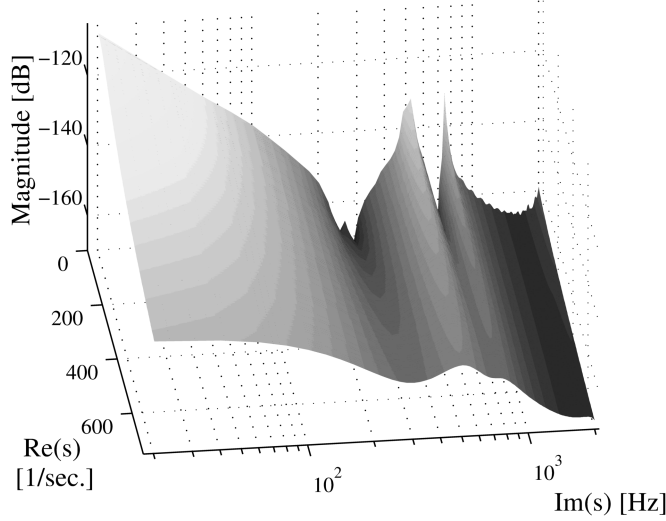


Figure 3.11: 3D Bode diagram of the (1,1) entry of the TFD of the OAT setup.

The error bound  $\Delta\hat{\mathbf{H}}(s_i)$  in (3.40) is computed according to the results presented in Section 3.3. Firstly, the error due to the definite integral includes the fact that  $\omega_{max} = 4999$ . Secondly, the variance on the TFD is computed using (3.33), where the variance on the FRD is computed from (3.32). Thirdly, the error due to the integration method is computed using (3.31). Finally, the error due to the symmetry condition is estimated from (3.39) where  $d_{min} = 0$  and  $d_{max} = 13.2$ . The latter is taken from the most dominant high-frequency mode, which is found at 700 Hz, thus choosing  $\omega_{nd} = 2\pi 700$  in (3.23).

### 3.5.5 Example 1: Root-locus torsion mode

To validate the computation of the closed-loop pole locations a data-based root-locus will be computed for the torsion mode of the setup. This is achieved by computing the closed-loop poles for a number of different gains  $k_T$  of the torsion controller. The closed-loop poles are estimated from time-domain responses measured on the setup as to validate the closed-loop poles obtained from TFD.

The torsion controller contains a lead filter as to increase the phase around the torsion mode to increase the damping of this mode. The torsion controller gives a stable closed-loop for a large range of values for  $0 \leq k_T \leq 64 \cdot 10^4$ . However,



it is not clear which value for  $k_T$  will give the best amount of damping. This information cannot be obtained using loop-shaping techniques, as information on the closed-loop pole locations is required. TFD enables the computation of the closed-loop poles of the setup using the method discussed in Section 3.4 and as such does provide the required information.

The estimated determinant  $\hat{D}(s_i)$  is computed for different values of the gain  $k_T = 4, 8, \dots, 64 \cdot 10^4$  using (3.59). Next, the  $\hat{u}$ - and  $\hat{v}$ -contours and closed-loop pole locations are estimated for each gain. For  $k_T = 20 \cdot 10^4$ , these contours are depicted in Figure 3.12. The thick black  $\times$  indicates the location of the closed-loop pole  $\hat{p}_{cl}$ , whereas the grey ellipse indicates the uncertainty bound on the pole location. This bound is computed by generating 50 realizations according to (3.71) and computing the pole locations for each realization  $\hat{p}_{cl,r}$ . The ellipse is drawn in such a way that all  $\hat{p}_{cl,r}$  lie within the ellipse. From the computed uncertainty on the TFD, the uncertainty of the closed-loop pole locations is visualized.

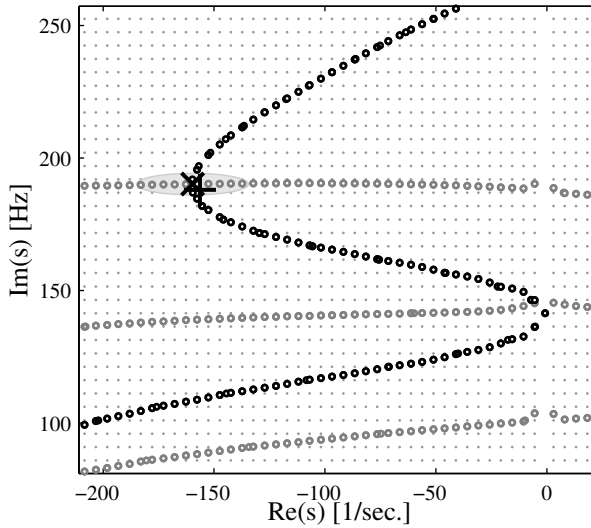


Figure 3.12:  $\hat{u}$ -contours (grey  $\circ$ ) and  $\hat{v}$ -contours (black  $\circ$ ) of the setup for  $k = 20 \cdot 10^4$ . The closed-loop pole location  $\times$  and its uncertainty (grey ellipse) lie at the intersection of these contours. The pole location obtained from time-domain experiments is shown by  $+$ .

To validate the pole locations computed from TFD, an impulse response measurement has been conducted for each value of  $k_T$ . A block-pulse of 2 N with a duration of 2 milliseconds is applied to the torsion input of the system, and the

response  $y_t$  at the torsion output is measured. Figure 3.13 shows the response for  $k_T = 20 \cdot 10^4$ . The measured response is plotted in the bottom left part of the figure in black. As the response is dominated by the torsion mode, the response can be approximated by

$$y_t(t) \approx c e^{\hat{p}_{cl}t} = c e^{\sigma_p t + j\omega_p t} = c e^{\sigma_p t} e^{j\omega_p t}. \quad (3.81)$$

The damping and the dominant frequency of the response are computed to estimate the pole location from this time-domain data. To estimate the damping of the response, a line is fitted through the peaks ( $\circ$ ) of  $|\log(y)|$  as shown in the top part of Figure 3.13. The slope of the line immediately gives the damping coefficient  $\hat{\sigma}_{p,time}$  of the closed-loop pole, which can be used to validate the real part of the closed-loop pole computed from TFD. To estimate the frequency  $\omega_p$  of the oscillation, the Fourier transform of the response is computed, see the right plot. The peak in the spectrum is taken to be the frequency  $\hat{\omega}_{p,time}$  of the closed-loop pole, which can be used to validate the imaginary part of the closed-loop pole that is computed from TFD. The estimate of the closed-loop pole location, or

$$\hat{p}_{time} = \sigma_{p,time} + j\omega_{p,time}, \quad (3.82)$$

is plotted in Figure 3.12 as a black  $+$ . It can be observed that the closed-loop pole estimated from the time-domain data lies within the uncertainty ellipse of the closed-loop pole estimated from TFD.

Figure 3.14 shows the computed pole locations for all values of  $k_T = 4, 8, \dots, 64 \cdot 10^4$ . The pole locations computed from TFD are again plotted with  $\times$  and a grey ellipse which indicates the uncertainty. All poles estimated from the impulse responses ( $+$ ) lie within the uncertainty bounds of the poles estimated from TFD. The closed-loop poles form the root-locus of the system for the parameter  $k_T$ . It is well known that a root-locus starts at an open-loop pole location. For the torsion mode, the open-loop pole is located at 142 Hz, which follows from the FRD, and close to the imaginary axis, due to the low damping. For increasing gains, the closed-loop pole shifts into the LHP until the gain reaches  $k_T = 32 \cdot 10^4$ . Increasing the gain further results in a less damped response and eventually destabilizes the system at  $k_T > 64 \cdot 10^4$ .

These results show that it is possible to accurately estimate the closed-loop poles from TFD. Along the process the controller gain that maximizes the damping of the torsion mode is found to be  $k_T = 32 \cdot 10^4$ . It must be emphasized that this method neither requires a parametric model to compute the closed-loop poles, nor is it necessary to perform impulse response measurements to estimate the closed-loop poles. By extrapolation of the FRD to the entire  $s$ -plane, it is possible to study the closed-loop poles in a completely data-based way.

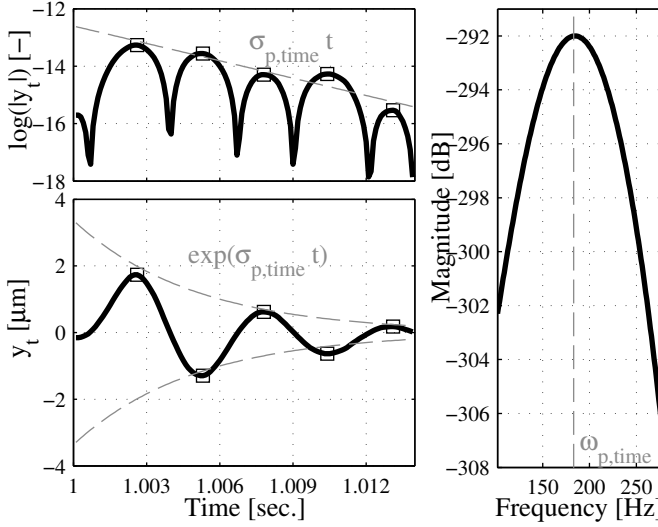


Figure 3.13: Measured impulse response (black) in time (left) and frequency domain (right) and estimation of the closed-loop pole (grey) for  $k = 20 \cdot 10^4$ .

### 3.5.6 Example 2: Damping 500 Hz modes

The second example of the application of TFD is a design example where a controller is designed using loop-shaping, while incorporating the closed-loop pole locations obtained from TFD in the design. The design focusses on the damping of the modes of the wafer stage that lie around 500 Hz.

From a finite element model of the system, it is found that the system has three modes around 500 Hz, namely two bending modes at 501 Hz, and an umbrella mode at 517 Hz. Due to symmetry, the two bending modes have an identical resonance frequency, but one mode shape bends across the  $x$ -axis, while the other bends across the  $y$ -axis. The modes are not decoupled, and appear in most of the entries of the MIMO system, see Figure 3.10. The controllers for the  $z$ ,  $R_x$  and  $R_y$  direction contain notch filters around 500 Hz, the parameters of which are given in Table 3.1. These notch filters prevent excitation of the modes around 500 Hz by reducing the controller gain at these frequencies. This stabilizes the system, but the modes can no longer be actively controlled. It is desirable to actively damp these modes to improve performance, which is otherwise deteriorated by oscillations induced by the excitation of these modes. One approach to achieve this is to use skew-notch filters. In these filters, the frequency of the zeros is not

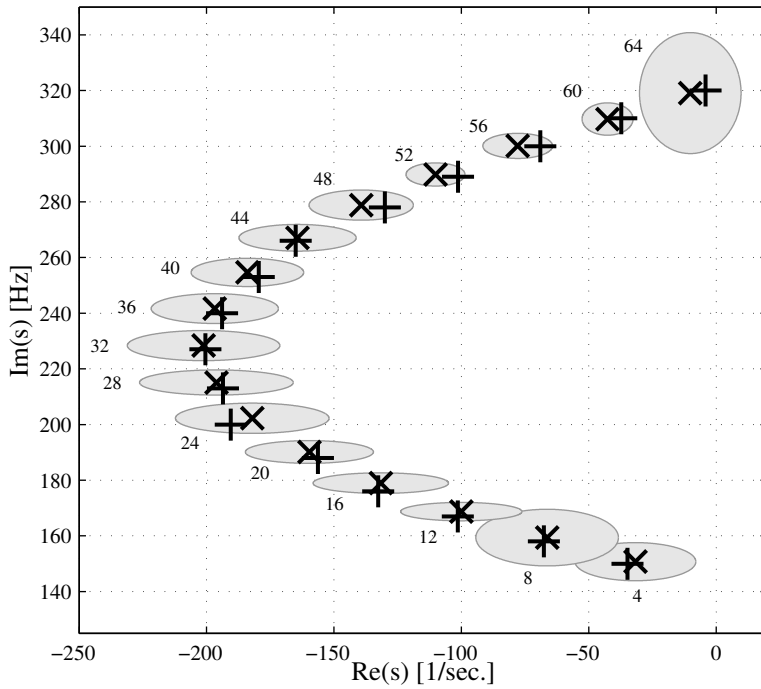


Figure 3.14: Root-locus of the torsion mode of OAT for  $k_T = \{4, 8, \dots, 64\} \cdot 10^4$ . The estimated closed-loop pole locations  $\times$  and uncertainty ellipses (grey) are depicted. The pole locations obtained from time-domain experiments are marked by a  $+$ .

axis	$f_{n,z}$	$\beta_{n,z}$	$f_{n,p}$	$\beta_{n,p}$
$z$	507	0.01	507	0.4
$R_x$	502	0.01	502	0.6
$R_y$	502	0.01	502	0.6

Table 3.1: Conventional notch filters around 500 Hz.

equal to frequency of the poles of the filter, which creates a phase lead (or lag) between these frequencies that can be used to increase damping of the closed-loop system. However, using conventional loop-shaping techniques it is not possible to tune these filters towards optimal damping. This is due to the fact that the Bode and Nyquist plots do not provide information on the closed-loop pole locations.

Using the method described in this chapter, the closed-loop pole locations can be computed, however. This means that the damping of the closed-loop poles can be incorporated in the control design. This is done for the notch filters around 500 Hz. The procedure is to tune one parameter of a notch filter at a time, until optimal damping for this parameter is achieved, and then continue with the next parameter. This procedure is repeated for every parameter that results in a more damped closed-loop system. Note that this procedure will result in a local minimum for the damping of the system and that other (probably) better approaches could be adopted. The key point is that the closed-loop poles are computed in a data-based way. Finding the best control design method to utilize this information is beyond the scope of this chapter.

The closed-loop pole locations are obtained from inspecting the  $\hat{u}$ - and  $\hat{v}$ -contour plot. Each parameter change requires the computation of a new contour plot from which the updated pole locations are computed. This does not require re-computation of the TFD  $\hat{\mathbf{H}}(s_i)$  as the system to be controlled is not changed. However, because the controller  $\mathbf{C}(s)$  changes,  $\mathbf{C}(s_i)$  has to be evaluated on the grid points  $s_i$  to compute (3.59). Next, the  $\hat{u}$ - and  $\hat{v}$ -contour and closed-loop pole locations are computed using (3.62) and (3.67), respectively. For the system under study, these steps are completed within a few seconds on a conventional pc (2.4 GHz dual-core, 4GB RAM).

The  $\hat{u}$ - and  $\hat{v}$ -contour plot for the controller that gives optimal damping is shown in Figure 3.15. Table 3.2 gives the parameters of the skew-notch ellipses that were used. Six closed-loop poles  $\times$  along with the grey uncertainty ellipses can be observed at the intersections of the  $\hat{u}$ - and  $\hat{v}$ -contours. The number of closed-loop poles in this region is six, because the system itself has three open-loop poles, and the controller has three notch filters, which also contain one pole each. Note that we are not counting the complex conjugates of the poles as the analysis is

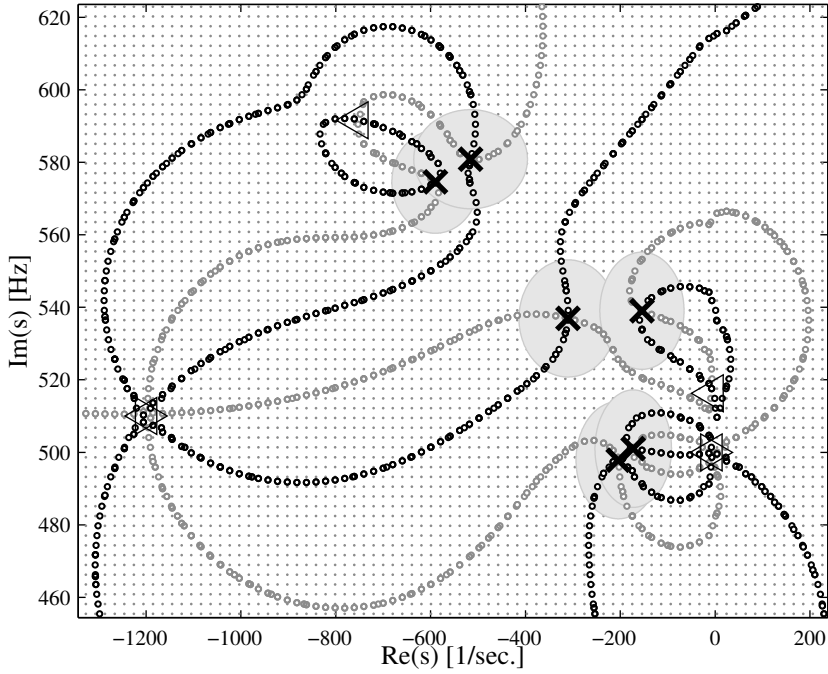


Figure 3.15:  $\hat{u}$ -contours (grey  $\circ$ ) and  $\hat{v}$ -contours (black  $\circ$ ) of the setup for optimal damping of the modes around 500 Hz. The closed-loop pole locations  $\times$  and its uncertainties (grey ellipses) lie at the intersection of these contours. Open loop poles are plotted by  $\triangleleft$  for single multiplicity and  $\star$  for multiplicity equal to two.

limited to the positive imaginary axis. At the closed-loop pole locations, the  $\hat{u}$ - and  $\hat{v}$ -contours intersect with  $90^\circ$  angles, which follows from (3.58).

axis	$f_{n,z}$	$\beta_{n,z}$	$f_{n,p}$	$\beta_{n,p}$	$f_{nd,p}$	$\sigma_{n,p}$
$z$	437	0.001	604	0.2	592	759
$R_x$	410	0.001	545	0.35	511	1199
$R_y$	410	0.001	545	0.35	511	1199

Table 3.2: Skew notch filters around 500 Hz, tuned with TFD.

The open-loop poles, marked with  $\blacktriangleleft$  and  $\star$  can also be observed in the figure at the intersections points. In the algorithm, the open-loop are distinguished from the closed-loop poles by inspection of the magnitude of  $\hat{D}(s_i)$ , see also (3.71). The open-loop poles that lie close to the imaginary axis, are the poles of the plant. One pole is observed at 517 Hz. At 500 Hz, there are two open-loop poles, which can be seen from the fact that two  $\hat{u}$ - and two  $\hat{v}$ -contours intersect at this point. This is marked with the  $\star$  symbol. The poles of the notch filters can also be observed in the figure. The imaginary part of the pole location, the damped eigen-frequency is  $f_{nd,p} = \sqrt{1 - \beta_{n,p}^2}$ , and the real part is  $\sigma_{n,p} = 2\pi\beta_{n,p}f_{n,p}$ . These values are listed in Table 3.2 as well. The multiplicity that is created by placing the notches for  $R_x$  and  $R_y$  at the same frequency is clearly visible. Observe that, according to (3.58) the angles between the contours at the point of intersection equal  $45^\circ$ .

To verify that the damping has indeed improved for the new tunings of the notch filters, time-domain experiments have been conducted. A 510 Hz sinusoidal force disturbance of 1 N with a length of 0.5 seconds is injected in the torsion direction whereas the response is measured at one of the corners of the wafer stage. The top part of Figure 3.16 shows the response for both the initial tunings of the notch filters (grey) and for the notch filters tuned with the information obtained from the TFD approach (black). It can be observed that the amplitude of the response during excitation ( $t < 0.5$  seconds) is reduced by more than a factor two using the TFD approach. Furthermore, the decay rate after the response is much faster for the TFD-based approach. The bottom part of Figure 3.16 shows the power spectrum of both responses for the free response, i.e.,  $0.5 < t < 0.7$  seconds. The response obtained with the initial tuning of the notch filters clearly shows peaks at 500 and 517 Hz, which coincide with the resonance frequencies of the plant around 500 Hz. The spectrum of the response obtained with the TFD-based approach does not show sharp peaks, as the closed-loop poles are heavily damped. The frequency content is increased between 500 and 600 Hz as this is where the closed-loop poles are located. As such, the results show that the TFD-based approach indeed leads to a very effective damping of the modes of this setup around 500 Hz.

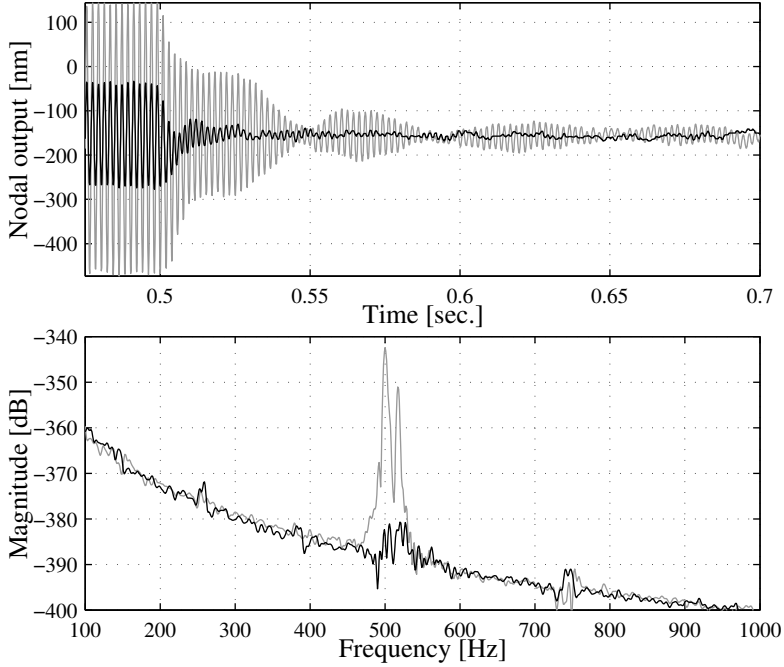


Figure 3.16: Time-domain response of the wafer stage and its frequency contents after injection of a 500 Hz sinusoidal disturbance. The tuning of the notch filters performed with TFD (black) results in a more damped response compared to the initial tuning (grey).

## 3.6 Conclusions

This chapter has presented a method to compute the closed-loop poles of multi-input multi-output systems from frequency response data, without the use of a parametric model of the system to be controlled. The method uses *transfer function data* (TFD), which is computed on a grid of points in the complex plane from the frequency response data using a Cauchy contour integral. The computation of TFD and its uncertainty bounds in the right half-plane is possible if the system is stable and strictly proper. TFD in the left half-plane can be computed as well, provided that the poles and zeros of the system possess a certain symmetry with respect to the imaginary axis.

TFD enables numeric evaluation of the determinant of the return difference ma-



trix from which the closed-loop poles can be computed. A numerically reliable method to estimate the closed-loop pole locations in between the grid points at which the TFD is computed is presented. The method is based on the estimation of the so-called  $u$ - and  $v$ -contours in the complex plane. It is shown that these contours intersect at certain angles at the pole locations depending on the multiplicity of the closed-loop poles. The open-loop poles and their multiplicity can also be estimated as the  $u$ - and  $v$ -contours also intersect at the open-loop pole locations. Discrimination between the open- and closed-loop poles is done based on the magnitude of the determinant.

Experiments that were conducted on a prototype wafer stage validate the results of the proposed method. Firstly, a root-locus for the torsion mode of the setup was drawn. The root-locus was validated by comparing the closed-loop poles obtained from TFD with the estimation of closed-loop poles from time-domain data. Secondly, it was shown that TFD can be used as a design tool that can aid the control engineer in the design of controllers by loop-shaping. The experiments show that TFD can be used to tune skew notch filters towards optimal damping factors of the closed-loop poles.

## Chapter 4

# Directionality of flexible modes

*A new method to design notch filters for MIMO motion control systems with flexible mechanical structures is proposed in this chapter. The method involves so-called directional notch filters that act only in the direction of the targeted resonant mode. As a result, only one SISO notch filter is required per mode to suppress a resonance throughout the MIMO system. Compared to the conventional approach where a notch filter is placed and tuned in each of the separate control loops, the new approach reduces the order of the controller significantly. The directional notch filter is computed using either the input or output mode shapes of the system. A new numerical optimization method to obtain these mode shapes from frequency response data is described. Experiments on a flexible beam setup are included to demonstrate the feasibility of the proposed method in practice.*

### 4.1 Introduction

Dealing with flexible dynamics of high-precision motion systems has become increasingly important due to increasing performance requirements for these systems. A clear example is given by wafer scanners in the semi-conductor industry. To achieve high accelerations in these scanners, a trend is towards lightweight mechanical designs. However, in general this results in a decrease in stiffness of these systems and causes the resonances of these systems to shift towards lower frequencies, thereby potentially affecting the stability of the system. This complex interaction between the mechanical design, the dynamics of the system, the actuation and sensor systems and the control design poses a challenging problem.

In industrial practice, high-precision multi-input-multi-output (MIMO) motion systems are generally controlled in a decentralized way (Butler, 2011; Van de Wal et al., 2002). To this end, MIMO motion systems are decomposed in single-input-single-output (SISO) systems by pre- and post-multiplying the plant with static decoupling matrices. As accurate frequency response data can be obtained at low costs for such systems, loop-shaping is used to design the SISO controllers (Steinbuch and Norg, 1998). The controllers usually contain notch filters to suppress high-frequency resonances that cause instability of the closed-loop system. However, at high frequencies the system is usually not decoupled. The reason for this is the interaction caused by the flexible dynamics of these systems. This means that the notch filters that are designed in each SISO loop separately to suppress the resonances that appear in that loop, do not guarantee that the complete MIMO system is stable. This is because the system is not decoupled at these frequencies.

Ideally, it is possible to decouple all modes and address each of them in separate SISO control loops by modal decoupling, as described in Inman (1984), and applied by, e.g., Schneiders et al. (2004); Friswell (2001); Anthonis and Ramon (1999). Modal decoupling exploits the mode shapes to compute static transformation matrices to decouple the modes. However, the number of modes that can be decoupled is limited by the number of actuators and sensors. Flexible structures have infinitely many modes such that perfect decoupling of all modes would require an infinite number of actuators and sensors.

The step towards dynamic decoupling matrices has been made to overcome this limitation, but with limited success only (Vaes, 2005; Chughtai et al., 2005). Using observers to estimate the modal states has also been studied extensively. In this field, independent modal space control (Meirovitch and Baruh, 1983) is the best known example. However, it is well known that these observers suffer from control and observation spillover of unmodelled modes, see Balas (1978). Despite this disadvantage, independent modal space control remains a topic of active research, especially in those cases where a sufficient number of sensors is available, see Inman (2001); Cazzulani et al. (2011); Resta et al. (2010) and the references therein.

Another disadvantage of dynamic decoupling and observer-based strategies is that they often require a MIMO model of the system to be controlled. Accurate MIMO models for high-precision motion systems are not readily available, see van de Wal et al. (2001, 2002).

In this chapter, an alternative method to deal with the resonances in flexible MIMO motion systems is described. The dynamics of a flexible structure can be described by its modal representation, see Gawronski (2004); Preumont (2011). In this representation, it is assumed that the transfer function of the system can be written as a summation of modes, each with a specific frequency, damping, and

mode shape. These mode shapes give the modes a strong directionality in the MIMO system. Since each mode has a specific input and output direction, the control of these modes should take this directionality into account.

Directionality is the main difference between SISO and MIMO systems (Skogestad and Postlethwaite, 2005). While it is often recognized that directions in MIMO systems are important, there are not many methods to design controllers that cope with this directionality, without resorting to full model-based control design methods. Boerlage et al. (2010) describe a method to design a controller that counteracts disturbances in the appropriate directions. Contrary to Boerlage et al. (2010), who focus on disturbance rejection, our method aims at using the directions of the flexible modes in the control design.

The directionality of the modes is utilized to design notch filters that have the correct directionality within the MIMO system. For this purpose, a SISO notch filter is distributed over the channels of the MIMO system according to the mode shape of the targeted resonant mode, creating a so-called *directional notch filter*. Conventionally, for each mode one notch filter per SISO loop is required to suppress the resonance in all channels of the system. A directional notch filter requires only one SISO notch filter such that the order of the controller is reduced and the design process is facilitated. Note that contrary to the available feedback, e.g., Hjalmarsson and Birkeland (1998); Hara et al. (1988) and feedforward methods, e.g., Bien and Xu (1998) that rely on the repetitive nature of the motion task, our approach is completely independent of the setpoint. The proposed approach aims at enhancement of the dynamics of the system rather than the suppression of (repetitive) disturbances.

In the conventional way of designing notch filters, i.e., independent design of a controller for each SISO loop, merely the stability of the SISO loops is considered. After the loop-shaping of the SISO loops, the stability of the MIMO system should be checked in view of the interaction between the loops. If the MIMO stability analysis shows that the system is unstable, it is in general not clear which SISO loop should be adjusted to stabilize the system. Adaptive notch filters as described in (Levin, 2011), are used for the automatic tuning of SISO notch filters. However, the multivariable nature of these systems is not taken into account. Another approach that is often used is sequential loop-closing, see Hovd and Skogestad (1994); Mayne (1973). Although this technique does consider the interaction between the loops, the order in which the loops are closed is arbitrary, and again it is not obvious which loop should be adjusted in case the performance of the system is unsatisfactory.

Design of the directional notch filters is done in view of MIMO stability, which guarantees the stability of the overall system. In this chapter, the characteristic loci (Maciejowski, 1989) are used to design the directional notch filters. Other

MIMO stability analysis methods could be used as well.

The transformation matrices are computed from the mode shapes of the modes that need to be suppressed. The mode shapes may be obtained from a parametric model of the system to be controlled, if such a model is available. However, as mentioned before, an accurate parametric model is often not available. Therefore we will reside to a data-based method to obtain the mode shapes. Many methods are known in modal analysis literature, see Reynders (2012) for an overview. However, these methods require that the number of inputs and outputs exceed the number of modes. Therefore, this chapter also describes a new method to obtain the mode shapes from the frequency response data directly.

In addition, experiments have been conducted on a prototype flexible motion system to validate the proposed concepts. Summarizing, the main contributions of this chapter are:

- a new method to design notch filters for MIMO systems,
- an algorithm to compute mode shapes from frequency response data,
- validation of the method by experiments.

This chapter is organized as follows. First, the necessary concepts of the modal description are discussed in Section 4.2. Next, conventional notch filter design is discussed in Section 4.3. Section 4.4 explains the concept of directional notch filtering and elaborates on the computation of directional notch filters. Experiments are presented in Section 4.5, followed by conclusions in Section 4.6.

## 4.2 Modal description

Flexible structures are characterized by internal deformations of a structure. The dynamics of these internal deformations can be described in *nodal* or *modal* coordinates. Nodal coordinates typically represent the position and velocity of each node in the structure. A large number of nodes is required to obtain an accurate description of the structure, which implies that accurate nodal models are generally of high order. To limit the model-order, the dynamics of flexible structures are often described using the modal representation, see e.g., Preumont (2011); Gawronski (2004). In this description, the deformation of a flexible structure is described in terms of a limited number of modes and mode shapes. These modes are mutually independent (assuming proportional damping), contrary to the nodal

coordinates, which simplifies the analysis. Several modal forms are possible, see Gawronski (2004). A modal description with state vector

$$\mathbf{x} = \begin{bmatrix} \mathbf{q}_m \\ \dot{\mathbf{q}}_m \end{bmatrix}, \quad (4.1)$$

is chosen, where  $\mathbf{q}_m$  represent the modal displacements and  $\dot{\mathbf{q}}_m$  the modal velocities. Both  $\mathbf{q}_m$  and  $\dot{\mathbf{q}}_m$  are vectors of length  $n_m$ , where  $n_m$  is the number of modes in the model. The  $2n_m$  equations of motion are given by

$$\begin{aligned} \dot{\mathbf{x}} &= \mathbf{A}\mathbf{x} + \mathbf{B}\mathbf{u} \\ \mathbf{y} &= \mathbf{C}\mathbf{x} + \mathbf{D}\mathbf{u}, \end{aligned} \quad (4.2)$$

with

$$\begin{aligned} \mathbf{A} &= \begin{bmatrix} \mathbf{0} & \mathbf{I}_n \\ \Omega^2 & -2\mathbf{Z}\Omega^2 \end{bmatrix}, & \mathbf{B} &= \begin{bmatrix} \mathbf{0} \\ \mathbf{B}_m \end{bmatrix}, \\ \mathbf{C} &= [\mathbf{C}_m \quad \mathbf{0}], & \mathbf{D} &= \mathbf{0}, \end{aligned} \quad (4.3)$$

where

$$\Omega = \text{diag}(\omega_1, \dots, \omega_{n_m}), \quad (4.4)$$

is the matrix that contains the eigenfrequencies  $\omega_i$  of the modes and where

$$\mathbf{Z} = \text{diag}(\zeta_1, \dots, \zeta_{n_m}), \quad (4.5)$$

is the matrix that contains the modal damping ratios  $\zeta_i$  of the modes. Consequently, the  $\mathbf{A}$  matrix is of dimension  $2n_m \times 2n_m$ .  $\mathbf{B}$  is  $2n_m \times n_u$ , with  $n_u$  the number of actuators. Since only force actuators are considered, the first  $n_m$  rows of  $\mathbf{B}$  are zero. The lower, non-zero part of  $\mathbf{B}$  is denoted with  $\mathbf{B}_m$  and is given by

$$\mathbf{B}_m = \begin{bmatrix} \mathbf{b}_{m1}^T \\ \mathbf{b}_{m2}^T \\ \vdots \\ \mathbf{b}_{mn_m}^T \end{bmatrix}. \quad (4.6)$$

Each row  $\mathbf{b}_{mi}^T$  contains the mode shape of mode  $i \in \{1, 2, \dots, n_m\}$  as being controlled at the  $n_u$  actuator locations, i.e., the *input mode shape* of mode  $i$ .  $\mathbf{C}$  has dimensions  $n_y \times 2n_m$ , with  $n_y$  the number of sensors. The last  $n_m$  columns of  $\mathbf{C}$  are equal to zero since only position sensors are considered. The first  $n_m$  non-zero columns are denoted with  $\mathbf{C}_m$  and are given by

$$\mathbf{C}_m = [\mathbf{c}_{m1} \quad \mathbf{c}_{m2} \quad \cdots \quad \mathbf{c}_{mn_m}]. \quad (4.7)$$

Each column  $\mathbf{c}_{mi}$  contains the mode shape of mode  $i$  as observed at the  $n_y$  sensor locations.  $\mathbf{c}_{mi}$  will further be referred to as the *output mode shape* of mode  $i$ .

The state space system (4.2) contains  $n_m$  independent second-order differential equations, one for each mode. This can be seen by substitution of (4.3) in (4.2), which gives

$$\mathbf{y}(s) = \mathbf{H}(s)\mathbf{u}(s), \quad (4.8)$$

where

$$\begin{aligned} \mathbf{H}(s) &= \mathbf{C}(s\mathbf{I}_{2n_m} - \mathbf{A})^{-1}\mathbf{B} \\ &= \mathbf{C}_m(\mathbf{\Omega}^2 + s^2\mathbf{I}_{n_m} + 2s\mathbf{Z}\mathbf{\Omega})^{-1}\mathbf{B}_m \\ &= \sum_{i=1}^{n_m} \frac{\mathbf{c}_{mi}\mathbf{b}_{mi}^T}{s^2 + 2s\zeta_i\omega_i + \omega_i^2}, \end{aligned} \quad (4.9)$$

where the special structure of the  $\mathbf{B}$  and  $\mathbf{C}$  matrices and the fact that  $\mathbf{\Omega}$  and  $\mathbf{Z}$  are diagonal is used. Equation (4.9) shows that the modes are independent, the transfer from inputs  $\mathbf{u}$  to outputs  $\mathbf{y}$  is a summation of individual modal contributions. Furthermore, it can be observed from (4.9) that each mode has a very specific directionality in the MIMO system, which is completely determined by the numerator terms in (4.9). For each mode, the denominator is a scalar valued function. This means that the directionality is determined by the constant matrix  $\mathbf{c}_{mi}\mathbf{b}_{mi}^T$  in the numerator. Note that this matrix has rank one as it is build up from a multiplication of a column vector with a row vector. These vectors, the input and output mode shape, determine the directionality of each mode. This directionality will be utilized in the method proposed in the remainder of this chapter.

### 4.3 Conventional notch filters

Multi-input-multi-output (MIMO) motion systems are often controlled in a decentralized way. Conventionally, static decoupling matrices  $\mathbf{T}_y$  and  $\mathbf{T}_u$  are used to transform the inputs and outputs of the system  $\mathbf{H}(s)$  to a new set of coordinates according to

$$\mathbf{H}_{dec}(s) = \mathbf{T}_y\mathbf{H}(s)\mathbf{T}_u, \quad (4.10)$$

where  $\mathbf{H}_{dec}(s)$  represents the decoupled system. There are several advantages to this approach. Firstly, the transformation matrices are chosen in such a way that they minimize the coupling between the subsequent channels, which makes

it possible to apply single-input-single-output (SISO) control design techniques to control the MIMO system. This simplifies the control design significantly. Secondly, the new coordinates can be chosen in such a way that they are aligned with the performance variables. This simplifies the setpoint design and performance assessment.

Motion systems are often decoupled in their rigid-body modes, since these modes enable the system to perform the motion tasks for which it is designed. For example, a 6 degrees-of-freedom (DOF) motion system will have six rigid-body modes for which  $\omega_i = 0$  for  $i \leq 6$ , see (4.9). The system will be decoupled in these modes such that a controller can be designed for each DOF separately. However, every motion system has a finite stiffness, which means that internal deformations will occur during the motion task due to the non-rigid-body, or flexible, modes of the system. In the example of the 6-DOF motion system this means that in (4.9)  $\omega_i \neq 0$  for  $i > 6$ .

Lightweight motion systems are often equipped with more sensors and actuators than rigid-body modes, to increase control authority over the internal deformations of the system. This is sometimes referred to as *overactuation* and gives more freedom in the selection of the decoupling matrices. Moreover, it enables *modal decoupling* where besides the rigid-body modes a limited number of flexible modes are decoupled as well. However, the number of modes that can be controlled explicitly is limited by the number of actuators and sensors in the system. A flexible structure is an infinite dimensional system having infinitely many modes such that in principle it is not possible to decouple all modes.

The remaining modes, which are not decoupled, will be visible to some extent in the transfer functions contained in  $\mathbf{H}_{dec}(s)$  in (4.10) depending on their mode shapes. The modes that affect closed-loop stability are suppressed using loop-shaping notch filters in the SISO loops. This, however, poses the following problem. Firstly, there is no guarantee that the MIMO system is stable when all SISO loops are designed to be stable, since the system is generally not decoupled at the frequencies of the resonances. Therefore, MIMO stability has to be checked afterwards. Secondly, should the MIMO system no longer satisfy the required stability properties, it is no straightforward task to determine in which loop a notch filter should be adjusted as to ensure MIMO stability altogether. Therefore, a different approach is needed.

## 4.4 Directional notch filters

The directionality of the modes can be utilized to design notch filters that have the correct directionality in the MIMO system. We call this *directional notch*



*filtering*. The idea is depicted in Figure 4.1 for mode  $i$ . The MIMO system  $\mathbf{H}(s)$  is controlled in a decentralized way by diagonal controller  $\mathbf{C}(s)$ , where the decoupling is achieved by the input decoupling matrix  $\mathbf{T}_u$  and output decoupling matrix  $\mathbf{T}_y$ . To this standard decentralized control loop, a directional notch is added at the plant input to target mode  $i$  of the system. The directional notch filter consists of two static transformation matrices  $\mathbf{T}_{in,i}$  and  $\mathbf{T}_{in,i}^{-1}$  and a matrix  $\mathbf{N}_i(s)$  that contains a notch filter at one of its entries.

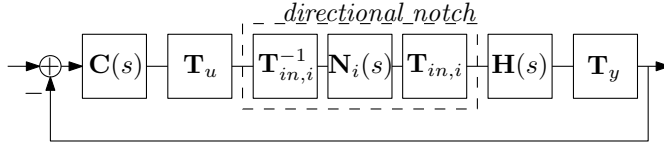


Figure 4.1: Feedback loop with directional notch filter.

#### 4.4.1 Directional notch filtering concept

The transformation matrix  $\mathbf{T}_{in,i}$  in Figure 4.1 transforms the input directions of the plant such that the input direction of mode  $i$  is isolated from the other input directions. This is achieved by the  $n_u \times n_u$  matrix

$$\mathbf{T}_{in,i} = [\mathbf{b}_{mi} \quad \text{Ker}(\mathbf{b}_{mi}^T)], \quad (4.11)$$

which consists of the input mode shape  $\mathbf{b}_{mi}$  of mode  $i$  and its kernel. The kernel of  $\mathbf{b}_{mi}^T$  contains the  $n_u - 1$  vectors that are perpendicular to the input mode shape of mode  $i$ . In this way,  $\mathbf{T}_{in,i}$  always has full rank, such that the inverse transformation matrix  $\mathbf{T}_{in,i}^{-1}$  exists. The transformation matrix  $\mathbf{T}_{in,i}$  combined with the input matrix  $\mathbf{B}_m$  of (4.3), yields

$$\mathbf{B}_m \mathbf{T}_{in,i} = \begin{bmatrix} \mathbf{b}_{m1}^T \\ \vdots \\ \mathbf{b}_{mi}^T \\ \vdots \\ \mathbf{b}_{mn}^T \end{bmatrix} [\mathbf{b}_{mi} \quad \text{Ker}(\mathbf{b}_{mi}^T)] = \begin{bmatrix} * & * & \cdots & * \\ \vdots & \vdots & & \vdots \\ * & * & \cdots & * \\ * & 0 & \cdots & 0 \\ * & * & \cdots & * \\ \vdots & \vdots & & \vdots \\ * & * & \cdots & * \end{bmatrix}. \quad (4.12)$$

Since the  $i^{th}$  row is zero, except for the first element, mode  $i$  can only be transferred through the first channel of the transfer function  $\mathbf{H}(s)\mathbf{T}_{in,i}$ . Thus, the transformation makes the  $i^{th}$  mode uncontrollable for all inputs except for the first input.

In this way, the resonance associated with this mode can be suppressed with one SISO notch filter in the first input channel. The diagonal notch filter for the transformed system is therefore given by

$$\mathbf{N}_i(s) = \begin{bmatrix} N_i(s) & \mathbf{0} \\ \mathbf{0} & \mathbf{I}_{n_u-1} \end{bmatrix}, \quad (4.13)$$

where

$$N_i(s) = \frac{s^2 + 2s\beta_{Ni,n}\omega_{Ni,n} + \omega_{Ni,n}^2}{s^2 + 2s\beta_{Ni,d}\omega_{Ni,d} + \omega_{Ni,d}^2}, \quad (4.14)$$

with  $\beta_{Ni,n}$ ,  $\beta_{Ni,d}$  and  $\omega_{Ni,n}$ ,  $\omega_{Ni,d}$  respectively the damping ratios and frequencies of the notch filter that are tuned for mode  $i$  as will be described in the next section. The other channels are unchanged, hence the identity matrix in (4.13). In order to control the system in the original directions, the inverse of the transformation matrix, i.e.,  $\mathbf{T}_{in,i}^{-1}$ , is added after notch filtering. The open-loop  $\mathbf{L}(s)$  with the directional notch filter is thus given by

$$\mathbf{L}(s) = \mathbf{T}_y \mathbf{H}(s) \mathbf{T}_{in,i} \mathbf{N}_i(s) \mathbf{T}_{in,i}^{-1} \mathbf{T}_u \mathbf{C}(s). \quad (4.15)$$

The directional notch performs a local adjustment of the frequency response of the system. Just as a conventional notch, it is local in terms of frequency interval because the notch is only affecting a narrow frequency band. However, the directional notch is also local in terms of direction; it only acts in the direction of the mode shape of the targeted resonance. Note that the approach can be applied to multiple modes by adding multiple directional notches in series. In that case the open-loop becomes

$$\mathbf{L}(s) = \mathbf{T}_y \mathbf{H}(s) \prod_i (\mathbf{T}_{in,i} \mathbf{N}_i(s) \mathbf{T}_{in,i}^{-1}) \mathbf{T}_u \mathbf{C}(s), \quad (4.16)$$

where  $i$  runs over all targeted modes.

Motion systems often require a non-constant decoupling, for example when the performance location of the system changes over time. In that case the decoupling will also be required to change over time, i.e., to become position dependent. As a result, conventional notch filters either have to be chosen robustly, at the cost of performance, or different notch filters have to be used at different points of interest on the structure, which comes at the cost of controller complexity. Since the directional notch is placed directly before the plant, it is independent of the decoupling of the system. This means that it is neither necessary to design the notches very robustly, nor to reside to different notches at different performance locations. Directional notch filtering can be seen as an enhancement of the plant, independent of the controllers for the decoupled degrees-of-freedom. The plant

with directional notch filters can be controlled at a higher bandwidth compared to the plant without directional notch filters. However, the achievable performance of the overall system still depends on the limitations of this enhanced system. These limitations are the quality of the decoupling, fundamental performance limits such as right-half-plane zeros, available phase lead, to name but a few.

In the previous analysis, the directional notches were applied to the inputs of the plant. They can also be applied to the output of the plant, however. In that case the  $n_y \times n_y$  transformation matrix

$$\mathbf{T}_{out,i} = [\mathbf{c}_{mi} \quad \text{Ker}(\mathbf{c}_{mi}^T)]^T, \quad (4.17)$$

has to be used, which is determined by the output mode shape  $\mathbf{c}_{mi}$  of mode  $i$ . In terms of the outputs of (4.3), the transformation at the output combines the output matrix  $\mathbf{C}_m$ , giving

$$\begin{aligned} \mathbf{T}_{out,i} \mathbf{C}_m &= \begin{bmatrix} \mathbf{c}_{mi}^T \\ \text{Ker}(\mathbf{c}_{mi}^T)^T \end{bmatrix} [\mathbf{c}_{m1} \quad \cdots \quad \mathbf{c}_{mi} \quad \cdots \quad \mathbf{c}_{mn}] \\ &= \begin{bmatrix} * & \cdots & * & * & * & \cdots & * \\ * & \cdots & * & 0 & * & \cdots & * \\ \vdots & & \vdots & \vdots & \vdots & & \vdots \\ * & \cdots & * & 0 & * & \cdots & * \end{bmatrix}. \end{aligned} \quad (4.18)$$

That is, the  $i^{th}$  mode becomes unobservable in all output channels except for the first one. Again it is possible to suppress this resonance with a single SISO notch in the first output channel. The open-loop with directional notch filter for mode  $i$  at the output is defined as

$$\mathbf{L}(s) = \mathbf{T}_y \mathbf{T}_{out,i}^{-1} \mathbf{N}_i(s) \mathbf{T}_{out,i} \mathbf{H}(s) \mathbf{T}_u \mathbf{C}(s). \quad (4.19)$$

Addressing multiple modes is done by adding extra directional notch filters in series to obtain

$$\mathbf{L}(s) = \mathbf{T}_y \prod_i (\mathbf{T}_{out,i}^{-1} \mathbf{N}_i(s) \mathbf{T}_{out,i}) \mathbf{H}(s) \mathbf{T}_u \mathbf{C}(s). \quad (4.20)$$

#### 4.4.2 Design of the directional notch filter

As discussed in Section 4.3, the conventional loop-shaping approach is to place SISO notch filters in each decentralized SISO control loop. However, the non-decoupled modes will appear in all transfer functions of the MIMO system, so several SISO loops will generally contain notch filters for one and the same resonant

mode. This unnecessarily increases the order of the controller. Furthermore, the SISO design gives no guarantees regarding MIMO stability.

Design of the directional notch filter will be shown to be straightforward. The transformation matrices  $\mathbf{T}_{in,i}$  from (4.11) (or  $\mathbf{T}_{out,i}$  from (4.17) in the case that the directional notch is used at the plant output) ensures that the directional notch filter acts in the proper direction of the MIMO system. Not only is the order of the controller reduced, but also the design process is facilitated in this way. Namely, per mode only a single SISO notch filter (4.14) has to be tuned. This can be done in combination with a MIMO stability analysis method such as the characteristic loci or the MIMO Nyquist plot. The characteristic loci will be used in this chapter. The overall control design procedure can be described as follows:

1. decouple the system with static decoupling matrices  $\mathbf{T}_u$  and  $\mathbf{T}_y$ ,
2. design SISO controllers for the decoupled system  $\mathbf{H}_{dec}(s)$  while disregarding the high-frequency resonances,
3. draw the characteristic loci and assess which resonances need notch filtering,
4. compute directional notch filters for these resonances,
5. design the SISO notch filters  $N_i(s)$  using characteristic loci.

In this chapter, the need for notch filters (step 3) is determined on the basis of the characteristic loci plot. The SISO notch filters are tuned (step 5) such that the characteristic loci lie outside a circle with radius 0.5 around the -1 point, thus ensuring a design with sufficient robustness margins. Of course, other stability measures, design methods, and/or robustness criteria can be chosen.

### 4.4.3 Obtaining the mode shapes

One aspect that has not been discussed so far is how to obtain the mode shapes that are used to construct the  $\mathbf{T}_{in,i}$  or  $\mathbf{T}_{out,i}$  matrices in (4.11) and (4.17). One approach is to derive a modal model using Finite Element Modeling (FEM). For motion control purposes, however, FEM models are either expensive or not accurate enough. Alternatively, (modal) identification techniques can be used, see Brown et al. (2011) for a recent overview of this extensively studied field of research. The disadvantage of modal identification techniques is that they require that the number of sensors exceeds the number of modes, which is generally not the case in our field of application.

In this chapter, an alternative, data-based approach is used to find the input or output mode shapes needed to construct  $\mathbf{T}_{in,i}$  or  $\mathbf{T}_{out,i}$  in (4.11) and (4.17) respectively. Since only the mode shape and not a complete modal model is required, a relatively straightforward approach can be used. The idea will be explained for the case that the directional notch is placed at the input side of the system. The derivation is similar for the case when the directional notch is placed at the output side of the system.

The idea is to find the input mode shape  $\mathbf{b}_{mi}$ . A way to do so is by inspecting whether the corresponding matrix  $\mathbf{T}_{in,i}$  causes mode  $i$  to be affected by the first input only, recall the definition in (4.12). The frequency response can be used to verify this. If  $\mathbf{T}_{in,i}$  is in the desired direction, the resonance peak of that mode will only appear in the first column of  $\mathbf{H}\mathbf{T}_{in,i}$ . For this purpose, the value of the transformed system at the resonance frequency  $\omega_i$  of mode  $i$  will be used. This is denoted with

$$\mathbf{M}(j\omega_i) = \mathbf{H}(j\omega_i)\mathbf{T}_{in,i}, \quad (4.21)$$

while each of the entries of  $\mathbf{M}(j\omega_i)$  with dimension  $n_y$  times  $n_u$  are denoted with  $m_{kl}$ . The cost function  $J$  for this optimization can then be formulated as

$$J = \min_{\mathbf{b}_{mi}} \sum_{k=1}^{n_y} \sum_{l=2}^{n_u} |m_{kl}|. \quad (4.22)$$

The cost function  $J$  represents a summation of all elements in  $\mathbf{M}(j\omega_i)$ , except for the first column. In this way the cost function is minimal if the resonance peak of mode  $i$  is only visible in the first column of  $\mathbf{H}(j\omega)\mathbf{T}_{in,i}$ .

Stating the problem of finding the mode shape in this way calls for numeric optimization techniques to find the minimum of (4.22). This requires a proper parametrization of  $\mathbf{b}_{mi}$ . Since only the direction and not the magnitude of  $\mathbf{b}_{mi}$  is important,  $\mathbf{b}_{mi}$  can be parametrized using  $n_u - 1$  angles (Vaes, 2005) giving

$$\mathbf{b}_{mi} = \begin{bmatrix} \prod_{k=1}^{n_u-1} \cos(\theta_k) \\ \sin(\theta_{n_u-1}) \prod_{k=1}^{n_u-2} \cos(\theta_k) \\ \sin(\theta_{n_u-2}) \prod_{k=1}^{n_u-3} \cos(\theta_k) \\ \vdots \\ \sin(\theta_2) \cos(\theta_1) \\ \sin(\theta_1) \end{bmatrix}, \quad (4.23)$$

which saves one optimization parameter, but more important, yields the optimization bounded as all angles range between  $-\pi$  and  $\pi$ . With this parametrization, (4.22) represents a cheap optimization problem, since the number of parameters is

only  $n_u - 1$ . The cost function is also relatively simple and numerically not computationally demanding because it does not contain very large matrices. However, the optimization is non-linear and convexity properties are likely to be lost, which is why we reside to genetic algorithms to solve the optimization problem.

Whether the computation of the mode shapes is based on a parametric model of the system or on optimization routines, the stability analysis will always be performed completely data-based. Computation of the characteristic loci or the MIMO Nyquist plot require only frequency response data of the system. This means that errors in the approximation of the mode shapes, will be visible in the MIMO stability analysis.

## 4.5 Results

### 4.5.1 Flexible beam setup

To validate the approach, experiments have been conducted on a prototype lightweight motion system. The system, shown in Figure 4.2, consists of a flexible beam with a collocated set of three actuators and three sensors. This beam setup approximates the dynamics such as found in flexible lightweight motion systems like lithographic machines. The dynamics of these systems are characterized by a combination of rigid-body modes, which are the required degrees-of-freedom, and unwanted flexible modes that can affect the stability and limit performance of the closed-loop system. The beam in Figure 4.2 can only move in  $y$ -direction and rotate about the  $z$ -axis, the other rigid-body degrees-of-freedom are fixed. Internal deformations of the beam are mainly in the  $y$ -direction since this is the direction of the beam that has the lowest stiffness.

For the experiments, only the outer two actuators (A1, A3) and sensors (S1, S3) of the setup are used. Due to symmetry, all mode shapes are either symmetric or antisymmetric with respect to the center of the beam. This means that decoupling towards the center would decouple all flexible modes as well. As this is an exceptional situation, the decoupling is chosen towards a more challenging point between S1 and S2. Namely, the point where the coordinate system is drawn in Figure 4.2. In this way, the non-rigid-body modes will be coupled in the (rigid-body) decoupled system. The decoupling matrices are given by

$$\mathbf{T}_y = \begin{bmatrix} 1 & 1 \\ 3 & -1 \end{bmatrix}, \quad \mathbf{T}_u = \mathbf{T}_y^{-1}. \quad (4.24)$$

The frequency response of the decoupled system is shown in Figure 4.3. The goal is

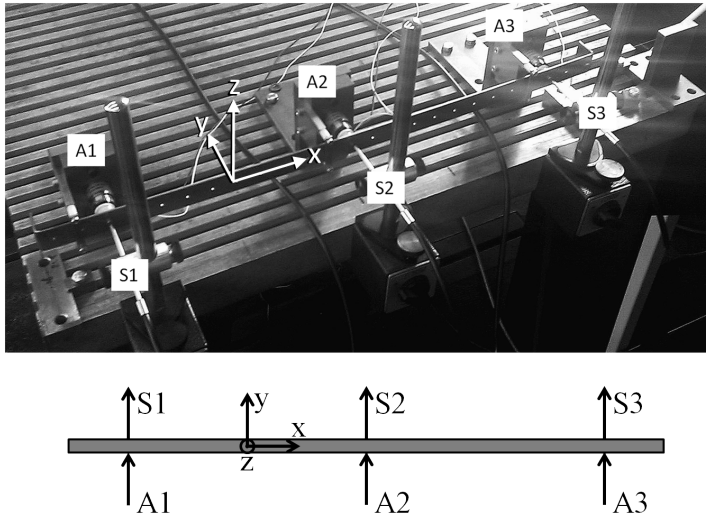


Figure 4.2: Photo and schematic representation of the beam setup. The system has three actuators  $A1$ - $A3$  and sensors  $S1$ - $S3$ .

to control the rigid-body degrees-of-freedom with a bandwidth of 50 Hz. From the relative gain array (RGA), plotted in Figure 4.4, it can be observed that around the target bandwidth frequency, the decoupling is sufficiently good. The diagonal terms are around 0 dB at 50 Hz, while the off-diagonal terms are much smaller ( $-30$  dB). This favors decentralized control.

#### 4.5.2 Decentralized Control

Two SISO controllers are designed using conventional loop-shaping techniques on the two SISO open-loops, see Figure 4.5. The controllers consist of a lead-filter, a low-pass filter, and a limited set of notch filters. The controller for the first loop has a notch filter at 179 Hz, while the second loop has notch filters at 99 Hz and 286.5 Hz. These notch filters are tuned such that the SISO Nyquist curves lie outside a circle with radius 0.5 around the Nyquist stability point at  $(-1,0)$ , see Figure 4.6. This guarantees that magnification of the corresponding sensitivity function  $\leq 6$  dB and the amplitude margins  $\geq 6$  dB. However, Figure 4.4 shows that the system is not decoupled at high frequencies. This means that a MIMO stability test is required to check stability of the MIMO system. For this purpose, the characteristic loci are plotted in Figure 4.7.

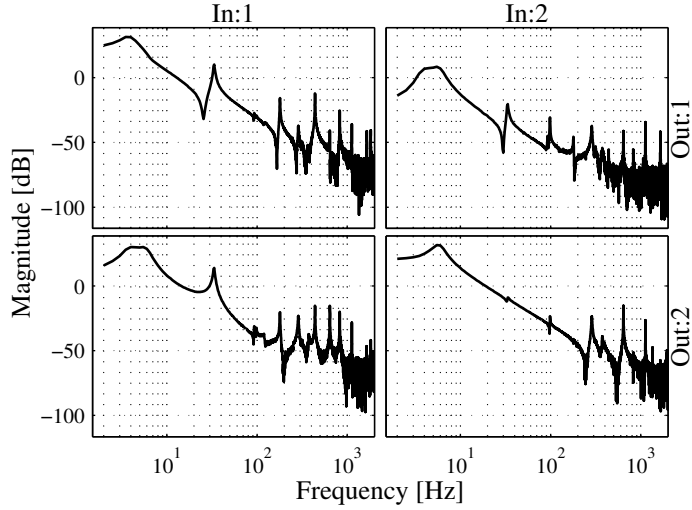


Figure 4.3: Measured frequency response of the decoupled beam setup.

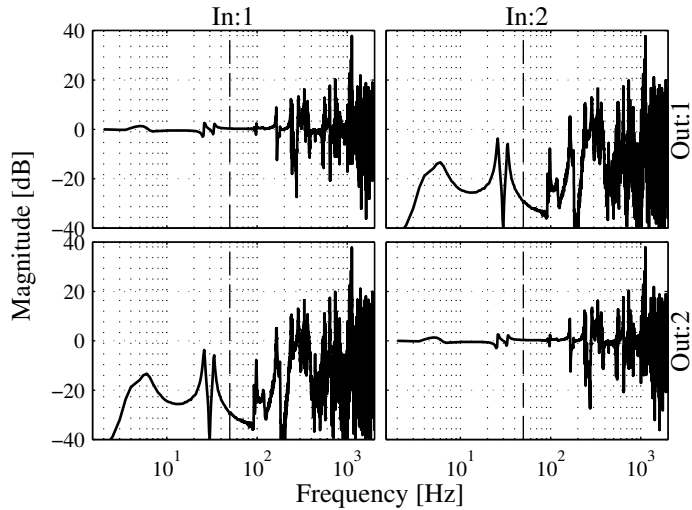


Figure 4.4: Relative gain array of the decoupled beam setup. Decoupling is sufficiently obtained around the desired bandwidth ( 50 Hz), but lost at high frequencies.



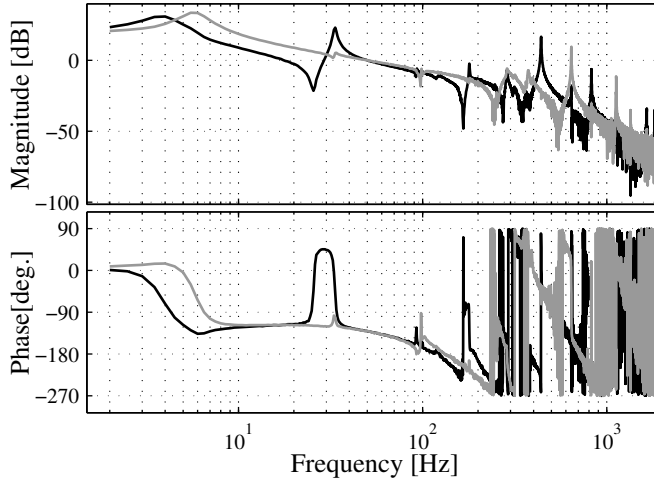


Figure 4.5: Open-loops of the first (black) and second (grey) loop of the setup for conventional decentralized control.

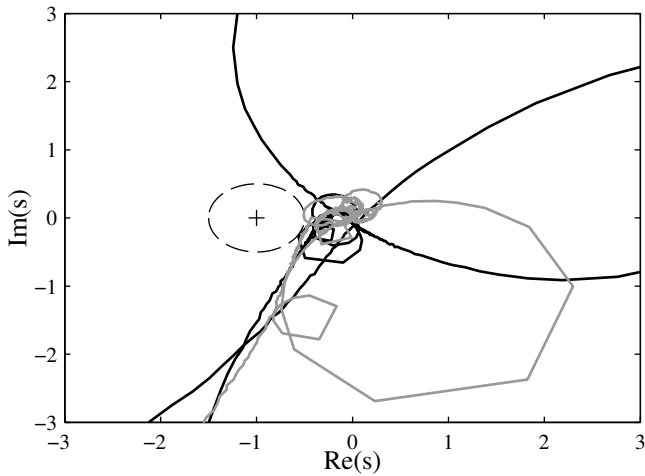


Figure 4.6: Nyquist plots of the first (black) and second (grey) loop of the setup for conventional decentralized control.

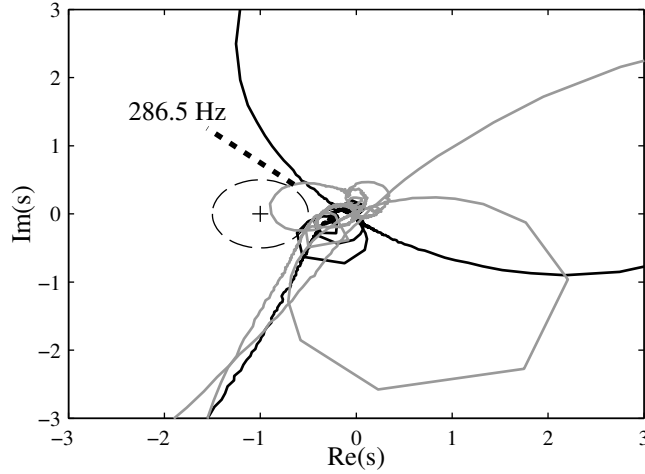


Figure 4.7: Characteristic loci of the open-loop of the setup for conventional decentralized control.

The characteristic loci violate the previous circle constraint, showing that the stability margins are not as good as they appeared from SISO analysis. It can be concluded that the notch filter at 286.5 Hz is not applied in the proper direction of the MIMO system. This could be expected, since the system is not decoupled at this frequency. One solution might be to add a notch filter at 286.5 Hz in the first loop as well. However, this increases the order of the controller because it adds two states to the controller and it is not clear how to tune this notch filter.

### 4.5.3 Directional Notch filtering

As conventional loop-shaping control design cannot deal properly with the coupled dynamics of the high-frequency resonances, the directional notch filtering concept is applied next. Firstly, the SISO controllers are designed while disregarding high-frequency resonances. For the beam setup, these SISO controllers consist of the same lead filter and a low-pass filter as used in the conventional design approach, yet without the notch filters. The characteristic loci of the open-loop are depicted in Figure 4.8. Three resonances at 99, 179 and 286.5 Hz lie within the circle around the Nyquist stability point. Directional notch filters, placed at the input of the plant, will be applied to these three modes. The modes will be numbered mode 1,

2 and 3.

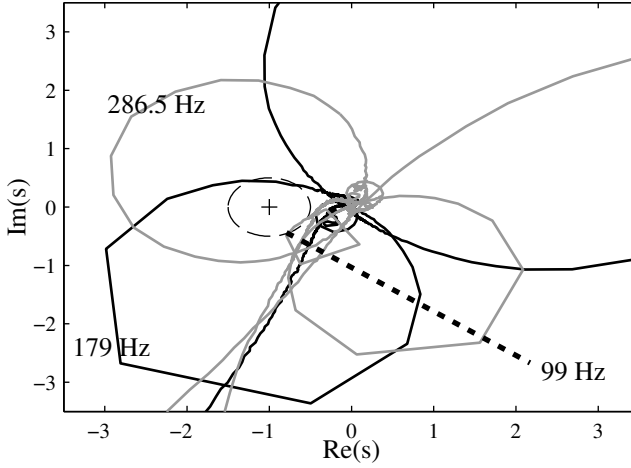


Figure 4.8: Characteristic loci of the open-loop of the setup with lead and low-pass filter, without notches.

The input mode shapes  $\mathbf{b}_{m1}$ ,  $\mathbf{b}_{m2}$  and  $\mathbf{b}_{m3}$  of each mode are determined first, using the optimization method as described in Section 4.4.3. For this  $2 \times 2$  system, the direction of each mode  $i$  can be parametrized with one angle only. Thus in this case

$$\mathbf{b}_{mi} = \begin{bmatrix} \cos(\theta_i) \\ \sin(\theta_i) \end{bmatrix}, \quad (4.25)$$

where  $i \in \{1, 2, 3\}$ . The goal of the optimization is to find the value of  $\theta_i$  for which the resonance peak of mode  $i$  disappears from the second column of the frequency response plot of  $\mathbf{H}(j\omega)\mathbf{T}_{in,i}$ . Three optimizations with a genetic algorithm are conducted with an initial population of 100 over 20 generations, which take less than a second to run on a normal pc. The result of the optimization is that

$$\begin{aligned} \theta_1 &= -19.63^\circ \\ \theta_2 &= 48.78^\circ \\ \theta_3 &= -45.56^\circ. \end{aligned} \quad (4.26)$$

These angles are used to compute the transformation matrices  $\mathbf{T}_{in,1}$ ,  $\mathbf{T}_{in,2}$  and  $\mathbf{T}_{in,3}$  for each of the three directional notches that are used for this system. For

each mode, it is verified that the resonance peak indeed disappears from the second column of  $\mathbf{H}(j\omega)\mathbf{T}_{in,i}$ . In Figure 4.9 this is shown for mode 2. While the resonance at 298 Hz was visible in all transfers of the original system, the transformed system  $\mathbf{H}(j\omega)\mathbf{T}_{in,2}$  no longer has the resonance in the second column of the frequency response matrix. This means that, at that point in the feedback loop, the system is decoupled with respect to mode 2 such that a single SISO notch filter in the first input channel is sufficient to remove this mode from the MIMO system entirely.

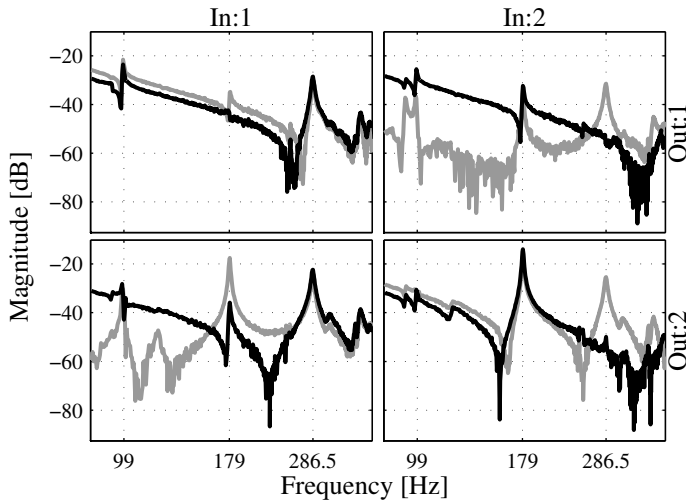


Figure 4.9: The system  $\mathbf{H}(j\omega)\mathbf{T}_{in,i}$  (black) does not show the mode at 286.5 Hz in the second column. The original plant  $\mathbf{H}(j\omega)$  is shown in grey.

Now that the direction of each mode is known, the next step is to tune the three SISO notch filters  $N_i$  in (4.13) and (4.14) such that the characteristic loci from Figure 4.8 lie outside the circle around the Nyquist stability point. Figure 4.10 shows the characteristic loci of the system with the tuned directional notches. The MIMO open-loop plots for the conventional case and the directional notch filtering case are compared around the resonance frequencies of the modes, see Figure 4.11. In the figure, it can be observed that the resonance peaks in the off-diagonal terms are suppressed much better with the directional notches compared to the conventionally tuned notches.

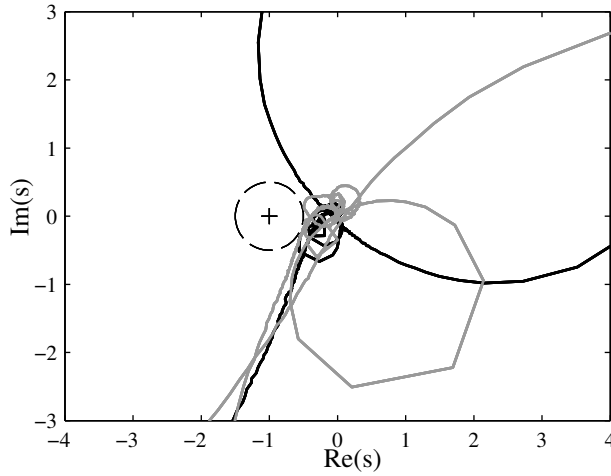


Figure 4.10: Characteristic loci of the open-loop with lead and low-pass filter, with directional notches.

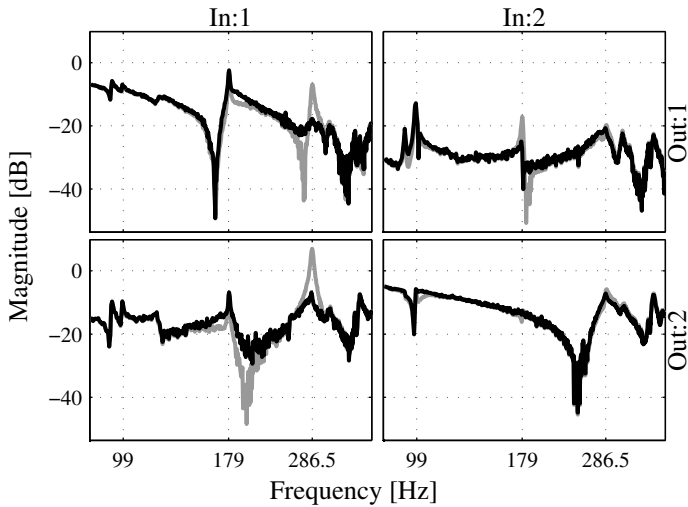


Figure 4.11: Open-loop for conventional decentralized control (grey) and directional notch filtering approach (black).

#### 4.5.4 Time-domain results

Time-domain results have been obtained from the beam setup for both the conventional loop-shaping controller and the controller with directional notches. Measured MIMO impulse responses are displayed in Figure 4.12. Although both controllers are stable, the conventional controller design clearly shows a more oscillatory behaviour. The amplitude of the oscillations is a factor 2 to 3 larger. The cumulative power spectral density plot of Figure 4.13 reveals that this is mainly induced by the resonant mode at 286.5 Hz that is visible in the response of the conventionally controlled system. This could have been expected as the characteristic loci for the conventional controller lie too close to the Nyquist stability point, recall Figure 4.7.

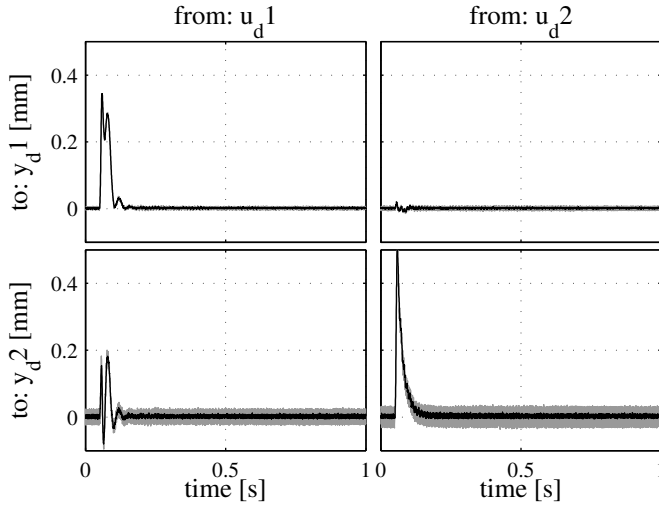


Figure 4.12: Impulse response for conventional decentralized control (grey) and directional notch filtering approach (black).

## 4.6 Conclusions

Directional notch filters provide a new way of loop-shaping notch filters for MIMO motion systems with flexible structures. The mode shapes of the target resonant modes can be used to compute directional notch filters that operate in the correct

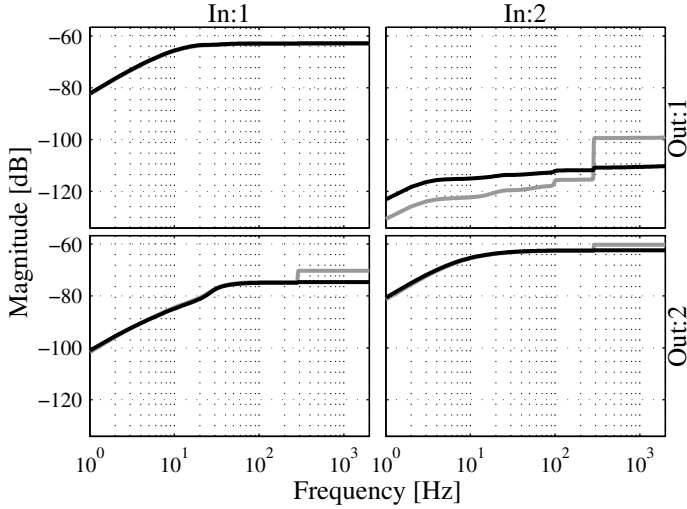


Figure 4.13: Cumulative power spectral density plot for conventional decentralized control (grey) and directional notch filtering approach (black).

direction of the MIMO system. The mode shapes of the system are obtained in a data-based way from the measured frequency responses of the system. Only one SISO notch filter is required per mode to suppress a resonance in the MIMO system. As a result, the new approach reduces the order of the controller compared to conventional multiloop SISO control. The method allows for tuning of the directional notch filters in view of MIMO stability, thereby accounting for the coupling in the system.

Experiments on a prototype lightweight motion system show the feasibility of the approach in practice. Three modes of the beam setup that affect the stability of the closed-loop system are suppressed successfully using directional notches. Compared to conventional multiloop SISO loop-shaping, the results show that suppression of the flexible modes is improved when directional notch filters are applied. This is because directional notch filters account for the directionality of the resonances. Conventional SISO loop-shaping notch filters are not suitable for this, as the system is not decoupled at the frequencies of the resonances.

## Chapter 5

# Conclusions and recommendations

**T**he main conclusions of this thesis are discussed and suggestions for further research based on the presented methods are given in this chapter.

### 5.1 Conclusions

The frequency response data-based control design methods proposed in this thesis may form a key contribution towards accurate and fast positioning in the next generation of high-precision motion systems. Flexible dynamics will become increasingly important due to the increased performance requirements in terms of speed and accuracy. Conventional control design methods are not automatically suited to control these flexible dynamics. Advanced model-based control design techniques are available that could deal with flexible dynamics but these require a parametric model, which is often not available or insufficiently accurate for high-precision motion systems. This thesis describes methods to address the flexible dynamics, without the need for a parametric model of the system to be controlled. The conclusions are divided in two parts, which are discussed in the following two sections.

#### 5.1.1 Damping of flexible modes

It is concluded that the closed-loop pole locations can be incorporated in the control design, without the need for a parametric model of the system to be controlled.



Knowledge of the closed-loop pole locations is important in order to improve the damping properties of the flexible modes. Conventionally, however, the closed-loop poles can only be computed from a parametric model. Fortunately, highly accurate frequency response measurements can be obtained at low cost for high-precision motion systems. These can be used to design controllers with high bandwidths and good disturbance rejection and noise filtering properties. However, the frequency-domain does not provide direct information on the closed-loop transient response and therefore the damping properties of the closed-loop poles remains unknown. The proposed method bridges the gap between data-based and model-based control design methods in the sense that the closed-loop pole locations are obtained without a parametric model of the system to be controlled.

It is shown that transfer function data (TFD) can be obtained accurately from measured frequency response data. The computation of TFD enables the computation of the closed-loop poles without the use of a parametric model. For SISO systems, a root-locus can be drawn from the data, which enables selection of the controller parameters that give the largest damping of the flexible modes. By computing the determinant of the return difference matrix from the TFD, the computation of closed-loop poles can also be performed for MIMO systems. Furthermore, the multiplicity of the closed-loop poles can be obtained from the TFD by analysing so-called  $u$ - and  $v$ -contours in the complex plane.

The proposed methods are readily applicable in practice, which is demonstrated by means of experiments on two different setups. It is shown that the damping of a benchmark two-mass motion system can be optimized using TFD by computing a data-based root-locus. Furthermore, the approach is successfully applied to a prototype wafer stage. A comparison between the closed-loop poles computed from TFD and time domain experiments shows that the closed-loop poles are accurately computed. It is also demonstrated that the closed-loop pole locations obtained from TFD can be incorporated in a loop-shaping control design with the aim to optimize the damping of a number of closely spaced flexible modes of the wafer stage.

### 5.1.2 Directionality of flexible modes

It is concluded that the directionality of the flexible modes can be incorporated in the control design, without the need for a parametric model of the system to be controlled. The directionality of a flexible mode in a MIMO system is determined solely by its mode shape. As high-precision motion systems typically have a large number of modes, a large number of directions manifests itself in these systems. Decoupling all flexible modes would require a large number of actuators and sensors, which increases the costs and complexity of these systems

and might be infeasible due to space limitations. Note that these systems are typically decoupled in a limited number of directions, usually only the rigid-body directions of motion. As a result, the flexible modes will appear in many of the decoupled transfer functions. Conventionally, these flexible modes are suppressed using SISO notch filters in each of the decoupled control loops.

In this thesis it is shown that a flexible mode can be suppressed by a so-called *directional notch filter*. Directional notch filters provide a way to design a single SISO notch filter that suppresses a targeted flexible mode throughout the MIMO structure. In this way, the order of the controller is reduced compared to conventional notch filter design, which requires a SISO notch filter in each of the decoupled loops, while at the same time only a single notch filter has to be tuned. The mode shape of the targeted mode is used to ensure that the directional notch filter acts in the direction of the flexible mode. This approach neither requires extra actuators nor sensors. Multiple flexible modes can be suppressed by placing multiple directional notch filters in series. Furthermore, it is shown that the mode shape of the flexible mode can be obtained from the measured FRD via a numerical optimization procedure.

Experiments on a flexible beam setup validate the practical applicability of the proposed method. For this setup three flexible modes that affect the stability of the closed-loop system can be suppressed successfully using directional notch filters. Compared to a conventional notch filter design, the order of the controller is reduced, the tuning process becomes more transparent, and MIMO stability is directly accounted for. Moreover, the effect of the flexible modes is better suppressed, especially in the off-diagonal entries.

## 5.2 Recommendations

From this thesis a number of recommendations for further research can be given. The recommendations are divided in three parts. First, recommendations will be given regarding the damping of the flexible modes. Second, suggestions for research on incorporating directionality in the control design are given. Finally, more general recommendations for research on control design for flexible motion systems are suggested.

### 5.2.1 Damping of flexible modes

It would be beneficial to improve the accuracy of the TFD computation, because the accuracy of the computed closed-loop poles depends directly on the accuracy of the computed TFD. The largest improvement in the accuracy of the computed TFD is expected in the improvement of the symmetry condition used to compute LHP from RHP TFD. The current method as applied in Chapter 3 uses the assumption that the system poles lie on a line parallel to the imaginary axis, while in reality the actual absolute damping increases for increasing frequency. By transforming the complex plane by means of a linear fractional transformation, the RHP TFD satisfies the symmetry condition better, see Appendix A. Additional research is required on this topic, for example to compute the error bounds for this method.

Also, the estimation of the uncertainty bounds can be improved. In particular, the estimation of the error bound due to the symmetry condition can be conservative. Furthermore, the error due to the integration method can be improved. The latter is estimated on the basis of computing a second derivative of the FRD, which is sensitive to noise. This can be improved by estimating the second derivative by fitting a smooth curve on the FRD in a certain frequency range around the point at which the derivative is computed. One option to be explored is to use the rational polynomial method, see e.g., Geerardyn et al. (2014).

The computation of TFD is performed in the  $s$ -plane, corresponding to a continuous-time description of the system. It would be interesting to investigate the possibility of computing discrete-time transfer function data DTFD in the  $z$ -plane. The symmetry condition to compute DTFD inside the unit disk from DTFD outside the unit disk can be performed using a linear fractional transformation, see Appendix A. This could open a door towards direct synthesis of discrete-time controllers using TFD.

In this thesis the pole locations are analysed using TFD. The control design is performed by using manual loop-shaping. Future research on numerical optimization methods that can compute controllers that satisfy both time- and frequency-domain performance specifications is recommended. The frequency-domain specifications can be satisfied via constraints on the FRD, while constraints on the closed-loop poles obtained from TFD account for the time-domain specifications.

It will also be interesting to study control design methods that directly exploit TFD. Design methods where the controller  $\mathbf{C}(s)$  is a function of  $\mathbf{H}(s)$  provide ideal candidates for this purpose, i.e.,  $\mathbf{C}(s) = \mathbf{f}(\mathbf{H}(s))$ . A first attempt towards this direction was made in Hoogendijk et al. (2010), where an optimal controller is computed from the TFD. However, only the FRD and not the TFD of the

controller can be obtained in that paper. Further research in this direction is highly recommended.

It is proposed to compute TFD from FRD, which in its turn is computed from time-domain data. It might be possible to omit the intermediate step of computing FRD. A Laplace transformation of the time-domain data will, in theory, give TFD directly. Future research is required to assess the potential of this method. Foreseen challenges for this approach are the design of suitable time domain signals for the identification, coping with the initial conditions and non-stationary nature of these signals, and the numerical properties of this approach.

### 5.2.2 Directionality of flexible modes

The design of directional notch filters suppresses flexible modes in a MIMO system in the proper direction to improve stability properties. However, this does not actively control these modes. It is desirable to investigate the possibility of designing filters that actively damp the flexible modes. This can for example be achieved by using skew notch filters instead of conventional notch filters. A challenge in this approach is that a skew notch affects a larger frequency interval. When multiple directional notch filters are used, this will generally cause interaction among these directional notch filters.

In the computation of the mode shapes from the FRD only the peaks of the resonances in the FRD are used in the optimization algorithm. Using more FRD points around the resonance frequency can make this procedure less sensitive to noise.

In this thesis directional notch filters are designed by manually tuning the parameters using the characteristic loci. More advanced control design techniques should be developed in designing directional notch filters. To omit the manual tuning step, the control design criteria should be formulated in terms of cost functionals, which can be minimized using numerical optimization techniques.

### 5.2.3 General recommendations

Although a data-based control approach is pursued in this thesis, the results can also be used for identification purposes. The TFD method can be used to compute open-loop pole locations, while the mode shapes can be obtained from the FRD with the optimization method that is described. A modal model could be constructed by combining these two results. A first exploration in this direction

is described in Venrooij and Peters (2013). However, this will require the analysis and improvement of the estimation of open-loop poles from TFD, which are currently computed not very accurately. Alternatively, recent results by Soumelidis et al. (2011, 2012) might be useful to compute the open-loop pole locations.

The results presented in this thesis provide new feedback control design methods for flexible motion systems. However, for performance feedforward control is very important, see the recent thesis by Ronde (2014) on this topic. Further research is required to investigate how these two techniques interact and how these can be combined to achieve fast and accurate positioning in high-precision motion systems.

In this thesis, the system design is assumed to be given. However, the design of these systems should be optimized to achieve the best performance. Knowledge of the opportunities and limitations of the state-of-the-art control designs should be taken into account while designing high-precision motion systems. The geometry, stiffness and weight of the mechanical structure, but also the number and locations of the actuators and sensors should be optimized in such a way that the control system can achieve the best possible performance.

## References

- Aangenent, W. H. T. M., Kostić, D., de Jager, A. G., van de Molengraft, M. J. G., and Steinbuch, M. (2005). Data-based optimal control. In *Proc. American Control Conf.*, pages 1460–1465, Portland, Oregon, USA. IEEE.
- Adams, R. A. (1999). *Calculus: A Complete Course*. Addison-Wesley.
- Anderson, B. D. O. and Moore, J. B. (1969). Linear system optimisation with prescribed degree of stability. *Proc. IEE*, 116(12):2083–2087.
- Anthonis, J. and Ramon, H. (1999). SVD  $\mathcal{H}_\infty$  controller design for an active horizontal spray boom suspension. In *Proc. 7th Mediterranean Conf. Control and Automation*, pages 90–102, Haifa, Israel.
- Anthonis, J. and Ramon, H. (2003). Design of an active suspension to suppress the horizontal vibrations of a spray boom. *J. Sound and Vibration*, 266(3):573–583.
- Ash, R. and Ash, G. (1968). Numerical computation of root loci using the Newton-Raphson technique. *IEEE Trans. Automatic Control*, (October):576–582.
- ASML (2014). ASML website <http://asml.nl/asml/show.do?ctx=28145&rid=44709>.
- Balas, M. J. (1978). Feedback control of flexible systems. *IEEE Trans. Automatic Control*, 23(4):673–679.
- Balas, M. J. (1979). Direct velocity feedback control of large space structures. *Journal of Guidance, Control, and Dynamics*, 2(3):252–253.
- Balas, M. J. (1982). Trends in large space structure control theory: Fondest hopes, wildest dreams. *IEEE Trans. Automatic Control*, 27(3):522–535.
- Bien, Z. and Xu, J. X. (1998). *Iterative learning control. Analysis, design, integration and applications*. Kluwer Academic Publishers.

- Bode, H. W. (1945). *Network analysis and feedback amplifier design*. Van Nostrand, Princeton NJ.
- Boerlage, M. L. G., Middleton, R. H., Steinbuch, M., and de Jager, A. G. (2010). Rejection of fixed direction disturbances in multivariable electromechanical motion systems. *Mechatronics*, 20(1):45–52.
- van den Brink, M. (2013). Continuing to shrink: Next-generation lithography—Progress and prospects. In *Proc. IEEE Int. Solid-State Circuits Conference Digest of Technical Papers (ISSCC)*, pages 20–25, San Francisco, CA, USA.
- Brockett, R. and Byrnes, C. (1981). Multivariable Nyquist criteria, root loci, and pole placement: a geometric viewpoint. *IEEE Trans. Automatic Control*, AC-26(1):271–285.
- Brown, D. L., Allemang, R. J., and Phillips, A. W. (2011). Autonomous modal parameter estimation: application examples. In *Proc. Society for Experimental Mechanics Series 6*, volume 3, pages 403–428, New York, NY, USA. Springer.
- Bruijnen, D. J. H. and van Dijk, N. (2012). Combined input shaping and feed-forward control for flexible motion systems. In *Proc. American Control Conf.*, pages 2473 – 2478, Montreal, Canada.
- Butler, H. (2011). Position control in lithographic equipment. *IEEE Control Systems Magazine*, 31(5):28–47.
- Cabral, F. B. and Safonov, M. G. (1996). A falsification perspective on model reference adaptive control. In *Proc. of 35th IEEE Conf. on Decision and Control*, volume 3, pages 2982–2985, Kobe, Japan. IEEE.
- Cabral, F. B. and Safonov, M. G. (2004). Unfalsified model reference adaptive control using the ellipsoid algorithm. *Int. J. Adaptive Control and Signal Processing*, 18(8):683–696.
- de Callafon, R. A. and van den Hof, P. M. J. (2001). Multivariable feedback relevant system identification of a wafer stepper system. *IEEE Transactions on Control Systems Technology*, 9(2):381–390.
- Campi, M. C., Lecchini, A., and Savaresi, S. M. (2000). Virtual Reference Feedback Tuning (VRFT): a new direct approach to the design of feedback controllers. In *Proc. 2000 IEEE Conf. Decision and Control*, volume 1, pages 623–629, Sidney, Australia. IEEE.
- Cazzulani, G., Resta, F., and Ripamonti, F. (2011). An application of the IMSC on a non-linear flexible structure: numerical analysis and experimental validation. In *Proc. World Congress on Engineering*, volume III, pages 2221–2226, London, UK.

- 
- Chan, J.-T. H. (1996). Data-based synthesis of a multivariable linear-quadratic regulator. *Automatica*, 32(3):403–407.
- Chughtai, S. S., Nobakhti, A., and Wang, H. (2005). A systematic approach to the design of robust diagonal dominance based MIMO controllers. In *Proc. IEEE Conf. Decision and Control*, pages 6875–6880, Seville, Spain.
- Durango-Galvan, S. E., Heertjes, M. F., and Dunand, R. (2012). Plant enhancements in motion systems by modal control. In *Proc. American Control Conf.*, pages 5348–5353, Montreal, QC.
- Evans, W. R. (1950). Control system synthesis by root locus method. *Trans. AIEE*, 69(1):66–69.
- Ewins, D. J. (1986). *Modal testing: theory and practice*. Research Studies Press for Bruel & Kjaer.
- Formentin, S., Savaresi, S. M., and Del Re, L. (2012). Non-iterative direct data-driven controller tuning for multivariable systems: theory and application. *IET Control Theory and Applications*, 6(9):1250.
- Franklin, G. F., Powell, J. D., and Emami-Naeini, A. (2002). *Feedback control of dynamic systems*. Addison-Wesley series in electrical and computer engineering. Prentice Hall.
- Friswell, M. I. (2001). On the design of modal actuators and sensors. *J. Sound and Vibration*, 241(3):361–372.
- Gaing, Z.-L. (2004). A particle swarm optimization approach for optimum design of PID controller in AVR system. *IEEE Trans. on Energy Conversion*, 19(2):384–391.
- Gawronski, W. K. (2004). *Advanced structural dynamics and active control of structures*. Springer Verlag.
- Geerardyn, E., Oomen, T. A. E., and Schoukens, J. (2014). Enhanced  $\mathcal{H}_\infty$  norm estimation using local LPM/RPM modeling: Applied to an AVIS. In *Proc. IFAC 19th Triennial World Congress*, pages 1–6, Capetown, South Africa.
- Goh, C. J. and Caughey, T. K. (1985). On the stability problem caused by finite actuator dynamics in the collocated control of large space structures. *Int. J. of Control*, 41(3):787–802.
- Grassi, E., Tsakalis, K. S., Dash, S., Gaikwad, S. V., MacArthur, W., and Stein, G. (2001). Integrated system identification and PID controller tuning by frequency loop-shaping. *IEEE Trans. Control Systems Technology*, 9(2):285–294.



- Guardabassi, G. O. and Savaresi, S. M. (2000). Virtual reference direct design method: an off-line approach to data-based control system design. *IEEE Trans. Automatic Control*, 45(5):954–959.
- Haddad, W. M. and Bernstein, D. S. (1992). Controller design with regional pole constraints. *IEEE Trans. Automatic Control*, 37(1):54–69.
- Halikias, G. D., Zolotas, A. C., and Nandakumar, R. (2007). Design of optimal robust fixed-structure controllers using the quantitative feedback theory approach. *Proc. of the Institution of Mechanical Engineers, Part I: J. Systems and Control Engineering*, 221(4):697–716.
- den Hamer, A. J. (2010). *Data-driven optimal controller synthesis: a frequency domain approach*. PhD thesis, Eindhoven University of Technology.
- den Hamer, A. J., Angelis, G. Z., van de Molengraft, M. J. G., and Steinbuch, M. (2005). A practical loop-shaping approach for pole-placement in mechatronic systems. In *Proc. IEEE Conf. Control Applications*, pages 394–399, Toronto, Canada. IEEE.
- den Hamer, A. J., Weiland, S., Steinbuch, M., and Angelis, G. Z. (2008). Stability and causality constraints on frequency response coefficients applied for non-parametric  $\mathcal{H}_2$  and  $\mathcal{H}_\infty$  control synthesis. In *Proc. IEEE Conf. Decision and Control*, pages 3670–3675, Cancun, Mexico.
- Hara, S., Yamamoto, Y., Omata, T., and Nakano, M. (1988). Repetitive control system a new-type servo system. *IEEE Trans. Automatic Control*, AC-33:659–688.
- Heath, M. T. (2005). *Scientific computing: an introductory survey*. McGraw-Hill.
- van Helvoort, J. J. M., de Jager, A. G., and Steinbuch, M. (2008). Data-driven controller unfalsification with analytic update applied to a motion system. *IEEE Trans. Control Systems Technology*, 16(6):1207–1217.
- van Herpen, R. M. A. (2014). *Identification for control of complex motion systems*. PhD thesis, Eindhoven University of Technology.
- Hjalmarsson, H. and Birkeland, T. (1998). Iterative feedback tuning of linear time-invariant MIMO systems. In *Proc. 37th IEEE Conf. Decision and Control*, number December, pages 3893–3898, Tampa, Florida, USA.
- Hjalmarsson, H. and Gevers, M. (1998). Iterative feedback tuning: theory and applications. *IEEE Control Systems Magazine*, (August):26–41.

- Hoogendijk, R., den Hamer, A. J., Angelis, G., van de Molengraft, M. J. G., and Steinbuch, M. (2010). Frequency response data based optimal control using the data based symmetric root locus. In *Proc. IEEE Int. Conf. Control Applications*, number 2, pages 257–262, Yokohama, Japan. Ieee.
- Hooijkamp, E. C., van Keulen, F., and van Eijk, J. (2012a). Modal analysis applied to transient thermal problems. In *Proc. 8th European Solid Mechanics Conf.*, pages 1–2, Graz, Austria.
- Hooijkamp, E. C., Peters, H. J., van Keulen, F., and van Eijk, J. (2012b). Engineering interpretation of eigenvector sensitivities using normalization. In *Proc. ASPE summer topical meeting on Precision Engineering and Mechatronics Supporting the Semiconductor Industry*, pages 80–82, Berkeley, California.
- Hooijkamp, E. C., Saathof, R., van Keulen, F., and van Eijk, J. (2012c). Measured thermal modes for thermal design optimization. In *Proc. 12th Euspen Int. Conf.*, pages 416–419, Stockholm, Sweden.
- Horowitz, I. M. (1963). *Synthesis of feedback systems*. Academic Press.
- Horowitz, I. M. (1993). *Quantitative feedback design theory*. QFT Publications, Boulder, Colorado.
- Hovd, M. and Skogestad, S. (1994). Sequential design of decentralized controllers. *Automatica*, 30(10):1601–1607.
- Hughes, P. (1987). Space structure vibration modes: How many exist? Which ones are important? *IEEE Control Systems Magazine*, 7(1):22–28.
- Inman, D. J. (1984). Modal decoupling conditions for distributed control of flexible structures. *J. Guidance, Control, and Dynamics*, 7(6):750–752.
- Inman, D. J. (2001). Active modal control for smart structures. *Philosophical Trans. Royal Society of London, Series A*, 359(1778):208–219.
- Jung, J.-H., Cheng, T.-H., and Oh, I.-K. (2012). Electromagnetic synchronized switch damping for vibration control of flexible beams. *IEEE/ASME Trans. Mechatronics*, 17(6):1031–1038.
- Karimi, A. and Galdos, G. (2010). Fixed-order controller design for nonparametric models by convex optimization. *Automatica*, 46(8):1388–1394.
- Karimi, A., Kunze, M., and Longchamp, R. (2007). Robust controller design by linear programming with application to a double-axis positioning system. *Control Engineering Practice*, 15(2):197–208.

- Karimi, a., Mišković, L., and Bonvin, D. (2003). Iterative correlation-based controller tuning with application to a magnetic suspension system. *Control Engineering Practice*, 11(9):1069–1078.
- Katalenić, A. (2013). *Control of reluctance actuators for high-precision positioning*. PhD thesis, Eindhoven University of Technology.
- Keel, L. H. and Bhattacharyya, S. P. (2008). Controller synthesis free of analytical models: three term controllers. *IEEE Trans. Automatic Control*, 53(6):1353–1369.
- Lequin, O., Gevers, M., Mossberg, M., Bosmans, E., and Triest, L. (2003). Iterative feedback tuning of PID parameters: comparison with classical tuning rules. *Control Engineering Practice*, 11(9):1023–1033.
- Levin, J. (2011). Adaptive notch filter using real-time parameter estimation. *IEEE Trans. Control Systems Technology*, 19(3):673–681.
- Levine, W. S. (2011). *The control handbook - control system applications*. CNC Press, Boca Raton FL.
- MacFarlane, A. G. J. and Postlethwaite, I. (1977). Characteristic frequency functions and characteristic gain functions. *Int. J. Control*, 26(2):265–278.
- Maciejowski, J. M. (1989). *Multivariable feedback design*. Addison-Wesley.
- Mack, C. (2008). *Fundamental principles of optical lithography: the science of microfabrication*. Wiley.
- Makarovic, J., Schneiders, M. G. E., van der Wielen, A. M., Lomonova, E. A., van de Molengraft, M. J. G., Compter, J. C., Steinbuch, M., and Schellekens, P. H. J. (2004). Integrated design of a lightweight positioning system. In *Proc. 7th Int. Conf. Motion and Vibration Control*, pages 1–10, St. Louis, USA.
- Mayne, D. Q. (1973). The design of linear multivariable systems. *Automatica*, 9(2):201–207.
- Meirovitch, L. (1997). *Principles and techniques of vibrations*. Prentice Hall.
- Meirovitch, L. and Baruh, H. (1983). On the problem of observation spillover in self-adjoint distributed-parameter systems. *J. Optimization Theory and Applications*, 39(2):269–291.
- Mitsukura, Y., Yamamoto, T., and Kaneda, M. (1999). A design of self-tuning PID controllers using a genetic algorithm. In *Proc. American Control Conf.*, volume 2, pages 1361–1365, San Diego, CA, USA. IEEE.

- 
- Molins, C. and Garcia-Sanz, M. (2009). Automatic loop-shaping of QFT robust controllers. In *Proc. IEEE National Aerospace & Electronics Conf.*, pages 103–110, Dayton, OH, USA.
- Oomen, T. A. E. and Bosgra, O. H. (2012). System identification for achieving robust performance. *Automatica*, 48(9):1975–1987.
- Oomen, T. A. E., van Herpen, R. M. A., Quist, S., van de Wal, M. M. J., Bosgra, O. H., and Steinbuch, M. (2014). Connecting system identification and robust control for next-generation motion control of a wafer stage. *IEEE Trans. Control Systems Technology*, 22(1):102–118.
- Owens, D. H. (1978). On structural invariants and the root-loci of linear multi-variable systems. *Int. J. of Control*, 28(2):187–196.
- Pettinato, J. S. and Pillai, D. (2005). Technology decisions to minimize 450-mm wafer size transition risk. *IEEE Trans. Semiconductor Manufacturing*, 18(4):501–509.
- Pintelon, R. and Schoukens, J. (2001). *System identification: a frequency domain approach*. IEEE Press, Piscataway, NJ.
- Postlethwaite, I. and MacFarlane, A. G. J. (1979). *Lecture notes in control and information science vol. 12: a complex variable approach to the analysis of linear multivariable feedback systems*. Springer Verlag.
- Preumont, A. (2011). *Vibration control of active structures: an introduction*. Springer Verlag Berlin Heidelberg, third edition.
- Preumont, A., Dufour, J.-P., and Malekian, C. (1992). Active damping by a local force feedback with piezoelectric actuators. *J. Guidance, Control, and Dynamics*, 15(2):390–395.
- Preumont, A. and Seto, K. (2008). *Active control of structures*. Wiley Online Library.
- Rahman, M. (1997). *Complex variables and transform calculus*. Computational Mechanics Publications.
- Resta, F., Ripamonti, F., Cazzulani, G., and Ferrari, M. (2010). Independent modal control for nonlinear flexible structures: An experimental test rig. *J. Sound and Vibration*, 329(8):961–972.
- Reynders, E. (2012). System identification methods for (operational) modal analysis: review and comparison. *Archives of Computational Methods in Engineering*, 19(1):51–124.

- Ronde, M. J. C. (2014). *Feedforward control for lightweight motion systems*. PhD thesis, Eindhoven University of Technology.
- Schneiders, M. G. E., van de Molengraft, M. J. G., and Steinbuch, M. (2004). Benefits of over-actuation in motion systems. In *Proc. American Control Conf.*, pages 505–510, Boston, Massachusetts, USA.
- Silvas, E., Hoogendijk, R., Aangenent, W. H. T. M., van de Wal, M. M. J., and Steinbuch, M. (2012). Modal decoupling of a lightweight motion stage using algebraic constraints on the decoupling matrices. In *Proc. 31st Benelux meeting on System and Control*, page 166, Heijen, the Netherlands.
- Skelton, R. E. and Shi, G. (1994). The data-based LQG control problem. In *Proc. IEEE Conf. Decision and Control*, number 0, pages 1–6, Lake Buena Vista, FL, USA.
- Skogestad, S. and Morari, M. (1987). Effect of disturbance directions on closed-loop performance. *Ind. Eng. Chem. Res.*, 26(10):2029–2035.
- Skogestad, S. and Postlethwaite, I. (2005). *Multivariable feedback control: analysis and design*. John Wiley & Sons.
- Soumelidis, A., Bokor, J., and Schipp, F. (2012). Identifying poles from time-domain data using discrete Laguerre system. In *Proc. 20th Mediterranean Conference on Control & Automation (MED)*, volume 1, pages 1450–1455, Barcelona, Spain. Ieee.
- Soumelidis, A., Schipp, F., and Bokor, J. (2011). Pole structure estimation from laguerre representations using hyperbolic metrics on the unit disc. In *IEEE Conf. Decision and Control and European Control Conf.*, pages 2136–2141, Orlando, FL, USA. Ieee.
- Spall, J. C. and Cristion, J. A. (1998). Model-free control of nonlinear stochastic systems with discrete-time measurements. *IEEE Trans. Automatic Control*, 43(9):1198–1210.
- Steinbuch, M. and Norg, M. L. (1998). Advanced motion control: An industrial perspective. *European J. Control*, 4:278–293.
- Taboga, M. (2013). *Lectures on probability theory and mathematical statistics*. CreateSpace Independent Publishing Platform.
- Tesche, F. M. (1992). On the use of the Hilbert transform for processing measured CW data. *IEEE Trans. Electromagnetic Compatibility*, 34(3):259–266.
- Tsiotras, P. (2005). The relation between the 3-D Bode diagram and the root locus. *IEEE Control Systems Magazine*, 25(1):88–96.

- 
- Vaes, D. (2005). *Optimal static decoupling for multivariable control design*. PhD thesis, Katholieke Universiteit Leuven.
- Venrooij, S. J. P. and Peters, T. M. C. (2013). MIMO fitting tool for motion systems with flexible structures. Technical report, Eindhoven University of Technology.
- Vrijssen, N. H., Jansen, J. W., Compier, J. C., and Lomonova, E. A. (2013a). Measurement method to determine the magnetic hysteresis effects of reluctance actuators by evaluation of the force and flux variation. *Rev. Sci. Instrum.*, 84(7).
- Vrijssen, N. H., Jansen, J. W., and Lomonova, E. A. (2013b). Force prediction including hysteresis effects in a short-stroke reluctance actuator using a 3d-FEM and the Preisach model. *Applied Mechanics and Materials*, 416-417:187–194.
- Vrijssen, N. H., Jansen, J. W., and Lomonova, E. A. (2014). Prediction of magnetic hysteresis in the force of a pre-biased E-core reluctance actuator. *IEEE Trans. Industry Applications*, (99):1–9.
- Wagner, C., Bacelar, J., Harned, N., Loopstra, E., Hendriks, S., de Jong, I., Kuerz, P., Levasier, L., van de Kerkhof, M., Lowisch, M., Meiling, H., Ockwell, D., Peeters, R., van Setten, E., Stoeldraijer, J., Young, S., Zimmerman, J., and Kool, R. (2011). EUV lithography at chipmakers has started: performance validation of ASML's NXE:3100. In *Proc. SPIE 7969 Extreme Ultraviolet (EUV) Lithography II*, page 79691F, San Jose, California.
- van de Wal, M. M. J., van Baars, G., Sperling, F., and Bosgra, O. H. (2001). Experimentally validated multivariable  $\mu$  feedback controller design for a high-precision wafer stage. In *Proc. IEEE Conf. Decision and Control*, pages 1583–1588, Orlando, FL, USA.
- van de Wal, M. M. J., van Baars, G., Sperling, F., and Bosgra, O. H. (2002). Multivariable  $\mathcal{H}_\infty/\mu$  feedback control design for high-precision wafer stage motion. *Control Engineering Practice*, 10(7):739–755.



## Appendix A

# Symmetry condition using a LFT

The symmetry condition 3.21 is used to compute LHP TFD from THP TFD. In this method the LHP TFD is computed by mirroring in a point on the negative real axis. Figure A.1 shows the TFD gridpoints  $s_i$  that result from this transformation. This symmetry condition would be valid if all poles and zeros would have the same absolute damping. Instead, in reality mechanical systems have a damping ratio  $\zeta$ . The poles will lie on a line at an angle  $\theta = \arcsin(\zeta)$  with respect to the imaginary axis, see the poles and zeros in Figure A.1.

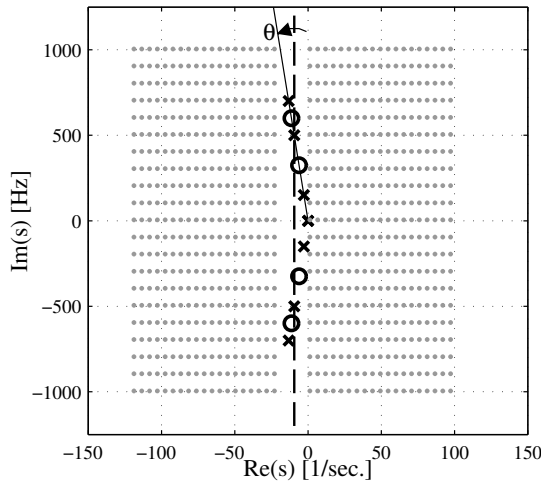


Figure A.1: Conventional symmetry condition. Symmetry in a point on the real axis is used to compute LHP TFD from RHP TFD.



A better symmetry condition can be obtained by using a linear fractional transformation (LFT) defined by

$$\bar{s} = \frac{as + b}{cs + d}, \quad (\text{A.1})$$

to transform the  $s$ -plane to the transformed  $\bar{s}$ -plane. The advantage of this transformation is that it is a one-on-one transformation that preserves symmetry. A linear fractional transformation maps circles and lines on circles and lines and can be regarded as a composition of translations, rotations, magnifications, and inversions. The inverse transformation is easily derived and is given by

$$s = \frac{-d\bar{s} + b}{c\bar{s} - a}. \quad (\text{A.2})$$

This transformation can be used to transform the  $s$ -plane, such that the poles and zeros are approximately mapped on the imaginary axis. Consequently, the symmetry condition (2.9) can be used to compute the LHP TFD. Finally, the inverse transformation is applied. The resulting TFD gridpoints  $s_i$  for this transformation are shown in Figure A.2.

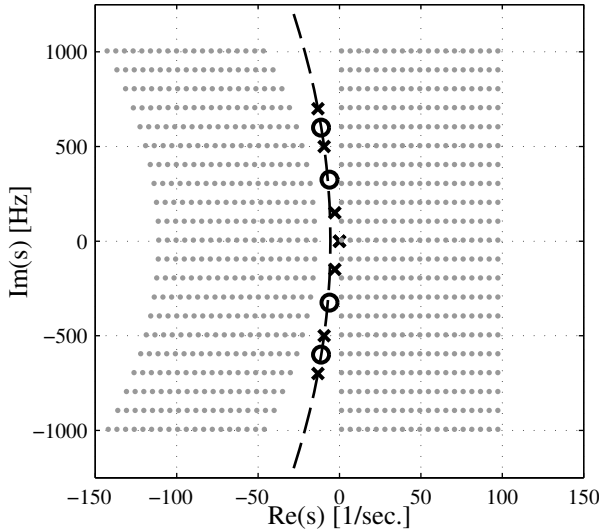


Figure A.2: Symmetry condition that uses the linear fractional transformation. Symmetry in a circle is used to compute LHP TFD from RHP TFD.

The procedure consists of four steps, which are depicted in Figure A.3.

**1. Find the LFT that maps the pole locations to the imaginary axis**

Finding the LFT implies finding the four constants  $a$ ,  $b$ ,  $c$  and  $d$ . Firstly,  $a = 1$  is chosen as this parameter acts as a scaling parameter. This way three parameters remain, which can be found by imposing three constraints on the parameters. Selecting three pairs of  $s$  and  $\bar{s}$  values enables an algebraic solution for this problem. These are chosen to be

$$\begin{aligned} s_1 &= \sigma_p + j\omega_p & \bar{s}_1 &= j\omega_p \\ s_2 &= \sigma_p - j\omega_p & \bar{s}_2 &= -j\omega_p \\ s_3 &= -d & \bar{s}_3 &= 0, \end{aligned} \tag{A.3}$$

where  $\sigma_p$  and  $\omega_p$  are the (estimated) absolute damping and frequency of a pole  $p = \sigma_p \pm j\omega_p$  of interest. In the example in the figure, the pole at 500 Hz is chosen to be the pole of interest. The circle of the LFT will go through these pole-locations, ensuring that the transformation is accurate around the pole of interest. The parameter  $d$  is chosen such that the tangent of the circle is parallel to the line on which the poles lie, which makes an angle  $\theta = \arcsin(\zeta)$  with respect to the imaginary axis, see the top plot of Figure A.3.

**2. Transform the RHP grid points  $s_i$  using the LFT**

Next, the transformation of the RHP TFD points is executed, see the second plot of Figure A.3. In this figure the pole locations are transformed as well, to demonstrate that these lie approximately on the imaginary axis. In practice this last step is of course not conducted.

**3. Compute the LHP TFD**

The symmetry condition (2.9) is used to compute the LHP TFD from the transformed RHP TFD, see the third plot in Figure A.3. The symmetry condition will be accurate as the poles approximately lie on the imaginary axis.

**4. Transform the TFD using the inverse LFT**

The inverse transformation (A.2) is applied to recover the TFD points in the original  $s$ -plane, see the bottom plot of Figure A.3. This gives the result that was shown in Figure A.2.

Although this gives a more accurate symmetry condition, additional research is required to use this in practice. Firstly, uncertainty bounds for this computation need to be derived. Furthermore, in the LHP the TFD grid becomes non-square, which requires some adjustments in the algorithms to compute the pole locations.

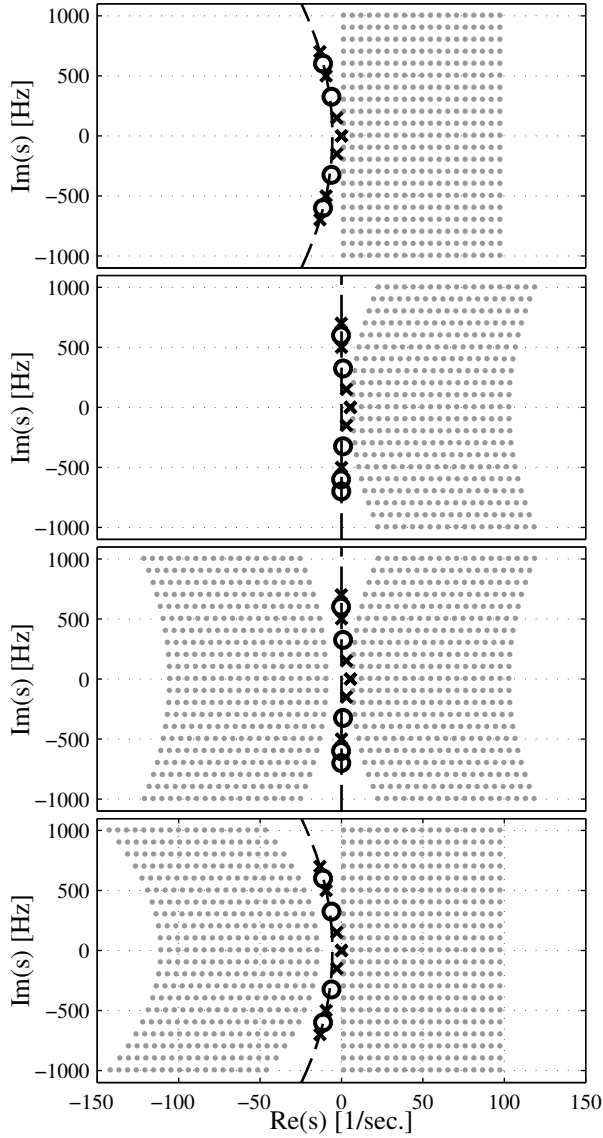


Figure A.3: Process to obtain TFD in the LHP using the LFT.

## Acknowledgements

While I write these final words of my thesis I realise that in a few weeks, I will defend my thesis exactly five years after I started as a Ph.D. candidate. Completing a thesis is something that cannot be done all alone. Therefore, I want to thank all the people that were involved in this process.

First of all, I want to thank my promotor Maarten Steinbuch for providing me the opportunity to do a Ph.D.. Thank you for the inspiring and motivating discussions and for your support in many ways during the project. Next, I want to thank my co-promotors René van de Molengraft and Marcel Heertjes for their supervision. René, your critical view during the meetings improved the contents of this thesis a lot. Marcel, your enthusiasm during the last months of the project helped me to put the ideas on paper, resulting in this thesis.

I also want to thank the students that helped to explore, investigate and develop the concepts that are treated in this thesis. Ronald, Emilia, Andrei, Emilia, Jan, Tim, Daniel, Yasemin, John, Scott and Ton, it was a pleasure to work with you. You have all contributed to this thesis in your own way.

I enjoyed working with the industrial partners of this project: ASML, Bosch-Rexroth, Heidenhein, Magnetic Innovations, MI-Partners, Philips Innovation Services, Prodrive and Vision Dynamics Mechaphysics. During the project meetings I was inspired by the problems that the industrial partners brought to table. A special thanks to ASML and in particular to Wouter Aangenent and Marc van de Wal for their input and to George Leenknecht for his help in successfully conducting the experiments that are presented in Chapter 3. I also appreciate the collaboration with Philips in supervising a number of students. I thank Dennis Bruijnen, Niels van Dijk and Arjen den Hamer for the pleasant cooperation.

I want to express my appreciation to all committee members: Georgo Angelis, Hans Butler, Jan Swevers and Siep Weiland for reading my thesis and providing valuable input.

The work environment that I have experienced in the basement of the Gemini building was exactly the opposite of the quality of the view that you get from the windows on this floor. I thank my roommates Jeroen, Cesar and Joost for the nice atmosphere in -1.126. I appreciate the conversations that we have had about our theses and about many other topics and the variety of music from our office theatre pc ranging from 100%NL to SmoothJazz and from the Colombian radio of DJ C-Lo to Vivaldi's four seasons. Despite the fact that he left us without prior notice during the last Christmas holiday, I want to thank our office cat Azrael who provided vital distractions in my last year. I also want to thank our neighbors: Robbert, Michael and Irmak for their company, the lunch walks and for their delicious coffee that always announced itself by a splash of water from the window, followed by the sound of the coffee bean grinder.

I also thank the other colleagues from CST and D&C for the nice lunches, conferences and cooperation. Furthermore, I want to thank the lab-employees Harrie, Peter, Pieter, Sjeff, Rob and Hennie for the best coffee of the TU/e (although our neighbours dare to challenge that). Waking up with good coffee and a nice chat was a good start of every day.

Robocup has been a very nice distraction from my Ph.D. work. Working together in a great team to learn robots to play robot soccer has been a welcome change from the daily work. I want to thank all Tech United members for the nice Tuesday evenings, the tournaments and the fun trips that we we made all over the world.

Last but not least I want to thank my lovely wife Marenne for always being there for me. Thank you for your support, for providing distraction whenever I needed it and for putting things into perspective.

## Curriculum Vitae



Rob Hoogendijk was born on Januari 30, 1983 in Lage Zwaluwe, the Netherlands. After finishing his secondary education at the Sint-Oelbert Gymnasium in Oosterhout in 2001, he studied applied physics at the Eindhoven University of Technology. In 2004 he changed to mechanical engineering as this department matched his interests better. The design of a ball-handling system for Tech United, the robot soccer team of the university, was the topic of his Bachelor final project. Thereafter, he started his master in the Control Systems Technology group. In 2008 he performed an internship at ASML in Veldhoven during which he developed an improved decoupling of the wafer stage long stroke. In 2009 he received his Master's degree with great appreciation on the topic 'Applications of Transfer Function Data'. This graduation research was performed at Philips Applied Technologies in Eindhoven. From 2009, he started as a Ph.D. candidate in the Control Systems Technology group at the department of mechanical engineering of the Eindhoven University of Technology on the topic 'Control of Flexible Motion Systems using Frequency Response Data', which resulted in this thesis. During his Ph.D., he completed the educational program of the graduate school DISC and was team-leader/member of Tech United in the RoboCup competition. He currently holds a position at the research and development department of Océ in Venlo where he works on industrial printing systems.

